

# **BULGARIAN CHEMICAL COMMUNICATIONS**

**2022** Volume 54 / Number 2

*Journal of the Chemical Institutes  
of the Bulgarian Academy of Sciences  
and of the Union of Chemists in Bulgaria*



## Modeling of polyester fabric dyeing after proteolytic enzyme pre-treatment

D. M. Djordjevic<sup>1\*</sup>, R. P. Krstic<sup>1</sup>, M. G. Kodric<sup>1</sup>, S. P. Djordjevic<sup>2</sup>

<sup>1</sup>University of Nis, Faculty of Technology in Leskovac, Serbia

<sup>2</sup>Higher Technological and Artistic Professional School Leskovac, Serbia

Received: April 12, 2021; Revised: March 02, 2022

This paper investigates modeling of dyed fabrics made of 100% polyester fibers with disperse dye, after pre-treatment with the proteolytic enzyme papain. The aim of the enzyme pre-treatment is to modify the surface of fibers in order to influence the sorption properties and the possibility of dyeing polyester fabric without carriers in atmospheric conditions. Based on the examination results of the polyester fabric, it was determined that the water absorption, and the wetting rates improve to a great extent after treatment with papain enzyme. Langmuir isotherm, among the equilibrium models, proved to be the best for the description of the process of enzyme-modified polyester dyeing with disperse dye, adsorption occurred at a limited number of definitely localized spots on the fiber, and the adsorbed layer was monomolecular.

**Keywords:** polyester, papain enzyme, dyeing, disperse dye, modeling, isotherms.

### INTRODUCTION

Polyester (PES) fibers (usually polyethylene terephthalate) belong to a group of synthetic fibers with active spots where dye molecules can be located (attached, integrated). PES fibers have an expressed hydrophobic character and compact structure, which makes the dyeing process more difficult, leading it towards extreme conditions. The alternative is to modify these fibers or to modify the usual dyeing process, that is to increase the rate of dye diffusion into fibers [1, 2].

For simpler dyeing of PES fibers, various pre-preparation methods are used. Thus, hydrolytic modification of the surface of polyester materials (treatment with different alkalis) is mentioned in order to obtain a better appearance, touch and simpler dyeing.

Furthermore, enzymes are increasingly being used in this field, as ecological and nature-friendly products [3]. Enzymes used to improve the hydrophilicity of polyester fiber include lipases, polyesterases, cutinases and papain [4, 5]. Among them, papain has a wide specificity by showing the activity of amidases and esterases [4, 5].

Papain, also known as papaya proteinase I, is the cysteine protease enzyme (EC 3.4.22.2) found in the papaya species, *Carica papaya* and *Vasconcellea cundinamaricensis*. It was discovered that the enzyme is localized in the papaya bark and that it is collected from cut unripe papaya fruit as raw latex. Papain is primarily used as amidase in textile processing, and not as esterase. There are few papers analyzing the possibility of papain modifying

polyester fabric in order to improve its hydrophilicity by hydrolysis of ester bonds [6, 7].

The purpose of the paper is to clarify the adsorption ability of a disperse dye for PES fibers pre-modified with the usual additives according to the standard dyeing recipe, without the use of carriers. The aim is to simplify the dyeing of polyester fibers with the help of nature-friendly enzymes, to eliminate additives (carrier) and to dye at lower temperatures and atmospheric conditions. The modeling of polyester dyeing with selected isothermal models will explain the expediency of pre-preparation of polyester by enzyme papain.

### EXPERIMENTAL

For pre-treatment and later dyeing, polyester fabric (100% polyethylene terephthalate) kindly offered by the textile company Yumco (Vranje, Serbia) was used, with the following characteristics: warp and weft fineness per 17×2 tex, warp and weft density of 35 and 29 threads/cm and surface mass of 235 g/m<sup>2</sup>.

Before dyeing sample preparation was performed, i.e. pre-treatment of polyester with the commercial enzyme. The used enzyme commercial papain (Sigma-Aldrich, USA) had the following characteristics: enzyme origin—papaya latex, *Carica Papaya*, crude powder, 1.5-10 units/mg, mol. wt. 21 kDa.

Besides the enzyme, the polyester treatment bath consisted of a buffered solution and an activator (ethylenediamine-tetra acetic acid). Tris buffer solution (pH 8), a mixture of tris(hydroxy- methyl) aminomethane (Centrohem, Serbia) and hydro-

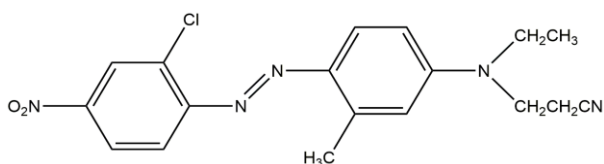
\* To whom all correspondence should be sent:  
E-mail: drag\_64@yahoo.com

chloric acid (Centrohem, Serbia) were used in the following ratio: 100 cm<sup>3</sup> of 0.1 M tris (hydroxymethyl) aminomethane + 58.4 cm<sup>3</sup> of 0.1 M hydrochloric acid, while ethylenediamine-tetra acetic acid (Centrohem, Serbia) was used at a concentration of 5% (owf). It is a relatively inexpensive strategy for immobilizing enzymes on polyester fabric by supporting functionalization with ethylenediamine.

Samples of polyester fabric were treated in a bath with active ingredients, that is the ratio of liquid and textile was 40:1, the bath temperature was 40°C, and the processing time was 120 min. The concentration of the enzyme papain for polyester processing was 65% (owb).

All polyester treatments with papain enzyme were carried out in a Linitest laboratory device. After processing, enzyme inactivation was performed, PES fabric samples were immersed in hot water (90°C) and held for 15 minutes.

The following test methods were used for checking the effects of enzymatic hydrolysis: change in mass (based on the differences in mass before and after processing); water absorption power-capillarity (ISO 18695:2007: a test specimen (polyester fabric) is immersed vertically, partly in water and after a certain time (1 min) measure the height of the part of the tube above the surface of the water which is wetted by water penetration); water absorption power-absorption (ISO 18696:2006: the mass of the test specimen is measured before immersion in water, then the tube is immersed in water and after 1 min the mass of the wet tube is measured. The amount of water remaining on the test tube after squeezing is calculated as a percentage); scanning electron microscopy (SEM) on a Jeol JCM 5300 type apparatus; wetting time (AATCC TM27-2013: a test specimen is padded in a water solution of a rewetting agent and dried. A drop of water is then carefully deposited on the taut surface of the specimen and the time required for a specular reflection of the water is recorded as the rewetting time), mechanical characteristics (ISO 5081).



**Figure 1.** The structure of the disperse dye C.I. Disperse Red 5 (using the ChemBioDraw Ultra 14.0 software).

The applied dye belongs to the class of mono azo dyes, and it has a small molecule suitable for a polyester. The dyeing process (the exhaustion method) was realized in a 98°C bath, without added carriers, the bath pH was 5. First, a dispersant is added to the bath, then the dye and finally the PES textile sample. Dyeing-adsorption begins and ends at 98°C at the predicted time.

The dyeing-adsorption test itself was performed in such a way that the mass of PES fabric was constant (1 g), the dyeing bath had a constant volume (100 cm<sup>3</sup>), the concentration of disperse dye ranged from 10 to 100 mg/dm<sup>3</sup>, while the processing time, with continuous stirring on a bath shaker (135 rpm), ranged from 5 to 60 minutes.

UV-VIS spectrophotometry and Cary 100 Conc UV-VIS apparatus, Varian (maximum absorption at 490 nm) were used to determine the dye concentration in the solution.

The amount of adsorbed disperse dye per unit mass of modified polyester fabric [8] (adsorption capacity at time  $t$  or at equilibrium time) was calculated using the following formula:

$$q_{t,e} = \frac{(C_o - C_{t,e}) \cdot V}{w} \quad (1)$$

where:  $C_o$  (g/dm<sup>3</sup>) is the initial dye concentration;  $C_{t,e}$  (g/dm<sup>3</sup>) is the dye concentration at time  $t$  or at equilibrium time;  $w$  (kg) fabric mass and  $V$  (dm<sup>3</sup>) is the solution volume from which adsorption was performed.

Langmuir adsorption model [9] is represented by the following equation:

$$\frac{1}{q_e} = \frac{1}{Q_o} + \left[ \frac{1}{b \cdot Q_o} \right] \cdot \frac{1}{C_e} \quad (2)$$

where:  $Q_o$  (mg/g) is the adsorption capacity,  $b$  (dm<sup>3</sup>/mg) is the adsorption energy.

The isothermal equation *Harkins-Jura* [9] is expressed as:

$$\frac{1}{q_e^2} = \frac{B_{HJ}}{A_{HJ}} - \frac{1}{A_{HJ}} \cdot \log(C_e) \quad (3)$$

where  $B_{HJ}$  and  $A_{HJ}$  are *Harkins-Jura* model constants.

The *Temkin* isotherm [9] is represented by the following equation:

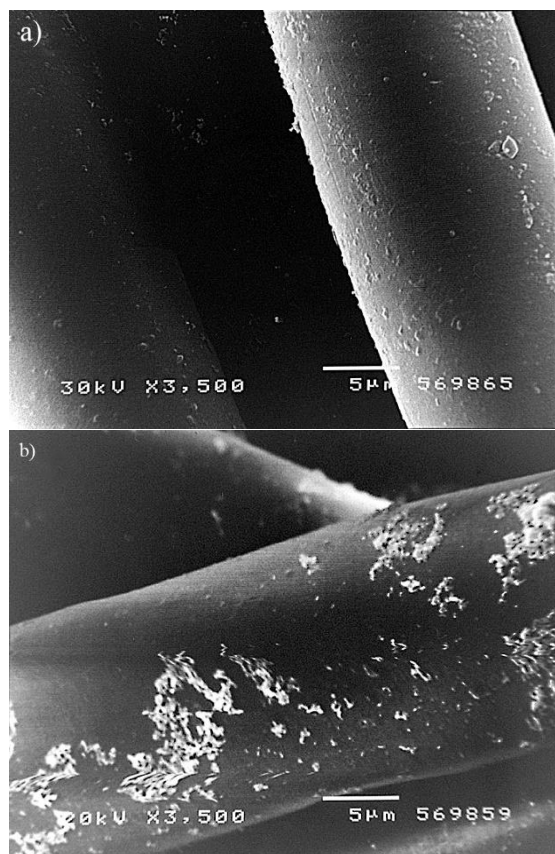
$$q_e = B_T \cdot \ln(K_T) + B_T \cdot \ln(C_e) \quad (4)$$

where:  $K_T$  (dm<sup>3</sup>/mg) and  $B_T$  are *Temkin* constants, the first of which is the adsorbate-adsorbent interaction, and the other one is related to the heat of adsorption  $b_T$  (J/mol).

## RESULTS AND DISCUSSION

In the enzyme processing mode in a wet environment, the substrate, i.e. polyester fabric, undergoes appropriate changes, primarily on its surface. Considering the high degree of crystallinity, compactness and strength of these fibers, it is very unlikely that these treatments would affect the internal structure of the fibers.

The confirmation of events on the polyester surface after enzyme treatment can be seen through a micrograph of fibers from the PES fabric recorded with a magnification of several thousand times. Figure 2 shows surface micrographs of untreated and papain enzyme-treated PES fibers. The untreated sample has a cleaner morphology, while the micrograph of the processed sample shows changes on the surface of the fibers in the form of surface stratification, peeling, deposits, which are not present on the untreated sample.



**Figure 2.** Micrographs of PES fiber samples in the enzyme treatment mode. a) untreated sample; b) sample treated with papain enzyme

A similar behavior was observed in the paper of Kardas *et al.* [10], where the tests performed by SEM showed differences in the appearance of the fiber surface before and after modification of poly(ethylene terephthalate) fibers from the point of view of changes in their surface structure in terms of

its micro-topography. The tests performed by SEM showed differences in the appearance of the fiber surface before and after modification (smoothing or increased roughness), depending on the type of enzyme preparation, lipase or esterase used.

The first thing that can be noticed after the modification of polyester is the loss in mass due to the hydrolysis of the fiber surface (up to 2.1%) caused by the action of papain enzymes, Table 1.

**Table 1.** Comparative results of the examined parameters of PES fabric in the papain enzyme treatment mode

Examined parameter	Values of results	
	Untreated sample	Treated sample
Loss of mass, %	0	2.1
Capillarity, warp direction, mm	0	14
Absorption, %	127	141
Wetting time, s	290	13
Breaking strength, warp direction, daN	149	140
Breaking elongation, warp direction, %	40	43

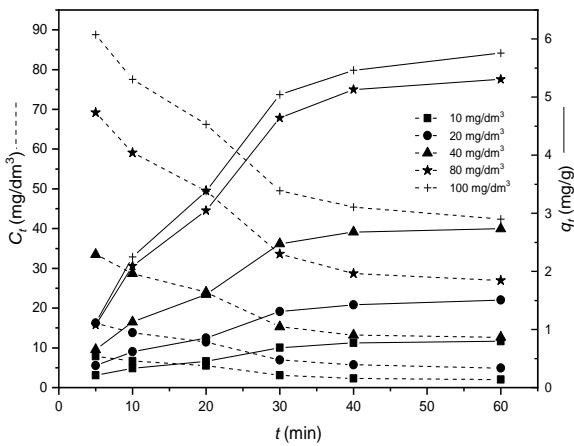
The following fiber properties on which enzymatic hydrolysis can have a significant effect are those that improve wetting: water penetration, water adsorption or wetting, Table 1. Water penetration in the direction of the warp threads is far higher (14 mm) in comparison to the untreated fabric (0 mm). The absorption of water by PES fabric confirms that the treated samples give better results, about twenty percent higher than the untreated sample.

The papain enzyme treatment improves the surface wetting ability of hydrophobic PES fibers. Such an improved wettability was attributed to the increasing number of polar groups, surface deformation, increased surface roughness of the material, etc. According to Table 1, the untreated sample of PES fabric has by far the slowest wetting of 290 s; in processed samples the average time of wetting is 13 s.

Mechanical properties, breaking strength and elongation, show a change, strength decreases and elongation increases slightly, which is a direct consequence of surface modification of fibers by the papain enzyme.

The influence of time of contact between adsorbate (dye) and adsorbent (PES fiber modified with papain enzyme) on the change of dye concentration (dashed line of curves) and adsorption capacity (full line of curves) is shown in the diagram in Figure 3. There is continuity in the changes of adsorption capacity ( $q_t$ ) over time, i.e. longer dyeing time causes a higher amount of adsorbed dye per unit

mass of adsorbent, reaching a maximum at 60 min. During dyeing, the concentration of the disperse dye ( $C_t$ ) decreases evenly, initially faster and then slower, reaching a minimum at the equilibrium time.

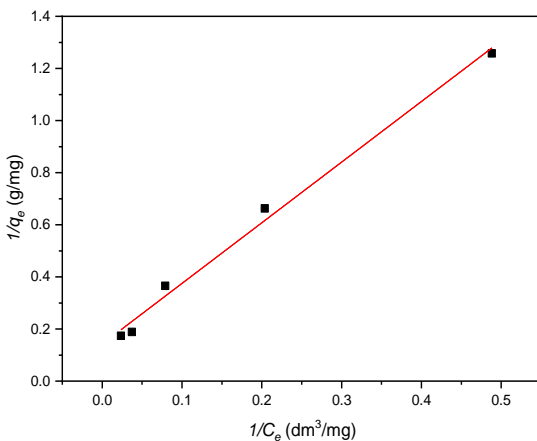


**Figure 3.** The influence of adsorption time on the change in the initial dye concentration and adsorption capacity

Linear regression was used to determine the best fitted isotherm, while the least squares method was used for finding the parameters.

The diagram in Figure 4 represents a linear interpretation of the *Langmuir* adsorption isotherm. There is a slight scattering of the measured values around the fitted curve, which indicates the adequacy of the *Langmuir* isotherm to describe the adsorption equilibrium of the tested system.

According to the results of this empirical model for a specific system, it is assumed that adsorption occurred only at a limited number of definitively localized sites on the fiber, and the adsorbed layer consisted of only one molecule of dye (monolayer adsorption).

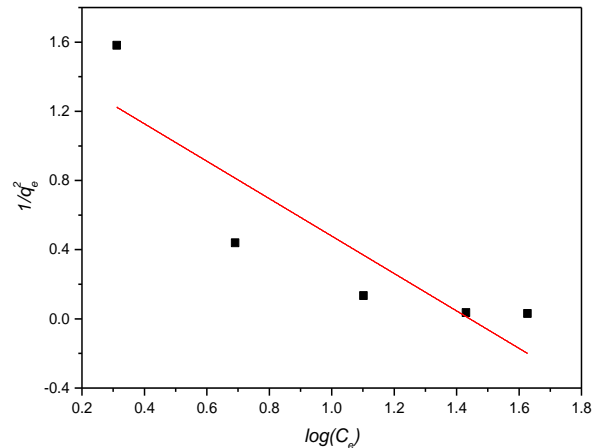


**Figure 4.** *Langmuir* adsorption isotherm for the system of disperse dye-PES.

Similar conclusions were made by other researchers examining the dyeing of polyester fiber, where the application of the *Langmuir* isotherm proved to be an excellent model for explaining the dyeing-sorption of the disperse dye [11].

The diagram in Figure 5 illustrates the *Harkins-Jura* model. It is noted that the fitting curve passes far from the experimental points, which leads to the conclusion that this isotherm cannot be accepted for the description of dyeing modified polyester with disperse dye. In the specific case, according to the presented *Harkins-Jura* isotherm, there is no multilayer adsorption, polyester fibers do not represent a heteroporous material and there is no heterogeneous pore distribution on the adsorbent-fiber surface.

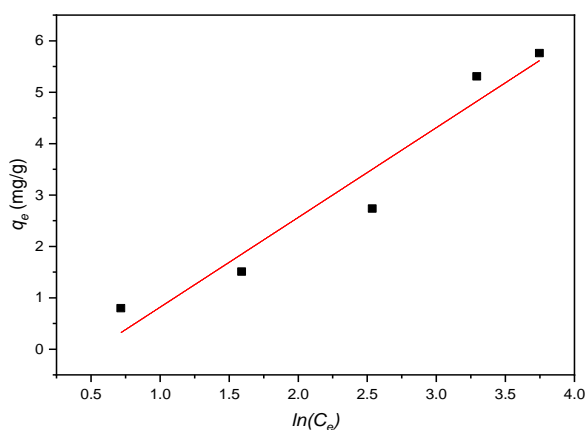
This confirms the applicability of the *Langmuir* isotherm, which implies monolayer adsorption, and therefore there is no multilayer adsorption that dominates in the *Harkins-Jura* model.



**Figure 5.** *Harkins-Jura* adsorption isotherm for the system of disperse dye-PES.

The diagram in Figure 6 represents the *Temkin* isotherm of adsorption, the linear regression curve fits relatively well the experimental points. According to this model, the heat of adsorption of all molecules of the disperse dye on the surface of PES fibers decreases linearly with increasing degree of coverage and adsorption is characterized by a uniform distribution of binding energy of molecules on the surface of the adsorbent.

Table 2 shows the analytical expressions of the used *Langmuir*, *Harkins-Jura*, and *Temkin* models with numerous values of characteristic constants, i.e. isotherm parameters. Also, the value of the statistical parameter is given, the coefficient of determination  $R^2$ , on the basis of which the validity is evaluated, i.e. the applicability of the models used.



**Figure 6.** Temkin adsorption isotherm for the system of disperse dye–PES

According to the results, the leading *Langmuir* isotherm with the highest value of  $R^2$  (0.992), is followed by the *Temkin* and *Harkins-Jura* models (0.940 and 0.782, respectively). The *Langmuir* parameter, adsorption energy,  $b$ , related to the apparent energy (surface energy) of sorption, has a relative value of  $0.06 \text{ dm}^3/\text{mg}$ , i.e. low surface energy in the system, which indicates a more probable connection between disperse dyes and PES fibers.

The characteristics of the *Langmuir* isotherm can also be expressed by a dimensionless constant, the equilibrium parameter  $R_L$ . From the values for  $b$

(Table 2) and the highest initial concentration of disperse dye ( $100 \text{ mg}/\text{dm}^3$ ), the parameter  $R_L$  was calculated to be between 0 and 1, i.e. it is 0.14, on the basis of which it can be concluded that it is an isotherm suitable for describing a specific dyeing process.

In the process of determining the dye retention capacity and affinity of the dye adsorbent, the *Langmuir* monolayer model adequately covers the experimental data and may be absolutely acceptable for adsorption of the applied disperse dye on enzyme-treated PES fabric. On the other hand, the *Harkins-Jura* model is not acceptable for a specific system due to the much lower value of  $R^2$ . According to the results of the *Temkin* model, it seems that adsorption is characterized by a uniform distribution of binding energies, and the heat of adsorption of all molecules in the layer decreases linearly with coverage due to the adsorbate-adsorbate interaction. The value of heat of adsorption ( $b_T$ ) for the observed system is  $1.77 \text{ kJ}/\text{mol}$ , which indicates a weak interaction between the dye and the fibers, and the process of interaction was manifested by physical adsorption (physi-sorption). It is a fact that the typical range of binding energy for the ion exchange mechanism (chemi-sorption) is between 8 and 16  $\text{kJ}/\text{mol}$  [12].

**Table 2.** Analytical expressions and parameters of the used models for the description of adsorption of the disperse dye for the modified PES fiber.

Model	Analytical expression of the model	Model parameters		$R^2$
<i>Langmuir</i>	$\frac{1}{q_e} = 0.14 + 2.33 \cdot \frac{1}{C_e}$	$Q_0$ (mg/g)	7.03	0.992
		$b$ ( $\text{dm}^3/\text{mg}$ )	0.06	
		$R_L$	0.14	
<i>Harkins-Jura</i>	$\frac{1}{q_e} = 1.56 + 1.08 \cdot \log(C_e)$	$B_{HJ}$	1.44	0.782
		$A_{HJ}$	0.92	
<i>Temkin</i>	$q_e = -0.93 + 1.75 \cdot \ln(C_e)$	$K_T$ ( $\text{dm}^3/\text{mg}$ )	0.59	0.940
		$B_T$	1.75	
		$b_T$ ( $\text{kJ}/\text{mol}$ )	1.77	

## CONCLUSIONS

Modification of the surface of polyester fibers by the papain enzyme has led to an improvement in the hydrophilicity of the highly hydrophobic and crystalline fiber. In addition to the influence on the sorption characteristics, there is also positive influence on the ability to dye polyester material. Micrograph of the processed PES sample shows changes on the surface of the fibers in the form of

surface stratification, which are not present on the untreated sample.

Modeling of disperse dye adsorption, i.e. dyeing of PES fabric was tested under different conditions without carriers in the dyeing bath. It was found that adsorption depends on the time of contact, the initial concentration of the dye, as well as on the fact that it is a monolayer adsorption on a homogeneous surface. The value of heat of adsorption indicates a weak interaction between the dye and the fibers, and

the process of interaction was manifested by physical adsorption (physi-sorption).

The results of this study suggest the possibility of different approaches in the dyeing process with polyester-disperse dye, all in favor of greater efficiency and cost-effectiveness, as well as environmental protection.

#### REFERENCES

1. A. Pellis, C. Gameraith, G. Ghazaryan, A. Ortner, E. H. Acero, G. M. Guebitz, *Bioresour. Technol.*, **218**, 1298 (2016).
2. B. Mu, H. Xu, Y. Yang, *Color. Technol.*, **133**, 415 (2017).
3. A. Robic, C. Ullmann, P. Auffray, C. Persillon, J. Martin, *OCL*, **24**, 1 (2017).
4. T. Teeraphatpornchai, T. Nakajima-Kambe, Y. Shigeno-Akutsu, M. Nakayama, N. Nomura, T. Nakahara, H. Uchiyama, *Biotechnol. Lett.*, **25**, 23 (2003).
5. Y. Welde, A. Worku, *J. Med. Plants Stud.*, **6**, 127 (2018).
6. G. M. Guebitz, A. Cavaco-Paulo, *Curr. Opin. Biotechnol.*, **14**, 577 (2003).
7. G. Fischer-Colbrie, S. Heumann, S. Liebmingner, E. Almansa, A. Cavaco-Paulo, G. M. Fuebitz, *Biocatal. Biotransform.*, **22**, 341 (2004).
8. M. Arslan, M. Yigitoglu, *J. Appl. Polym. Sci.*, **107**, 2846 (2008).
9. A. G. Shirke, P. Parekh, B. Dholakiya, K. Kuperkar, *J. Surfactants Deterg.*, **21**, 187 (2018).
10. I. Kardas, B. Lipp-Symonowicz, S. Sztajnowski, *J. Appl. Polym. Sci.*, **119**, 3117 (2011).
11. S. Dhouib, A. Lallam, F. Sakli, *Text. Res. J.*, **76**, 271 (2006).
12. V. K. Gupta, A. Mittal, A. Malviya, J. Mittal, *J. Colloid Interface Sci.*, **335**, 24 (2009).



## Spectroscopic and thermodynamic characterization of the chemotherapy drug Epirubicin interaction with human serum albumin

S. Abarova<sup>1\*</sup>, B. Antonova<sup>1</sup>, K. Stoichkova<sup>2</sup>, N. Nakova<sup>3</sup>, P. Abarov<sup>4</sup>, A. Zasheva<sup>1</sup>, R. Koynova<sup>5</sup>, B. Tenchov<sup>1</sup>

<sup>1</sup> Department of Medical Physics and Biophysics, Medical University-Sofia, 1431 Sofia, Bulgaria

<sup>2</sup> Faculty of Physics, Sofia University „St. Kliment Ohridski“, Sofia, Bulgaria

<sup>3</sup> UMBAL „St. Ivan Rilski“, Sofia, Bulgaria

<sup>4</sup> Faculty of Science and Engineering, Maastricht University, The Netherlands

<sup>5</sup> Ohio State University, College of Pharmacy, Columbus OH, USA

Received: June 10, 2021; Revised: February 24, 2022

In the present work we studied the interactions of the chemotherapy drug Epirubicin (Epi) with human serum albumin (HSA) by fluorescence spectroscopy and differential scanning calorimetry (DSC). The Epi-HSA binding parameters were evaluated by the fluorescence quenching method. As shown by intensity measurements, Epi strongly quenched the intrinsic HSA fluorescence. The calculated Stern-Volmer quenching constant  $K_{sv}$ , the association binding constant  $K_a$  of the Epi-HSA complex, as well as the thermodynamic parameters, including  $\Delta H^\circ$ ,  $\Delta S^\circ$  and  $\Delta G^\circ$  indicated that hydrophobic forces play a major role in the interaction of Epi with HSA. These measurements point to a quenching mechanism based on Epi-HSA static complex formation rather than to dynamic collisions. This conclusion well agrees with the DSC heat capacity profiles which showed a strong increase of the post-denaturation HSA aggregation with increase of the Epi concentration. This work provides new insights into the mechanism of Epi-HSA interactions and contributes to a better understanding of the effects of chemotherapy drugs on the stability and structural modifications of the carrier blood plasma proteins.

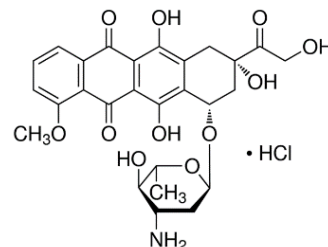
**Keywords:** Epirubicin; human serum albumin; fluorescence spectroscopy; differential scanning calorimetry; quenching; drug binding

### INTRODUCTION

The pharmacokinetics and pharmacodynamics of any drug will strongly depend on its interaction with human serum albumin (HSA), the most abundant plasma protein. HSA is an important carrier of exogenous and endogenous molecules in human blood plasma. It has high binding affinity to many drugs and thus facilitates their transport throughout the blood circulation [1-3]. The nature of the binding has direct consequences on drug delivery, pharmacokinetics, pharmacodynamics, and therapeutic efficacy. Epirubicin hydrochloride (Epi, Fig. 1) is an anthracycline drug used in the treatment of a range of neoplastic conditions including breast carcinoma and gastric cancer. It can be administered in combination with other medications to treat breast cancer in patients who have had surgery to remove the tumor. Epirubicin acts by intercalating DNA strands and generating free radicals that cause cell and DNA damage. Binding to cell membranes and plasma proteins may be involved in the compound's cytotoxic effects.

Several reports have shown that the mechanism of Epi action appears to be related to its ability to bind to nucleic acids. Epi was found to bind

differently to the various plasma proteins *in vitro*, and *in vivo* [5-7].



**Figure 1.** Chemical structure of Epirubicin hydrochloride (synonyms 4'-Epidoxorubicin hydrochloride, Epidoxorubicin hydrochloride [4]).

The *in vitro* binding rate of Epi to plasma proteins, namely alpha-HSA, gamma-HSG, alpha+beta-HSG and with isolated human red blood cells was shown to depend on the concentration of the matrix components, but no evidence is available on how Epi interacts with blood plasma proteins upon intravenous infusion. We thus decided to investigate here the fluorescence and DSC profiles of HSA upon binding of medication Epi and to use these profiles for the characterization of the Epi-HSA interaction parameters. With regard to its biological relevance, the present study demonstrated that there are significant changes in the fluorescence

\* To whom all correspondence should be sent:  
E-mail: sabarova@medfac.mu-sofia.bg

and DSC properties/parameters that may serve to evaluate the therapeutic effectiveness of anti-cancer drugs such as Epirubicin.

## MATERIALS AND METHODS

Stock solutions of fatty acid-free human serum albumin and Epirubicin hydrochloride solution for injection (2 mg/ml) were prepared in PBS, pH 7.4, and in saline for the fluorescence spectroscopy study and for DSC measurements, respectively.

### Fluorescence spectroscopy

A Scinco 2 South Korea spectrofluorimeter was used to measure fluorescence spectra with a 1.0 cm quartz cuvette. Bandwidths for both excitation and emission were 5 nm. Epi–HSA fluorescence measurements were carried out by keeping the concentration of HSA fixed at 4  $\mu\text{M}$  and those of Epi were 7, 14, 27, 54, 68  $\mu\text{M}$ . Fluorescence spectra were recorded at two different temperatures of 25 and 37  $^{\circ}\text{C}$  in the spectral emission range 300–500 nm upon excitation at 283 nm ( $n = 5$  replicates).

### Differential scanning calorimetry (DSC)

Thermal denaturation of HSA in the absence and presence of different Epi concentrations was studied by Nano DSC from Thermal Analysis Instruments with 300  $\mu\text{l}$  measuring cell volume. For each sample, two consequent heating scans were performed at a scan rate of 1 K/min in the range of 0–110 $^{\circ}\text{C}$ . To investigate the thermal transitions ongoing in the native samples, the second heating scans corresponding to denatured samples were used as baseline and were subtracted from the first heating scans of the native samples.

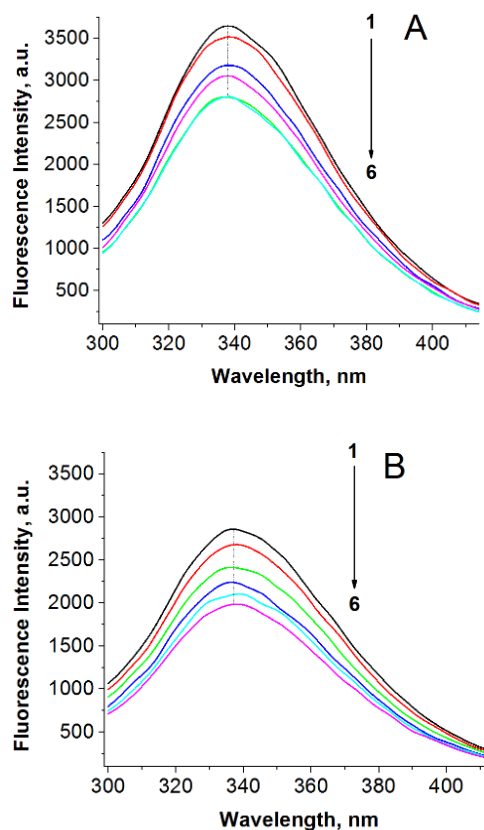
## RESULTS AND DISCUSSION

### Fluorescence spectroscopy

**Fluorescence quenching.** It is well known that HSA intrinsic fluorescence is due to the presence of specific amino acids, mainly tryptophan (Trp) and tyrosine (Tyr) residues [8]. The binding of a ligand to a protein may directly affect the fluorescence of a tryptophan residue by acting as a quencher or by interacting with the fluorophore, dynamically changing the polarity of its surrounding conditions. The fluorescence intensity of a compound can be decreased by several types of molecular interactions including excited-state reactions, energy transfer, collisional quenching, molecular rearrangements, and ground state complex formation. The different mechanisms of quenching are usually classified as either dynamic quenching or static quenching. Dynamic and static quenching can be distinguished

by their temperature and viscosity dependencies [9, 10].

In our study, the interaction between Epi and HSA was investigated upon exciting HSA at 283 nm where both Trp and Tyr residues get excited [11, 12]. The variations of the emission spectra of solutions at fixed HSA concentration and varying Epi concentrations at 25 and 37  $^{\circ}\text{C}$  are presented in Figure 2.



**Figure 2.** Fluorescence titration curve of HSA (4  $\mu\text{M}$ ) with the Epi complex in PBS, pH 7.4, at A. 25  $^{\circ}\text{C}$  and B. 37  $^{\circ}\text{C}$ . Curves 1–6 correspond to Epi concentrations of 0, 7, 14, 27, 54, 68  $\mu\text{M}$ , respectively.

As is clear from Figures 2A and 2B, the intrinsic fluorescence spectra of HSA were strongly quenched by Epi addition at both temperatures. There is no significant shift of the maximum emission wavelength at 338 nm implying that the interaction of Epi with HSA does not affect the conformation of the region surrounding the Tyr and Trp residues [9].

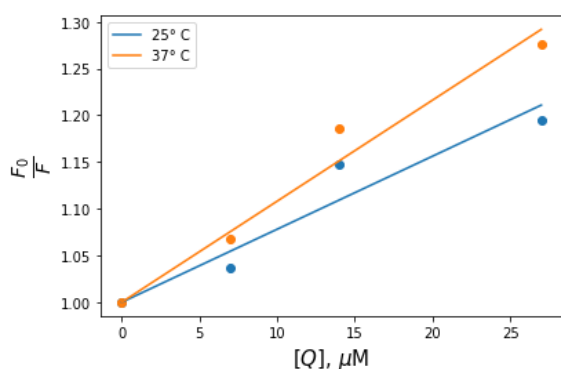
To analyze the fluorescence quenching mechanism, the quenching data about HSA were evaluated using the classical Stern-Volmer equation (eq. 1):

$$\frac{F_0}{F} = 1 + K_{SV}[Q] = 1 + K_q \tau_0 [Q] \quad (1)$$

where  $F_0$  and  $F$  are the fluorescence intensities in the absence and presence of a quencher, respectively,  $Q$  is the total concentration of the quencher (Epi), and  $K_{SV}$  is the Stern-Volmer quenching constant.  $K_q$  and  $\tau_0$  are the quenching rate constant, and the average lifetime of the biomolecule without quencher, respectively. Since the fluorescence lifetime of the biopolymer is  $\sim 10^{-8}$  s [13], the quenching rate constant,  $K_q$  can be calculated using equation (2):

$$K_q = \frac{K_{SV}}{\tau_0} \quad (2)$$

The intensity changes are given in Stern–Volmer representation (Figure 3). From the plots of  $F_0/F$  vs.  $Q$  the type of quenching can be determined, i.e., these plots can be either linear for static or dynamic quenching, or display upward bent curve for mixed quenching types [9].



**Figure 3.** Stern-Volmer plot for quenching of different Epi concentrations (7-27  $\mu\text{M}$ ) to HSA (4  $\mu\text{M}$ ) in PBS solution at 25 and 37  $^{\circ}\text{C}$ .

The Stern–Volmer plot of the fluorescence quenching shows complex or mixed interactions. If the interaction is either poorly dynamic or static, the Stern–Volmer plot of the intensity gives a linear correlation between the quencher concentration and the intensity.

For the linear plots obtained in the present study, the Stern-Volmer quenching constant  $K_{SV}$  can be calculated using equation (1). In order to obtain values for the fluorescence quenching constant we used the Nedler-Mead simplex algorithm to fit a linear regression model to  $F_0/F$  and  $Q$  for the first four values of Epi (0-27  $\mu\text{M}$ ). The values for  $K_{SV}$  at two temperatures are given in Table 1.

**Table 1.** Stern-Volmer quenching constants  $K_{sv}$ , and quenching rate constant  $K_q$  for HSA complexes with Epi.

Temperature, $^{\circ}\text{C}$	$K_{sv}$ , $[10^4 \text{ M}^{-1}]$	$K_q$ , $[10^{12} \text{ M}^{-1}\text{s}^{-1}]$
25	0.78	0.78
37	1.08	1.08

It can be seen that, upon increasing the temperature from 25 to 37  $^{\circ}\text{C}$ , the values of  $K_{SV}$  were not significantly increased suggesting that the Epi does not act as a dynamic quencher (1). The calculated values of  $K_q$  were greater than the limiting diffusion rate constant of the biomolecule ( $2 \times 10^{10} \text{ L}\cdot\text{mol}^{-1}\cdot\text{s}^{-1}$ ). This implied that the quenching was not induced by dynamic collisions but rather originated from the formation of a ground-state complex, and indicated that the probable quenching mechanism of fluorescence of HSA by the Epi is a static quenching procedure [14].

The quenching results were also analyzed using the modified Stern-Volmer equation [13]:

$$\frac{\log(F_0 - F)}{F} = \log K_a + n \log[Q] \quad (3)$$

where  $K_a$  and  $n$  are the binding constant and number of binding sites, respectively.

The value of  $K_a$  is important to understand the affinity of the drug to plasma proteins. The binding of Epi to HSA is of importance as it changes the pharmacological activity of the drug. It is known that protein-binding may alter drug activity in two different ways: by changing the plasma drug effective concentration at its site of action or by changing the rate at which the drug is eliminated, thus changing the length of time for which effective concentrations are maintained. Thus, weak binding can lead to a short-lived protein-ligand complex, while strong binding can decrease the concentrations of the free drug in plasma.

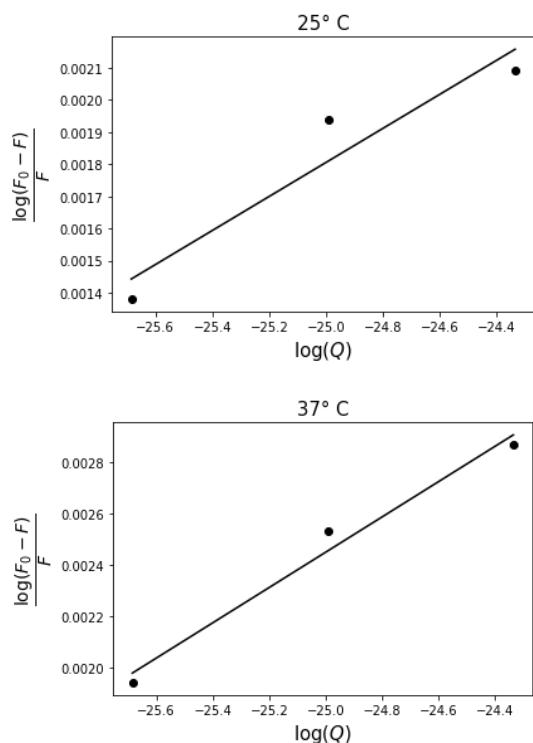
The values of  $K_a$  and  $n$  for the Epi-HSA complex were calculated from the intercept and slope of the plot of  $\log(F_0 - F)/F$  vs.  $\log[Q]$  (Table 2).

**Table 2.** Binding constants  $K_a$  of Epi–HSA at two different temperatures.

Temperature, $^{\circ}\text{C}$	$K_a$ , $[10^{-4} \text{ M}^{-1}]$
25	5.29
37	6.88

The plots for a representative system, Epi–HSA at the two different temperatures are given in Figure 4.

It should be noted that the binding constant values slightly increased with increasing temperature which suggests that at higher temperatures the increased mobility inside the serum albumin structure allows the ligand to find improved binding within the protein pocket. The binding constants calculated for Epi–HSA suggest low affinity of the drug-albumin binding.



**Figure 4.** Modified Stern-Volmer plots for the EPI-HSA complex at A. 25 and B. 37 °C.

*Thermodynamic parameters.* There are several kinds of binding forces that might occur between the drug and the biomolecule. Thermodynamic enthalpy change ( $\Delta H^0$ ), entropy change ( $\Delta S^0$ ), and free energy change (Gibbs energy  $\Delta G^0$ ), provide estimable information in studying the interaction between the biomolecule and the drug. These values are an indicator of the prevalent driving forces associated with the binding [14].

To depict the intermolecular forces existing between Epi and HSA, the temperature-dependent thermodynamic system was utilized and evaluated at 25 and 37 °C. After estimating the binding parameters, the van't Hoff equation (equation (4)) provides the different thermodynamic parameters of the complexes [14]:

$$\ln K_a = -\frac{\Delta H^0}{RT} + \frac{\Delta S^0}{T} \quad (4)$$

The values of  $\Delta G^0$  can be obtained from the binding constants  $K_a$  at the two different temperatures [16]:

$$\Delta G^0 = \Delta H^0 - T\Delta S^0 = -RT \ln K_a \quad (5)$$

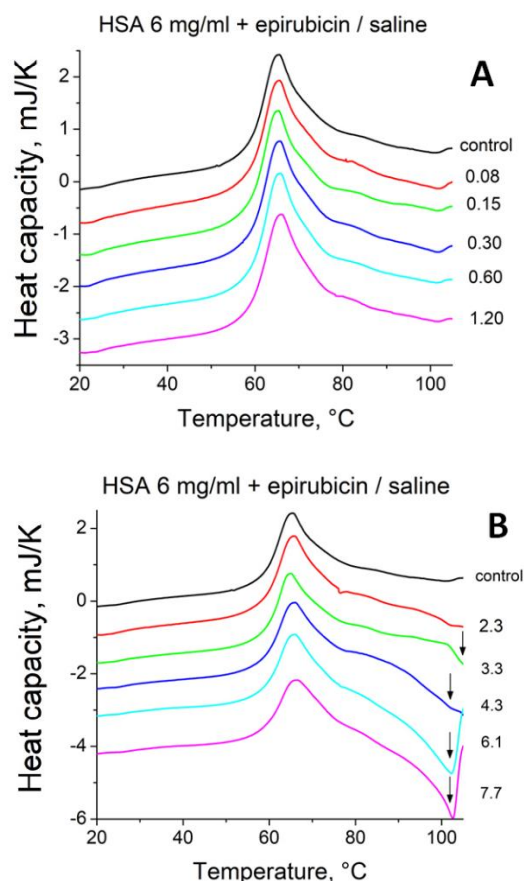
where  $K_a$  represents the binding constant at its corresponding temperature and  $R$  is the gas constant.  $\Delta G$  can be determined using van't Hoff plot, where  $\Delta H^0$  is the slope and  $\Delta S$  the intercept.

In our experiments the binding process was connected with positive changes in enthalpy and

Gibbs energy ( $\Delta H^0 > 0$  and  $\Delta G^0 > 0$ ), that indicate a non-spontaneous hydrophobically associated process [16]. In our study, a partial immobilization of the protein and the ligand is related to the obtained positive  $\Delta H^0 = 11.77$  kJ/M due to hydrophobic association processes, and partially offset by the negative  $\Delta S^0 = -6.45$  J.M<sup>-1</sup> due to the loss of translation and rotation (if any) in the hydrophobically associated species [16]. The non-spontaneous binding of drug to the biomolecule is represented by the positive sign of  $\Delta G^0 = 18.69$  kJ M<sup>-1</sup> and  $\Delta G^0 = 18.76$  kJ M<sup>-1</sup> at the two temperatures (25 and 37 °C), respectively [16].

#### Differential scanning calorimetry (DSC)

The DSC results of the influence of increasing Epi concentrations on the HSA denaturation heat capacity profile are summarized in Figure 5.



**Figure 5.** Heat capacity profiles obtained by DSC of Epi-HSA mixtures. The numbers on the right of the thermograms show the Epi-HSA molar ratio. The arrows in panel B point to the regions of post-denaturation HSA aggregation at high Epi-HSA ratios. The thermograms in panels A and B are vertically displaced for clarity.

They show that in the range of low Epi-HSA molar ratios (up to about 1.2 Epi molecules per one HSA molecule, Fig. 5A) Epi does not noticeably

affect the HSA denaturation profiles relative to the control, in accord with the conclusion derived from the fluorescence data about low affinity binding of the drug to HSA. However, a stronger Epi-HSA interaction takes place at higher Epi-HSA molar ratios in the range of Epi-HSA above 2 (Fig. 5B). In the latter range Epi brings about a well expressed post-denaturational HSA aggregation displayed in the downward exothermic slopes of the heat capacity curves at high temperatures (indicated by the arrows in Fig. 5B). The enhanced HSA aggregation might result from exposure of additional non-polar HSA regions upon denaturation taking place at high Epi concentrations that substantially exceed the 1:1 Epi-HSA molar ratio. This conclusion is also in accord with the fluorescence results indicating a predominant role of the hydrophobic interactions in the formation of the Epi-HSA complexes.

### CONCLUSIONS

The interaction between Epirubicin, a frequently used antitumor drug, and human serum albumin, a blood plasma carrier protein, was studied at different temperatures by fluorescence spectroscopy and differential scanning calorimetry (DSC) techniques.

Fluorescence quenching results revealed the formation of static complexes between Epi and HSA. The binding was determined to be due to hydrophobic interactions. The Epi binding to HSA resulted in significant alterations of the HSA structure and conformation displayed in decreasing protein stability and an increase of the non-polar or accessible hydrophobic surface of HSA to solvent. The significant post-denaturation HSA aggregation at high Epi concentrations revealed by DSC well agrees with the conclusions based on the fluorescence quenching data suggesting low binding affinity of Epi to HSA. The observed effects are of certain interest as they may influence the balance \*between bound and freely circulating drugs in cases

of simultaneous Epi application with other drugs, thus affecting the drug pharmacokinetics, efficacy and adverse side impact. This study helps to gain useful insights into the significance of the binding of anti-cancer drugs with the most abundant plasma carrier protein, serum albumin, on the drug overall distribution and pharmacological activity.

**Acknowledgement:** This work was supported by Grant D-241/19. 12. 2019 by SMN at the Medical University-Sofia.

### REFERENCES

1. G. Fanali, A. di Masi, V. Trezza, M. Marino, M. P. Fasano, *Mol Aspects Med.*, **33** (3), 209 (2012).
2. U. Kragh-Hansen, *Dan. Med. Bull.*, **37**(1), 57 (1990).
3. D. C. Carter, J. X. Ho, *Adv Protein Chem.*, **45**, 153 (1994).
4. <https://www.sigmaaldrich.com/catalog/product/sial/e0550000?lang=en&region=BG>.
5. S. Bhaduri, N. Ranjan, D. P. Arya, *Beilstein Journal of Organic Chemistry*, **14**, 1051 (2018).
6. I. Pernkopf, *Pharmazie*, **51**(11), 897 (1996).
7. S. Bandak, *Z. Naturforsch. C, J. Biosci.*, **49** (7-8), 483 (1994).
8. F. Yang, Y. Zhang, *Int. J. Mol. Sci.*, **15**, 3580 (2014).
9. Protein Fluorescence, in: J. R. Lakowicz (ed.) *Principles of Fluorescence Spectroscopy*. Springer, Boston, MA, (2006).
10. M. R. Eftink, Fluorescence quenching reactions, in: *Biophysical and biochemical aspects of fluorescence spectroscopy*, T. G. Dewey (ed.), Springer, New York, USA, 1991, p. 1.
11. F. W. Teale, G. Weber, *The Biochemical Journal*, **65** (3), 476 (1957).
12. J. M. Antosiewicz, D. Shugar, *Biophys. Rev.*, **8**, 163 (2016).
13. J. R. Lakowicz, G. Weber, *Biochemistry*, **12**, 4161 (1973).
14. G. Sudlow, D. Birkett, D. Wade, *Mol. Pharmacol.*, **12**, 1052 (1976).
15. Y. Ni, G. Liu, S. J. Kokot, *Talanta*, **76**, 513 (2008).
16. P. D. Ross, S. Subramanian, *Biochemistry*, **20** (11), 3096 (1981).

## Extraction of underexploited *Vernonia cinerea* oil with comparative pretreatment techniques for conversion into biodiesel

N. Umairambika<sup>1</sup>, N. Arunodhaya<sup>2</sup>, S. Renganathan<sup>1\*</sup>

<sup>1</sup> Biofuels Lab, Centre for Biotechnology, A. C. Tech, Anna University, Chennai, India

<sup>2</sup> Department of Petroleum Engineering, Rajiv Gandhi College of Engineering, Sriperumbudur, India

Received: July 21, 2021; Revised: March 28, 2022

An examination by a conventional Soxhlet method and pretreatment by ultrasonication was performed for the oil extraction from non-edible *Vernonia cinerea* seeds. Pretreatment was conducted by ultrasonication, microwave and autoclave methods. After optimizing the process parameters, ultrasonication provided the best results with a yield of 40.9%. A study on the kinetics of oil extraction was performed. The first-order kinetics was found to fit for the oil extraction with activation energy of 82.2 kJ/mol. The physical and chemical properties of the extracted oil were determined by ASTM method and all properties fit within the requisite limits for the production of biodiesel. The oil was subjected to two-step transesterification process and biodiesel produced was within standard limits.

**Keywords:** Pretreatment, ultrasonication, extraction, *Vernonia cinerea*, kinetic studies, biodiesel

### INTRODUCTION

Fossil fuels are in the depletion phase and the pollution created by ignition of such non-renewable fuels is highly hazardous to the environment. Biodiesel is fuel which would be a solution to overcome the above mentioned constraints. Due to the heavy demand prevailing all over the world, biomass provides a wide choice as the feedstock for production of alternate renewable fuels [1]. Biodiesel production from different biomass sources has grabbed the limelight in the recent years. In particular, non-edible seeds have been proved undeniably as a second-generation resource for the production of biodiesel [2]. The prime reason for its significance is that no major cost of input is utilized for the raw materials, as these seeds are plentifully available in tropical regions.

The oil extracted from the seeds of plants consists of a combination of saturated and unsaturated fatty acids, the significant biomolecules of which have to be brought under the focus of research. These biomolecules may serve as good raw materials in pharmaceutical, food and cosmetic industries [3-5]. If the lipid content of the extracted oil meets the fuel standards, it is a welcome source for the production of biodiesel. For the current economic situation pertaining in the world, voluminous scale of biodiesel production would help saving in foreign exchange [6, 7].

Proper selection of feedstock is the major parameter in production of biodiesel as the production cost could be excised to a great extent,

which leads to economical and feasible production. Seeds have to be chosen as the feedstock for transesterification process in such a way that the oil yield is above 20 % [8]. The degree of unsaturation of fatty acid in the raw oil extracted determines the cetane number, iodine value and oxidation stability. These are the key factors that ascertain the fuel standards [9].

In the present investigation *Vernonia cinerea* is the chosen seed for the extraction of oil. This is a novel seed as no earlier works have been documented for extraction of oil from *Vernonia cinerea*. It belongs to Asteraceae family. The objective pertains to the optimum yield of oil using Soxhlet extraction method which is the conventional and the best method for oil extraction. Pretreatments are performed using autoclave [10], ultrasonication [11-13] and microwave assistance methods [12] for enhancement of lipid extraction. Comparative studies on the highest oil yield using the mentioned pretreatment methods are deliberated.

The extracted oil is the lipid source which can be converted into FAME. No research work has been carried out earlier in conversion of *Vernonia cinerea* oil into biodiesel. In the present work all the key parameters, namely particle size of the chosen seeds, their moisture content, the best solvent utilized for extraction, the solvent-to-solid ratio and the extraction temperature required for conformity to be used as lipid source for biodiesel production, were studied. The biodiesel obtained from the transesterification reaction of the extracted *Vernonia cinerea* oil can be utilized as a fuel for automobiles.

\* To whom all correspondence should be sent:  
E-mail: srenganathan@annauniv.edu

## MATERIALS AND METHODS

### Extraction of oil

*Vernonia cinerea* plants are copiously available even in the barren lands all throughout the year. The seeds collected were sun-dried. The solvents n-hexane, chloroform, petroleum ether, acetone, isopropanol and dichloromethane of analytical grade with purity of 99.9% required for oil extraction were purchased from SRL Chemicals private ltd. Mumbai, India.

For the maximum extraction yield of oil, the moisture content in the seeds has to be negligible. To remove the excess moisture, the seeds were kept in a hot-air oven at 60°C for 20 min. The moisture content of the seeds was determined using the formula:

$$\text{Moisture content} = \frac{\Delta W}{W_i} \times 100 \% \quad (1)$$

where  $\Delta W$  = difference between initial and final weight of the seed,  $W_i$  = initial weight of seed.

The seeds were then crushed to fine powder using a crusher. Mechanical sieving was later performed for uniform segregation of the powders.

### Pretreatment methods

Pretreatment was performed to improve the extraction yield of oil. The outer wall breaks thereby providing a better interaction with the solvent for extraction. Three options of pretreatment were chosen.

#### Microwave assistance pretreatment

Microwave assistance pretreatment was performed with a 1200 W microwave oven (Model No. IFB 23SC3IFB). Whole seeds (10 g) were arranged randomly on a petri dish placed in the middle of the turn table of the microwave oven. The pretreatment by microwave irradiation was carried out for 30 sec [14].

#### Pretreatment using autoclave

The seeds were autoclaved at 121°C and at a pressure of 15 lbs. The presence of excess thermal stress prompts the rupture of cell walls inducing the release of intracellular lipids. After the pretreatment the seeds were brought back to room temperature [15].

#### Ultrasonication pretreatment

Ultrasonication was carried out using ultrasonic probe at 24 KHz (Model No: Sonics vibra cell 500 watts) with 10 sec of on and off cycle at constant room temperature. As solvents n-hexane, petroleum ether and chloroform were tested. The best solvent was used for pretreatment. The change in solid-to-solvent ratio (1:2-1:4 g/ml) and the ultrasonication time (2.5 - 15 min) were further studied [12].

Soxhlet apparatus was employed for extraction of oil from pretreated biomass. The organic solvent chosen for extraction was taken in a double-neck round-bottomed (RB) flask. The Soxhlet extractor was fixed to the center neck of the RB flask and the other end of the extractor was connected to a bulb condenser. Water inlet and outlet was provided on either ends of the condenser. The biomass of known weight was packed in the thimble. The entire set-up was placed in a heating mantle. Temperature was maintained little above the boiling point of the organic solvent chosen. Thermometer was inserted in the side neck of the RB flask to check the temperature of the system. The vaporized solvent moved up and on condensation dripped back to the thimble and got in contact with the biomass. Extraction of oil occurred here and the volume of solvent rose inside the thimble. Once the chamber was filled with the solvent, it flowed back to the RB flask through the side siphon tube. The extraction process was continued for 'n' cycles and the important parameters were optimized for highest yield of oil [16]. The solvent was removed by using a rotary evaporator. The extracted oil was stored in tightly packed vials. The yield of oil was calculated using equation 2:

$$\text{Yield of oil (\%)} = \frac{\text{weight of oil (g)}}{\text{weight of seed powder (g)}} \times 100\% \quad (2)$$

### Biodiesel synthesis

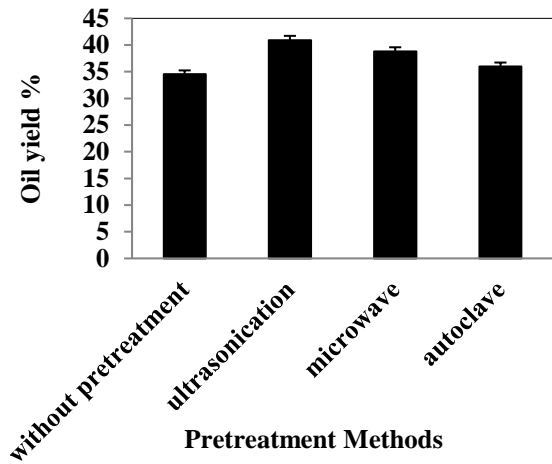
To check the conversion of the synthesized biodiesel a single run of two-stage transesterification was performed. For the esterification process, oil was treated with 1% sulfuric acid. 10:1 Methanol to oil and 1 wt.% acid mixture were taken in a flat-bottomed flask and kept in a water bath. The neck of the flask was connected to a condenser. The whole set-up was placed on a hot plate with magnetic stirrer. After thirty minutes of stirring, 0.5 wt % of KOH (homogeneous base catalyst) was added. The operating conditions were 65°C, 400 rpm stirring speed and 5 hours of process time [17]. After the reaction, the mixture was brought to room temperature and was allowed to settle for few hours. Two distinct layers were observed. The biodiesel formed at the top layer was separated and washed with distilled water.

## RESULTS AND DISCUSSION

### Comparison of pretreatment methods on oil yield

Pretreatment of *Vernonia cinerea* biomass was done using ultrasonication, microwave assistance and autoclave methods. The highest oil yield was

observed in ultrasonication-pretreated biomass. Without pretreatment the oil extraction yield was observed as 34.55 wt %. The yield significantly increased in all three pretreatment processes as observed in Figure 1.



**Fig. 1.** Oil yield obtained using the different pretreatment methodologies.

Ultrasonication pretreatment process has given a maximum increase of 6.35% oil yield. Earlier, the increase in oil yield was reported as 4.6% with the same pretreatment process [12]. The result obtained in the current work is appreciably high.

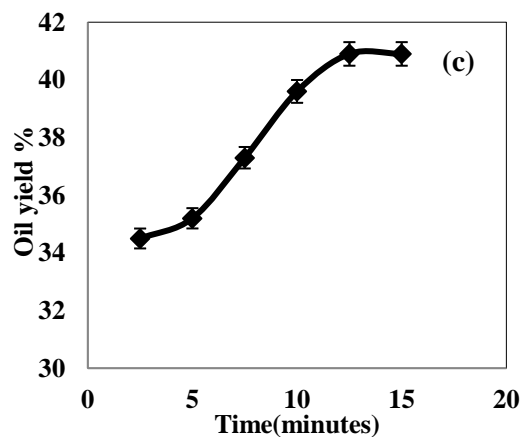
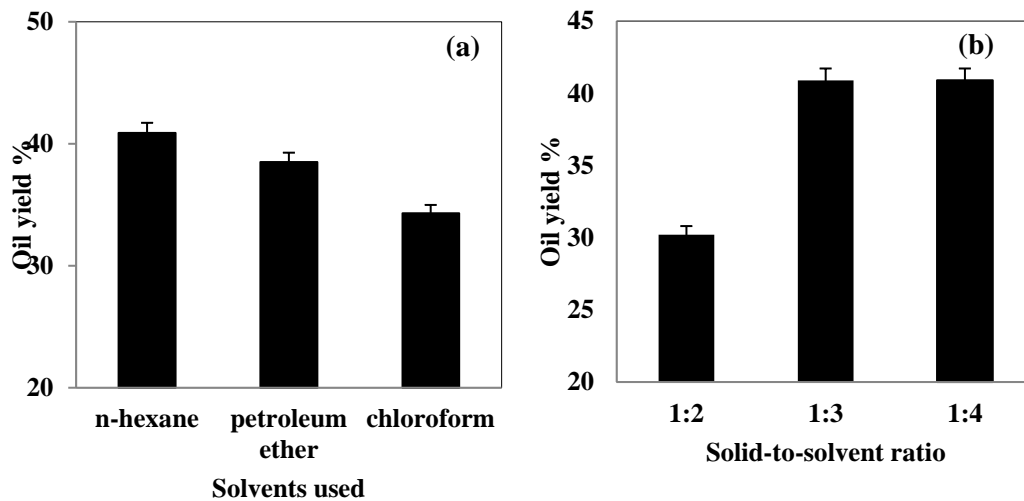
Hence, the oil extraction was performed with optimization of other important parameters to obtain high yield.

*Optimization of process parameters for oil extraction using ultrasonication*

The yield of oil with ultrasonication pretreatment gave the highest yield, thereby optimization of solvent, solid-to-solvent ratio and time was performed.

*Influence of solvents used for ultrasonication*

n-Hexane, petroleum ether and chloroform were the solvents chosen for ultrasonication. Solid-to-solvent ratio was taken as 1:3 and ultrasonication time was 10 minutes.



**Fig. 2.** Optimization of ultrasonication pretreatment process: (a) influence of solid-to-solvent (n-hexane) ratio; (b) effect of different solvents used; (c) effect of ultrasonication time.



The best yield was obtained using n-hexane solvent (Figure 2a). Many earlier works on extraction of oil have proved n-hexane as the best solvent for the maximum yield of oil from non-edible seeds [17].

#### *Solvent-to-solid ratio in ultrasonication*

Different ratios of 1:2, 1:3, 1:4 n-hexane-to-seed were taken and subjected to ultrasonication pretreatment. The process was carried out at room temperature for 12.5 minutes (Figure 2b).

#### *Ultrasonication pretreatment time*

Time of ultrasonication pretreatment was optimized with n-hexane as the solvent. The solvent-to-solid ratio was 1:3. Time was varied from 2.5 minutes till 15 minutes. The maximum yield of oil was observed at 12.5 minutes (Figure 2c).

#### *Extraction of oil following ultrasonication pretreatment*

*Influence of solvents used for extraction.* After ultrasonication pretreatment, few solvents, polar and non-polar in nature, namely acetone, chloroform, dichloromethane, petroleum ether, methanol and n-hexane were chosen for extraction of oil (Table 1). The yield of oil with methanol as solvent was the lowest with 20.3%. Non-polar solvents as listed in the table below yielded high oil extraction. The maximum yield was observed using n-hexane as the solvent. For extraction of oil, non-polar solvents are better suited than polar solvents as more of free fatty acids would be extracted using polar solvents [18].

The graph evidently shows that as the polarity of the solvent increases the extraction yield decreases. The maximum yield was observed to be 40.9% with the non-polar solvent n hexane (Figure 3a).

*Influence of moisture content in seeds.* Moisture content in seeds is a very important parameter for oil extraction. Presence of water would be an impeding factor for oil extraction with hydrocarbons. The moisture content on dry basis was read by the AOAC method [19]. Four samples beginning with the moisture content of 7% reduced till 2% were taken. Maximum oil extraction of 40.9% was observed with 2% moisture content. The extraction of oil got improved by 9.85% when the moisture content in the seeds was brought to the minimal one (Figure 3b). The seeds were dried for the removal of moisture content. By the process of drying the seed membrane wall the hydrolyzing enzymes get stimulated which leads to denaturalization of the protein structure inside the seed membrane. This helps in extraction of more oil from the dried powdered seeds [20]. Oil

extraction was highest at the minimum moisture content in earlier works too [21-23].

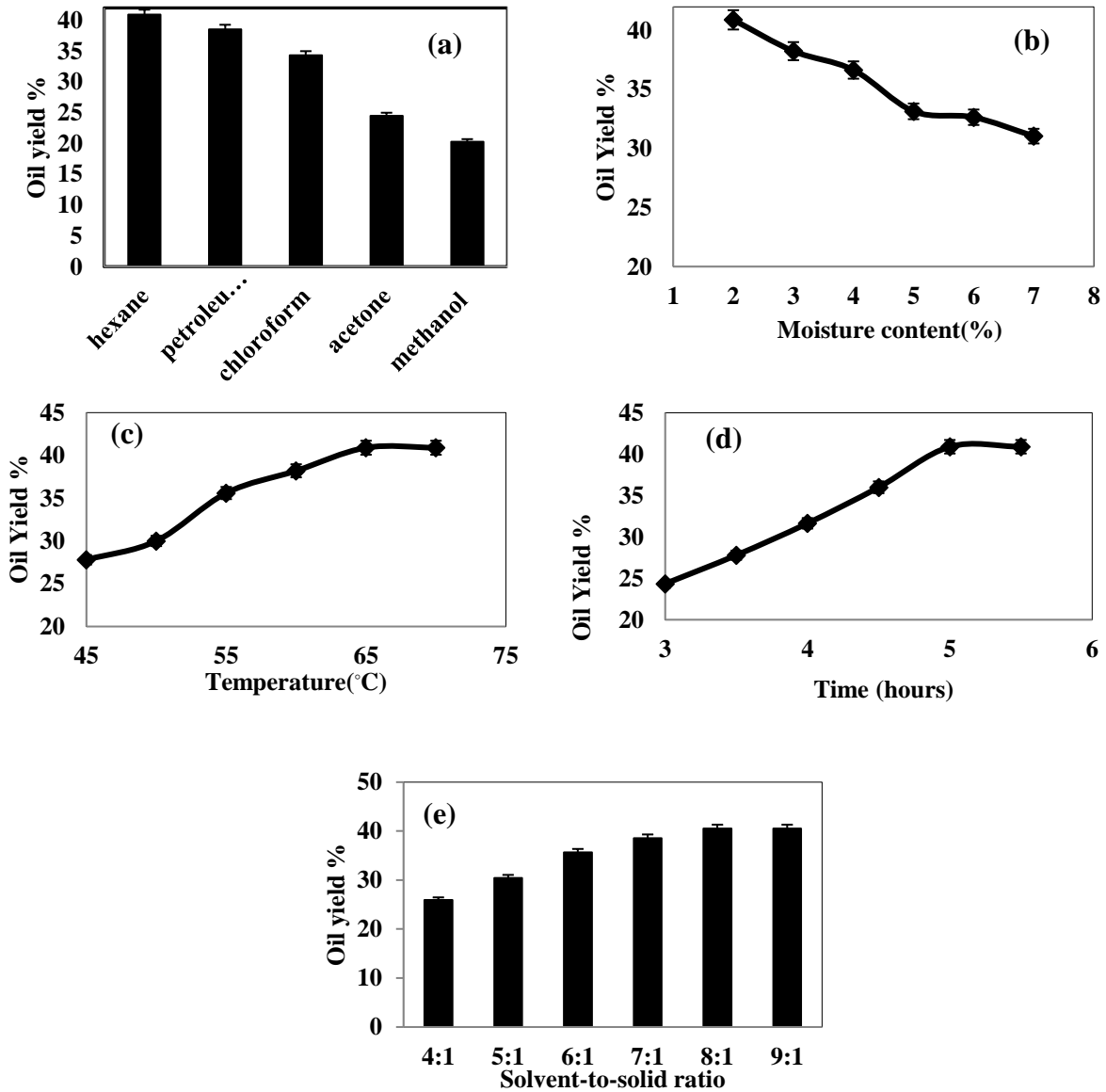
*Influence of particle size of the powdered seeds.* The powdered seeds with moisture content of 2% were subjected to mechanical screening where the powder was discriminated into different fractions as per their cumulative size. Particles retained above the mesh 20, 40, 80, 100, 120, 200 were taken for analysis (Table 2). The oil extraction of 40.9% was observed to be the highest at the particle size range of 200 mesh. Lesser the particle size better is the observed oil yield. The wall of the seeds gets broken with the process of milling. While milling the seeds into finer particles, heat gets produced which is thereby making the cell walls of the seeds easily broken. Due to this phenomenon extraction of oil gets influenced by the reduction in particle size [24].

*Influence of temperature.* Temperature is one important parameter to be optimized. Extraction was performed in the temperature range of 45-70 °C using n-hexane as solvent for 5 hours. The optimized parameters of powder taken as the feed were moisture content of 2% and particle size of 200 mesh. Oil yield improved and was noted to be high at 65°C and maintained to be the same at next increment of 70°C too (Figure 3c). Thus, the maximum yield is obtained at boiling range of n-hexane solvent. Many previous works have observed the highest oil yield only around the boiling range of the solvent. When the temperature reaches the boiling point of the solvent, an unparalleled improvement of diffusion coefficient between the solvent and the oil can be observed thereby improving the extraction of oil [25, 26]

*Influence of extraction time.* The main parameters to evaluate the economy of the extraction process are extraction time and amount of solvent utilized for oil extraction. Extraction of oil was performed from 3 hours till 5 hours 30 min (6-9 cycles per hour). The oil yield was calculated for every 30 min. It was found to be maximum at 5 hours of extraction time. After five hours there was no huge incremental yield of oil observed (Figure 3d). So, the optimized extraction could be concluded as 5 hours since extending the extraction beyond that time frame would mean spending high energy thereby increasing the cost of extraction. The inclusion of ultrasonication pretreatment process made the entire process time-effective as the Soxhlet extraction without pretreatment was extended up to 7 hours whereas the pretreatment made the entire extraction process in 5 hours. The reduction of time by two hours may be due to expeditious mass transfer of oil from the seeds to the solvent [27].

**Table 1.** List of solvents used for oil extraction with their properties

Name of the solvent	Chemical formula	Molecular weight (g/mol)	Density (kg/m <sup>3</sup> )	Boiling point (°C)	Polarity index	Polarity
n-hexane	C <sub>6</sub> H <sub>14</sub>	86.17	655	69	0.1	Non polar
Petroleum ether	C <sub>6</sub> H <sub>14</sub>	86.18	640	60-80	0.1	Non polar
Chloroform	CHCl <sub>3</sub>	119.38	1490	61.2	4.1	Non polar
Acetone	C <sub>3</sub> H <sub>6</sub> O	58.08	784	56	5.1	Polar
Methanol	CH <sub>3</sub> OH	32.04	792	65	5.1	Polar



**Fig. 3.** (a) Influence of different organic solvents used for oil extraction (process conditions: solvent-to-solid 9:1, 65°C, 5.5 h, 2% moisture); (b) Influence of moisture content in powdered seeds (process conditions: n-hexane solvent 9:1, 65°C, 5.5 h); (c) Influence of extraction temperature (process conditions: n-hexane solvent 9:1, 2% moisture, 5.5 h); (d) Influence of extraction time (process conditions: n-hexane solvent 9:1, 2% moisture, 65°C); (e) Influence of solvent-to-solid ratio (process conditions: n-hexane solvent, 2% moisture, 65°C, 5 h), 200 mesh particle size of powdered seeds in all cases.

**Influence of solvent-to-solid ratio.** All the above-mentioned parameters were taken at their optimized values to study the effect of solvent-to-solid ratio. Powdered seeds of particle size of 200 mesh with 2 % moisture content were subjected to extraction at the temperature of 65°C. The extraction process continued for 5 hours. Different solvent-to-solid ratios of n-hexane solvent, i.e. 2:1 incremented till 9:1 were taken and the significance of this parameter was studied. The observed highest yield at 8:1 ratio was 40.9 % (Figure 3e). At higher solvent-to-solid ratio extraction yield was observed to be high. This could be due to the immense driving force resulting in high oozing out of oil in more diluted solvent system [28]

*Kinetic studies on oil extraction*

The rate equation for extraction of oil can be expressed as equation (3):

$$\frac{dY}{dt} = kY^n \tag{3}$$

From the yield (Y) of oil and the extraction time (t), the rate constant (k) and the order of the reaction (n) can be found.

At different temperatures, namely 50, 55, 60 and 65°C the yield of oil was experimentally determined for the kinetic studies. The values of the respective yield are tabulated in Table 3.

A plot of ln(dY/dt) versus lnY is drawn and the values of the rate constant are obtained from the slopes of the plot (Fig 4 a). Regression coefficient (R<sup>2</sup>) average was obtained as 0.956. From the ‘n’ values, we could conclude it to be first-order kinetics.

Parthiban and Perumalswamy [1] have also reported first-order kinetics for oil extraction from *Annona squamosa* seeds.

Using Arrhenius equation, the rate constants can be found from equation (4) and are listed in Table 4 obtained at the different temperatures:

$$k = Ae^{-\frac{Ea}{RT}} \tag{4}$$

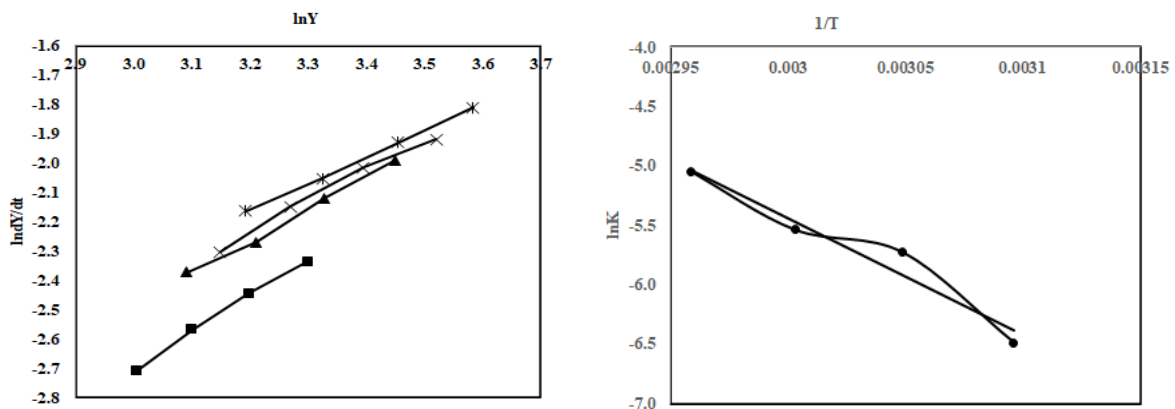
**Table 3.** Oil yield in the temperature range of 50-65°C with respect to extraction time

Time, hours	Temperature, °C			
	50	55	60	65
3.0	20.2	22	23.3	24.35
3.5	22.2	24.8	26.3	27.8
4.0	24.5	27.9	29.8	31.65
4.5	27.1	31.5	33.8	36
5.0	30	35.6	38.2	40.9

**Table 4.** Values of reaction rate constants with respect to temperature

Temperature (°C)	Rate constant k (min <sup>-1</sup> )
50	1.521 × 10 <sup>-3</sup>
55	3.251 × 10 <sup>-3</sup>
60	3.934 × 10 <sup>-3</sup>
65	6.44 × 10 <sup>-3</sup>

From the slope of the line in Fig. 4b, the activation energy was found to be 82.2 kJ/mol.



**Fig. 4.** (a) Plot of ln dY/dt vs lnY at 50, 55, 60, 65°C for *Vernonia cinerea* oil; (b) Graph of lnk vs 1/T for the determination of activation energy.

*Physical and chemical properties of extracted oil*

The basic physical properties of extracted *Vernonia cinerea* oil were determined using a standard method and are listed in Table 5.

Three important properties of the oil which determine whether the oil can be further subjected to transesterification process for the production of biodiesel are iodine value (IV), saponification value (SV) and cetane number (CN). These properties were determined for *Vernonia cinerea* oil.

Iodine value defines the degree of unsaturation. When the presence of unsaturated molecules is high, the FAME produced will not be suitable to be used as fuel. These double-bond molecules will react with the atmospheric oxygen leading to the formation of peroxide. Crosslinking may occur which further may lead to polymerization into a gummy material. On ignition at high temperature, this gummy polymer can clog the engine. The iodine value must be less than 133.5 [30].

**Table 5.** Properties of *Vernonia cinerea* oil

Property	Obtained value
Color	Dark brown
Odor	Repulsive
Specific gravity at 25°C (ASTM D1840 method)	0.927
Kinematic viscosity (cst) (ASTM D445 method)	41.1
Acid value (ASTM D664 method))	10.2
Iodine value	68.5
Saponification value	205.2
Cetane number	57.51
Long chain saturation factor (LCSF)	15.3
Higher heating value (HHV)	39.997

Cetane number tells about how rapid the fuel ignition occurs. The cetane number as per ASTM should be above 47 and should not exceed 65. The upper limit is fixed, as the increase in cetane number would decrease the iodine value which again would lead to gumming of fuel [30].

*Transesterification of Vernonia cinerea oil*

The acid value of extracted oil was high thereby before transesterification process, esterification process was carried out. The yield of biodiesel with the process conditions of 10:1 methanol-to-oil ratio and 0.5 wt % KOH was 89%. With proper

optimization of process parameters, the conversion of oil could be improved.

CONCLUSION

*Vernonia cinerea* seeds were subjected to pretreatment using ultrasound, microwave and autoclave techniques. Ultrasonication pretreatment was highly effective resulting in comparatively higher yield of oil. Oil extraction was performed by the Soxhlet method for oil extraction and the parameters for high yield were optimized. n-Hexane, a non-polar solvent, was best suited for extraction of oil. The parameters like moisture content, particle size, time, temperature and solid-to-solvent ratio were optimized. The highest yield of oil with all the optimized parameters is 40.9 %. The chemical parameters are well within the ASTM standard limits. A trial run was performed to check the conversion of oil and the yield of biodiesel was 89%. Further optimization of process conditions would enhance the yield of biodiesel. Thereby, *Vernonia cinerea* could be the best second-generation (non-edible oil) feedstock to produce biodiesel.

REFERENCES

1. K. S. Parthiban, M. Perumalsamy, *Fuel*, **180**, 211 (2016).
2. T. Balamurugan, A. Arun, G. Sathishkumar, *Renewable and Sustainable Energy Reviews*, **94**, 772 (2018).
3. A. H. Demirbas, I. Demirbas, *Energy Convers. Manag.*, **48**, 2386 (2007).
4. M. Balat, *Energy Convers. Manag.*, **52**, 1479 (2011).
5. S. Asif, M. Ahmad, M. Zafar, N. Ali, *Renewable and Sustainable Energy Reviews*, **74**, 687 (2017).
6. M. M. Azam, A. Waris, N. M. Nahar, *Biomass and Bioenergy*, **29**, 293 (2005).
7. H. H. Mardhiah, H. C. Ong, H. H. Masjuki, S. Lim, H. V. Lee, *Renewable and Sustainable Energy Reviews*, **67**, 1225 (2017).
8. B. Reyes-Trejo, D. Guerra-Ramírez, H. Cuevas-Sánchez, J. A. Reyes, L. Reyes-Humacero, J. A. Rodríguez-Salazar, *Industrial Crops and Products*, **52**, 400 (2014).
9. K. V. Thiruvengadaravi, J. Nandagopal, P. Baskaralingam, V. Sathya Selva Bala, S. Sivanesan, *Fuel*, **98**, 1 (2012).
10. J. Y. Lee, C. Yoo, S. Y. Jun, C. Y. Ahn, H. M. Oh, *Bioresource Technology*, **101**, 75 (2010).
11. Z. Li, F. Yang, L. Yang, Y. Zu, *Journal of Chemistry*, **16**, 1 (2016).
12. V. Theresa, R. S. Ernest Ravindran, R. Ajith Kumar, K. Pandian, S. Renganathan, *Energy Sources, Part A: Recovery, Utilization, and Environmental Effects*, **39**, 1369 (2017).
13. H. Mohammadpour, S. M. Sadrameli, F. Eslami, A. Asoodeh, *Industrial Crops and Products*, **131**, 106 (2019).

14. E. Momeny, S. Rahmati, N. Ramli, *J. Food Process/ Technol.*, **3**, 7 (2012).
15. R. Halim, R. Harun, M. K. Danquah, P. A. Webley, *Appl. Energy*, **91**, 116 (2012)
16. P. Sivakumar, K. S. Parthiban, P. Sivakumar, M. Vinoba, S. Renganathan, *Industrial & Engineering Chemistry Research*, **51**, 8992 (2012).
17. A. S. Bharadwaj, S. Niju, K. M. Meera Sheriffa Begum, A. Narayanan, *Environmental Progress & Sustainable Energy*, **39**(3), (2020).
18. T. Suganya, R. Kasirajan, S. Renganathan, *Bioresource Technology*, **156**, 283 (2014).
19. I. Efthymiopoulos, P. Hellier, N. Ladommatos, A. Russo-Profili, A. Eveleigh, A. Aliev, A. Kay, B. Mills-Lampton, *Industrial Crops and Products*, **119**, 49 (2018).
20. M. Fadhlullaha, S. Nanan, B. Widiyanto, E. Restiawaty, *Energy Procedia*, **68**, 177 (2015).
21. S. Hathurusingha, CQ University Rockhampton, Australia, 2012.
22. B. A. Orhevba, O. Chukwu, Z. E. Osunde, V. Ogwuagwu, *Global Journal of Engineering Design & Technology*, **2**, 20 (2013).
23. N. Mabona, W. Aboyade, M. Mollagee, L. Mguni, *Energy Sources, Part A: Recovery, Utilization, and Environmental Effects*, **40**, 501 (2018).
24. M. Karthikeyan, S. Renganathan, *Energy Sources, Part A: Recovery, Utilization and Environmental Effects*, **39**, 1140 (2017).
25. S. F. Bailey's Industrial Oil and Fat Products, John Wiley & Sons Inc., New Jersey, 2005.
26. R. Mathiarasi, N. Partha, *Renewable Energy*, **96**, 583 (2016).
27. S. Almasi, B. Ghobadian, G. Najafi, M. D. Soufi, *Journal of Cleaner Production*, 125830 (2021)
28. T. Suganya, S. Renganathan, *Bioresource Technology*, **107**, 319 (2012).
29. V. Ávila Vázquez, R. A. Díaz Estrada, M. M. Aguilera Flores, C. Escamilla Alvarado, H. C. Correa Aguado, *Biofuels*, **11**(7), (2020).
30. L. Wang, H. Yu, X. He, R. Liu, *Journal of Fuel Chemistry and Technology*, **40**, 397 (2012).

# MHD Eyring-Powell nanofluid flow in a channel with oscillatory pressure gradient: A note

P. B. Kumar, S. Srinivas\*

Department of Mathematics, VIT-AP University, Inavolu – 522 237, Near Vijayawada, Andhra Pradesh, India.

Received: November 01, 2021; Revised: March 03, 2022

This article describes the MHD Eyring-Powell nanofluid flow with oscillatory pressure gradient in an impermeable vertical channel. Here, blood and various shapes of alumina ( $Al_2O_3$ ) are taken as non-Newtonian base-fluid and nanoparticles, respectively. Maxwell Garnett and Brinkman models are used to calculate the thermophysical properties of the nanofluid. Governing flow equations are simplified and the resulting system of non-linear differential equations is solved by Shooting technique along with the Runge-Kutta fourth-order method. The effects of arising parameters on the flow variables have been studied in detail and numerical results are depicted graphically. Numerical results for the Nusselt number are presented in tabular form for different shapes of nanoparticles.

**Keywords:** Eyring-Powell nanofluid, Pulsating flow, Hartmann number, Grashof number.

## INTRODUCTION

Nanoparticles are used as drug delivery carriers which are usually less than 100 nm and contain various biodegradable elements such as natural/synthetic polymers/metals [1]. Choi and Eastman [2] noticed that the nanofluids enhance the thermal conductivity, as well as the heat transfer in base fluids. Since then, studies pertaining to nanofluids have attracted the attention of many researchers (see [3-8]) due to the rapid development of nanotechnology in engineering and sciences.

Oscillatory flow is a periodic flow oscillating around a non-zero mean value. In recent times, the studies pertaining to pulsating flows gain a great deal of research attention because of their applications in biological areas such as human circulatory, respiratory and vascular systems and in engineering areas such as fuel injection into or exhaust from internal combustion engines, thermo-acoustic coolers and MEMS microfluidic engineering applications [9-12]. Abou-zeid *et al.* [13] examined the heat and mass transfer of a pulsating flow of a non-Newtonian fluid through permeable parallel plates saturated with porous medium. Recently, Jafarzadeh *et al.* [14] simulated the unsteady pulsatile blood flow distribution of nanoparticles loaded with the drug in the artery by taking blood as non-Newtonian in character. Very recently, Kumar and Srinivas [15] numerically studied the combined effects of slip-velocity and Joule's heating on the MHD pulsating flow of Eyring-Powell nanofluid through a vertical porous channel.

Several mathematical models have been

developed to understand the flow behaviour pertaining to the oscillatory flows in different flow configurations (see Refs. [16-21] and several references therein).

A study related to MHD oscillatory flow of an Eyring-Powell nanofluid through the vertical channel considering the shape factor has not yet been reported, to the best of authors' knowledge. So, the main aim of the present study is to examine the flow of an Eyring-Powell nanofluid with oscillating pressure gradient accounting for the magnetic field, Joule's heating and thermal radiation. In this investigation, blood is taken as the base fluid and  $Al_2O_3$  is considered as nanoparticle. Effects of important parameters on the momentum and heat transfer characteristics were analysed with the help of computer illustrations. Results for the rate of heat transfer are presented for four different shapes of nanoparticles. This paper is organised as follows: mathematical formulation, results along with discussion and conclusions.

## MATHEMATICAL FORMULATION

As shown in Fig. 1, the flow of the fluid is only in the  $x$ -direction, and we have taken the oscillatory flow of the Eyring-Powell fluid in the vertical channel. The fluid is electrically conducting due to the applied magnetic field  $B_0$ . The polarization is negligible because of lower magnitude of external magnetic field, hence there will be no internal electric field. The temperature on the left wall of the channel is  $T_0$  while the uniform temperature  $T_1$  is considered on the right wall. The impact of thermal radiation in the equation of energy, is taken into

\* To whom all correspondence should be sent:  
E-mail: srinusuripeddi@hotmail.com

account. The momentum and energy equations considering the Boussinesq approximation for the flow are [15, 19, 22]:

$$\frac{\partial \hat{u}}{\partial \hat{t}} = -\frac{1}{\rho_{nf}} \frac{\partial \hat{p}}{\partial \hat{x}} + \frac{\mu_{nf}}{\rho_{nf}} \left( 1 + \frac{1}{\gamma C \mu_{nf}} \right) \frac{\partial^2 \hat{u}}{\partial \hat{y}^2} + g \beta_{nf} (\hat{T} - T_0) - \frac{\sigma_{nf} B_0^2}{\rho_{nf}} \hat{u} \quad (1)$$

$$\begin{aligned} \frac{\partial \hat{T}}{\partial \hat{t}} = & \frac{\kappa_{nf}}{(\rho c_p)_{nf}} \frac{\partial^2 \hat{T}}{\partial \hat{y}^2} + \frac{\mu_{nf}}{(\rho c_p)_{nf}} \left( 1 + \frac{1}{\gamma C \mu_{nf}} \right) \left( \frac{\partial \hat{u}}{\partial \hat{y}} \right)^2 + \frac{Q_0}{(\rho c_p)_{nf}} (\hat{T} - T_0) \\ & + \frac{\sigma_{nf}}{(\rho c_p)_{nf}} B_0^2 \hat{u}^2 - \frac{1}{(\rho c_p)_{nf}} \frac{\partial q_r}{\partial \hat{y}} \end{aligned} \quad (2)$$

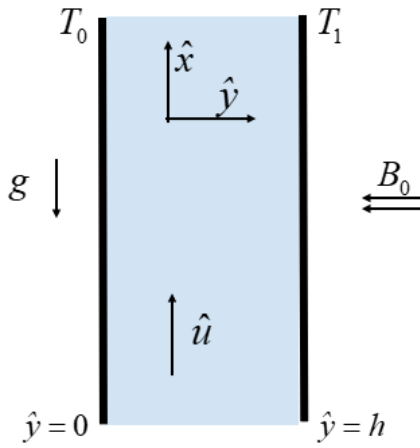


Figure 1. Physical sketch of the flow.

The velocity and temperature fields are subjected to the following conditions:

$$\text{on left wall: } \hat{u} = 0 \text{ and } \hat{T} = T_0; \text{ on right wall: } \hat{u} = 0 \text{ and } \hat{T} = T_1. \quad (3)$$

Flow of the fluid in the channel is influenced by an oscillatory pressure gradient [18]:

$$-\frac{1}{\rho_f} \frac{\partial \hat{p}}{\partial \hat{x}} = A \left[ 1 + \varepsilon e^{i\omega t} \right]; \quad \varepsilon \ll 1 \quad (4)$$

where, the subscript  $f$  indicates the base fluid;  $nf$  indicates the nanofluid;  $\hat{\cdot}$  indicates the dimensional variable;  $\mu_{nf}$  the dynamic viscosity;  $A\rho_f$ , amplitude of the oscillating pressure gradient;  $\gamma$  and  $C$  are the Eyring-Powell fluid parameters;  $\hat{u}$ ,  $\hat{v}$  are the components of velocity along  $x$ ,  $y$  axes;  $\hat{p}$ , the dimensional pressure;  $\rho_{nf}$ , the density;  $g$ , the gravitational force;  $\beta_{nf}$  denotes the thermal expansion coefficient;  $\hat{T}$  represents the dimensional

temperature of the fluid;  $\sigma_{nf}$  the electrical conductivity;  $B_0$ , the magnetic field strength;  $\hat{t}$ , the dimensional time;  $\kappa_{nf}$ , the thermal conductivity;  $(\rho c_p)_{nf}$ , the specific heat and  $Q_0$  indicates the heat source (or sink).

The radiative heat flux,  $q_r$ , is simplified according to the Rosseland approximation as:

$$q_r = \frac{-4}{3} \left( \frac{\partial \hat{T}^4}{\partial \hat{y}} \right) \frac{\hat{\sigma}}{\hat{k}} \quad (5)$$

where,  $\hat{\sigma}$  represents the Stefan-Boltzmann constant, the coefficient of Rosseland mean absorption represented by  $\hat{k}$  and  $\hat{T}^4 \cong 4T_1^3 \hat{T} - 3T_1^4$  [15].

Presenting the non-dimensional variables to transform the flow equations (1) - (5) into the non-dimensional form [7, 23]:

$$u = \hat{u}\omega / A; p = \hat{p} / A\rho_f h; t = \hat{t}\omega; \theta = (\hat{T} - T_0) / (T_1 - T_0); x = \hat{x} / h; y = \hat{y} / h \quad (6)$$

where,  $\omega$  is the angular frequency,  $u$  is the velocity and  $\theta$  is the temperature in dimensionless form.

The nanofluid's physical characteristics are represented as [3, 15, 22, 24]:

$$\left. \begin{aligned} A_1 &= \frac{1}{(1-\phi)^{2.5}} = \frac{\mu_{nf}}{\mu_f}; & A_2 &= (1-\phi) + \phi \left( \frac{\rho_n}{\rho_f} \right) = \frac{\rho_{nf}}{\rho_f}; \\ A_3 &= (1-\phi) + \phi \left( \frac{(\rho c_p)_n}{(\rho c_p)_f} \right) = \frac{(\rho c_p)_{nf}}{(\rho c_p)_f}; \\ A_4 &= \frac{\kappa_n + (m-1)\kappa_f - (m-1)\phi(\kappa_f - \kappa_n)}{\kappa_n + (m-1)\kappa_f + \phi(\kappa_f - \kappa_n)} = \frac{\kappa_{nf}}{\kappa_f}; \\ A_5 &= 1 + \frac{3((\sigma_n / \sigma_f) - 1)\phi}{((\sigma_n / \sigma_f) + 2) - ((\sigma_n / \sigma_f) - 1)\phi} = \frac{\sigma_{nf}}{\sigma_f}; \\ A_6 &= (1-\phi) + \phi \left( \frac{(\rho\beta)_n}{(\rho\beta)_f} \right) = \frac{(\rho\beta)_{nf}}{(\rho\beta)_f} \end{aligned} \right\} \quad (7)$$

where,  $\phi$  is the nanoparticle volume fraction,  $m$  is the shape factor, the subscript  $n$  is the nanoparticle.

Transforming the Eqs. (1) - (2) by using Eqs. (5) - (7) we get:

$$-\frac{\partial p}{\partial x} = 1 + \varepsilon e^{it} \quad (8)$$

$$H^2 \frac{\partial u}{\partial t} = -\frac{H^2}{A_2} \frac{\partial p}{\partial x} + \left(\frac{A_4}{A_2}\right) \left(1 + \frac{k_1}{A_1}\right) \frac{\partial^2 u}{\partial y^2} + \left(\frac{A_6}{A_2}\right) (Gr) \theta - \left(\frac{A_5}{A_2}\right) M^2 u \quad (9)$$

$$H^2 \frac{\partial \theta}{\partial t} = \left(\frac{A_4}{A_3} \frac{1}{Pr} + \frac{4}{3A_3} \frac{Rd}{Pr}\right) \frac{\partial^2 \theta}{\partial y^2} + \left(\frac{A_4}{A_3}\right) \left(1 + \frac{k_1}{A_1}\right) Ec \left(\frac{\partial u}{\partial y}\right)^2 + \left(\frac{A_5}{A_3}\right) Ec (M^2) u^2 + \left(\frac{Q}{A_3}\right) \theta \quad (10)$$

The transformed conditions are as follows:

$$\text{at } y = 0 : u = 0 \text{ and } \theta = 0; \quad \text{at } y = 1 : u = 0 \text{ and } \theta = 1 \quad (11)$$

where,  $H = h\sqrt{\omega/\nu_f}$  (frequency parameter),

$Pr = \nu_f (\rho c_p)_f / \kappa_f$  (Prandtl number),

$M = B_0 h \sqrt{\sigma_f / \mu_f}$  (Hartmann number),

$Q = Q_0 h^2 / [\nu_f (\rho c_p)_f]$  (heat source/sink parameter),

$Ec = A^2 / [\omega^2 (c_p)_f (T_1 - T_0)]$  (Eckert number),

$k_1 = 1 / (\gamma C \mu_f)$  (non-Newtonian parameter),

$Gr = g \beta_f (T_1 - T_0) \omega h^2 / (A \nu_f)$  (Grashof number),

$\nu_f = \mu_f / \rho_f$  (kinematic viscosity) and

$Rd = (4\sigma T_1^3) / (\kappa \hat{k})$  (radiation parameter).

A perturbative solution has been assumed to derive the solution for the transformed equations in the form [22, 25]:

$$u(y, t) = u_0(y) + \varepsilon u_1(y) e^{it}; \quad \theta(y, t) = \theta_0(y) + \varepsilon \theta_1(y) e^{it} \quad (12)$$

Here,  $u_0$  and  $\theta_0$  are the zeroth-order terms;  $u_1$  and  $\theta_1$  are first-order terms of the perturbative solution of the velocity and temperature distributions, respectively.

Incorporating Eq. (12) in Eqs. (8) – (11) and on equating the coefficients of different powers of  $\varepsilon$  we get:

$$B_1 u_0'' + B_3 u_0 + B_2 \theta_0 + B_4 = 0 \quad (13)$$

$$B_1 u_1'' + B_5 u_1 + B_2 \theta_1 + B_4 = 0 \quad (14)$$

$$B_6 \theta_0'' + B_7 (u_0')^2 + B_8 (u_0)^2 + B_{10} \theta_0 = 0 \quad (15)$$

$$B_6 \theta_1'' + (B_9 + B_{10}) \theta_1 + 2B_7 (u_0' u_1') + 2B_8 (u_0 u_1) = 0 \quad (16)$$

The above coupled equations are subjected to the conditions:

$$\begin{aligned} \text{at } y = 0 : u_0 = 0, u_1 = 0, \theta_0 = 0 \text{ and } \theta_1 = 0 \\ \text{at } y = 1 : u_0 = 0, u_1 = 0, \theta_0 = 1 \text{ and } \theta_1 = 0. \end{aligned} \quad (17)$$

Here,  $B_1 = (A_1/A_2)(1 + (k_1/A_1))$ ;  $B_2 = (A_6/A_2)Gr$ ;  $B_3 = -(A_5/A_2)M^2$ ;  $B_4 = H^2/A_2$ ;  $B_5 = B_3 - iH^2$ ;  $B_6 = (1/Pr)((A_4/A_3) + ((4Rd)/(3A_3)))$ ;  $B_7 = (B_1 A_2/A_3)(Ec)$ ;  $B_8 = (A_5/A_3)(Ec)(M^2)$ ;  $B_9 = B_5 - B_3$ ;  $B_{10} = Q/A_3$ .

The coupled equations from (13) to (16) are solved along with the conditions given in Eq. (17), numerically.

## RESULTS AND DISCUSSION

By assigning the numerical values to various parameters, for the physical insight of the problem, velocity ( $u$ ), temperature ( $\theta$ ) and Nusselt number ( $Nu$ ) distributions, for blood –  $Al_2O_3$  were discussed. The obtained results of the investigation are depicted graphically and in tabular form. While performing the simulations against one parameter, the values of other parameters are taken as follows:  $t = \pi/4$ ;  $\varepsilon = 0.01$ ;  $k_1 = 3$ ;  $\phi = 0.05$ ;  $Q = 1$ ;  $Pr = 21$ ;  $Ec = 1$ ;  $Gr = 4$ ;  $M = 2$ ;  $Rd = 2$ ;  $m = 3$  and  $H = 2$ . Also, the thermophysical properties of blood and  $Al_2O_3$  are  $\rho_f = 1050$ ,  $\rho_n = 3970$ ,  $(c_p)_f = 3617$ ,  $(c_p)_n = 765$ ,  $\kappa_f = 0.52$ ,  $\kappa_n = 40$ ,  $\sigma_f = 0.8$ ,  $\sigma_n = 1 \times 10^{-10}$ ,  $\beta_f = 1.8 \times 10^{-6}$ ,  $\beta_n = 8.5 \times 10^{-6}$  [22, 26].

In order to validate the present numerical work, the results were compared with those reported by Kumar and Srinivas [22] by considering  $Gr = R = Ec = 0$ . This comparison (see Fig. 2) shows that there is an excellent agreement between present numerical work and previously published results.

The velocity profiles against various parameters are shown in Figure 3. Fig. 3(a) illustrates the effect of  $H$  on the velocity of the fluid. It reveals that a rise in the frequency parameter enhances the velocity of the fluid. As non-Newtonian parameter,  $k_1$  and the inertial force are related directly; by raising  $k_1$  the inertial forces reduce the fluid velocity as depicted in Fig. 3(b). The influence of Grashof number  $Gr$  on  $u$  is illustrated in Fig. 3(c). The relation between  $Gr$  and the velocity describes that the rise in  $Gr$  decreases the viscosity. This decrease in viscosity aids in the raise of buoyancy forces, and as a consequence, there is a growth in the velocity.

From Fig. 3(d), a fall in the velocity profiles can be noticed with an increase in  $M$ . This decrement is caused due to the Lorentz force which is a resistive force that results in lowering the velocity.



Figures 3(e) and 4(c) demonstrate the effect of varying thermal radiation ( $Rd$ ) on the fluid velocity and temperature within the channel. The figures reveal that both the velocity and temperature within the channel raises with an increment of  $Rd$ . This rise in the temperature distribution maybe because of the decrease in thermal conduction of the fluid, which is causing a rise in the heat flux to the fluid. This change in the heat flux results in the rise of the fluid temperature, which enhances the kinetic energy of the fluid, thereby causing a faster flow of the fluid (Fig. 3(e)).

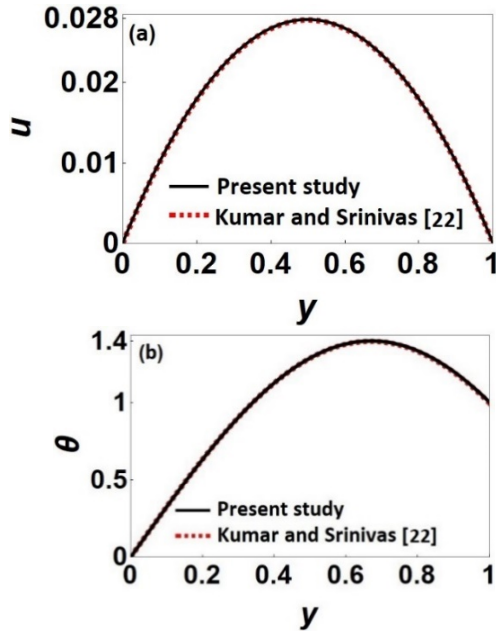


Figure 2. Comparison of (a) Velocity,  $u$  and (b) Temperature,  $\theta$  with the previous work.

Fig. 4(a) depicts the variation of  $Ec$  on the temperature distribution. Because of the viscous dissipation, an increase in the Eckert number generates the internal energy, and it reflects in the enhancement of the fluid temperature. The same can be observed from Fig. 4(a) that raising  $Ec$  enhances the temperature. From Fig. 4(b), it is clear that as increasing heat source cause the higher temperature. Fig. 4(d) is plotted for temperature distribution, to see the effect of  $\phi$ . The addition of nanoparticles into base fluids raises the thermal conductivity. Additional factors such as the size and shape of the particles may also bring changes in the thermal conductivity. Consequently, there is an increase in the temperature distribution as  $\phi$  increases (see Fig. 4(d)).

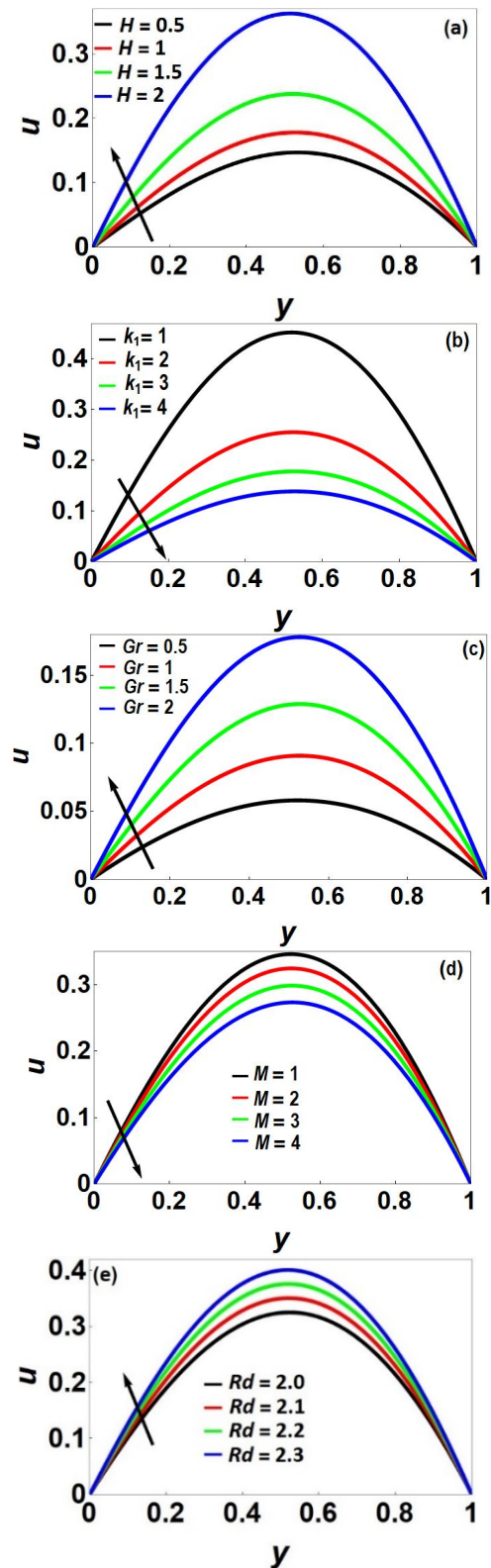
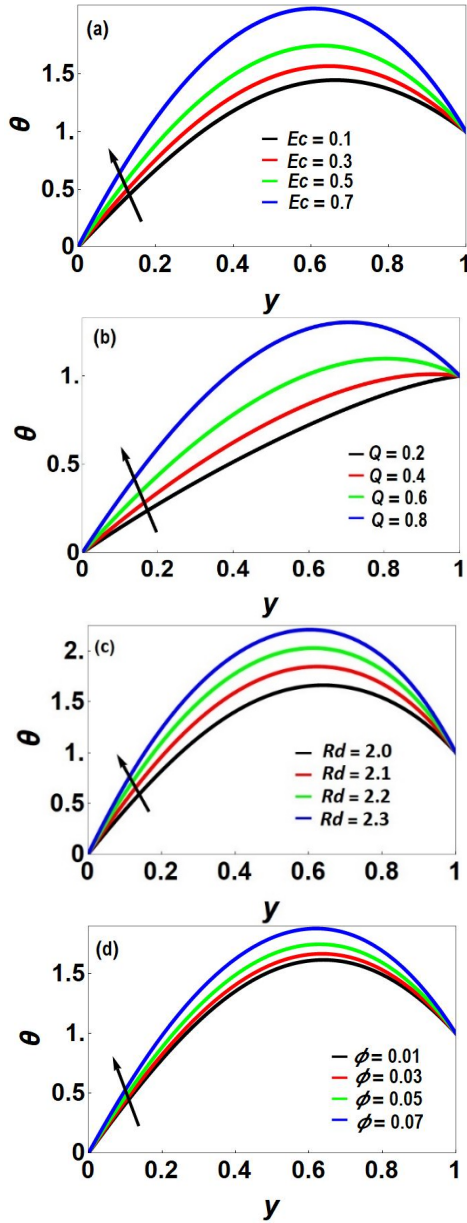


Figure 3. (a) Influence of  $H$ ; (b) Influence of  $k_1$ ; (c) Influence of  $Gr$ ; (d) Influence of  $M$ ; (e) Influence of  $Rd$  on  $u$ .




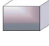
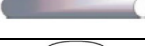

**Figure 4.** (a) Influence of  $Ec$ ; (b) Influence of  $Q$ ; (c) Influence of  $Rd$ ; (d) Influence of  $\phi$  on  $\theta$ .

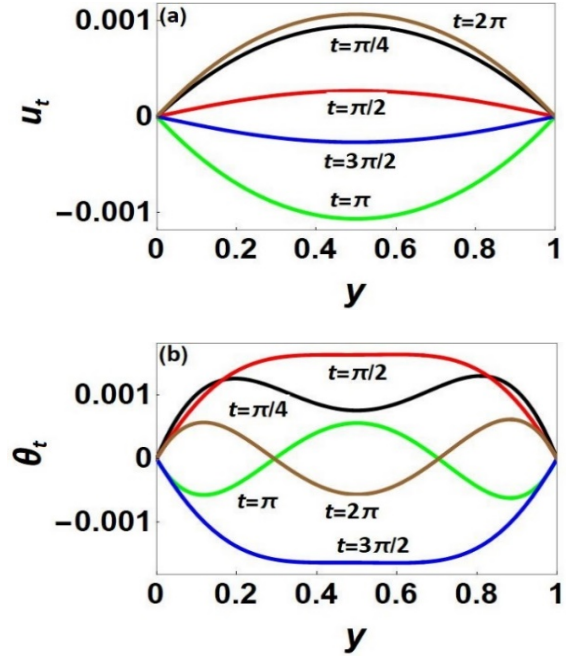
From Fig. 5 it is evident that unsteady velocity and unsteady temperature oscillate with increasing time, because the flow of the fluid is driven by an oscillatory pressure gradient. Consequently,  $u_t$  and  $\theta_t$  significantly vary with time. Fig. 5(b) illustrates that maximum temperature is drifted towards the boundary layers near channel walls.

The values of Nusselt number (on left and right walls) can be determined as follows [18]:

$$Nu_{0,1} = \frac{h\kappa_{nf}}{\kappa_f(T_1 - T_0)} \left( \frac{\partial \hat{T}}{\partial \hat{y}} \right) = A_4 \left( \frac{\partial \theta}{\partial y} \right)_{y=0,1}. \quad (18)$$

**Table 1.** The values of shape factor for various shapes of nanoparticles [6, 27]

Name of the shape	Shape of the nanoparticle	Shape factor ( $m$ )
Spherical		3
Brick		3.7
Cylinder		4.9
Platelet		5.7



**Figure 5.** Influence of  $t$  on (a)  $u_t$  (b)  $\theta_t$ .

Shape factors values for nanoparticles, used in our calculations, are depicted in Table 1. Table 2 shows the computed values of  $Nu$  on channel walls for different parameters. Our calculations reveal that heat transfer rate raises on the left wall,  $y = 0$  while it drops at the right wall of the channel for increasing values of  $Gr, \phi$  and  $Q$ , whereas the Nusselt number decreases with increasing  $k_l, M$  and  $Rd$ . This is because a raise in rheological parameter and Hartmann number reduces the fluid velocity near  $y = 0$ . Furthermore, the heat transfer rate increases as the particle shape factor increases for any given parameter. One can observe that the heat transfer rate is maximum for the case of platelets like cylindrical, brick and spherically shaped nanoparticles.

**Table 2.:** Variation of  $Nu$  for different values of  $Gr$ ,  $k_l$ ,  $M$ ,  $\phi$  and  $Q$ .

Parameter	Value	Shape of Nanoparticle ( $m$ )													
		Spherical ( $m = 3$ )		Brick ( $m = 3.7$ )		Cylinder ( $m = 4.9$ )		Platelets ( $m = 5.7$ )							
		$Nu_{y=0}$	$Nu_{y=1}$	$Nu_{y=0}$	$Nu_{y=1}$	$Nu_{y=0}$	$Nu_{y=1}$	$Nu_{y=0}$	$Nu_{y=1}$						
$Gr$	0.5	3.9808	-2.8623	4.0358	-2.8727	4.1258	-2.8872	4.1830	-2.8946	4.2680	-3.1861	4.3201	-3.1938	4.4040	-3.2088
	1	4.2680	-3.1861	4.3201	-3.1938	4.4040	-3.2088	4.4595	-3.2294	4.5191	-3.2469	4.5740	-3.2646	4.6340	-3.2821
	1.5	4.7590	-3.7369	4.8020	-3.7360	4.8733	-3.7327	4.9191	-3.7294	4.9749	-3.7269	5.0201	-3.7244	5.0651	-3.7219
$k_l$	1	9.7486	-9.1379	10.351	-9.7284	11.431	-10.768	12.1557	-11.466	12.840	-11.812	13.525	-12.466	14.210	-13.120
	2	6.8263	-5.9910	6.7640	-5.8822	6.6890	-5.7293	6.6551	-5.6446	6.6212	-5.5333	6.5974	-5.4888	6.4644	-5.4148
	3	5.6526	-4.7252	5.6651	-4.6933	5.6912	-4.6443	5.7101	-4.6148	5.7294	-4.5868	5.7487	-4.5601	5.7680	-4.5333
$M$	2	5.6526	-4.7252	5.6651	-4.6933	5.6912	-4.6443	5.7101	-4.6148	5.7294	-4.5868	5.7487	-4.5601	5.7680	-4.5333
	3	5.5173	-4.5740	5.5332	-4.5456	5.5491	-4.5172	5.5651	-4.4888	5.5810	-4.4601	5.5974	-4.4312	5.6133	-4.4025
	4	5.3376	-4.3756	5.3537	-4.3472	5.3698	-4.3188	5.3859	-4.2901	5.4020	-4.2612	5.4181	-4.2325	5.4342	-4.2038
$\phi$	0.01	4.3371	-3.4423	4.3470	-3.4440	4.3569	-3.4457	4.3668	-3.4474	4.3767	-3.4491	4.3866	-3.4508	4.3965	-3.4525
	0.03	4.8934	-3.9747	4.9155	-3.9715	4.9376	-3.9683	4.9597	-3.9651	4.9818	-3.9578	4.9999	-3.9546	5.0220	-3.9514
	0.05	5.6526	-4.7252	5.6651	-4.6933	5.6912	-4.6443	5.7101	-4.6148	5.7294	-4.5868	5.7487	-4.5601	5.7680	-4.5333
$Q$	0.4	2.1001	-0.3467	2.1493	-0.3384	2.2295	-0.3234	2.2810	-0.3127	2.3325	-0.2977	2.3840	-0.2828	2.4355	-0.2679
	0.6	2.7223	-1.2193	2.7753	-1.2202	2.8283	-1.2197	2.8813	-1.2180	2.9343	-1.2163	2.9873	-1.2146	3.0403	-1.2129
	0.8	3.7215	-2.4894	3.7733	-2.4934	3.8251	-2.4974	3.8769	-2.4976	3.9287	-2.4976	3.9805	-2.4976	4.0323	-2.4976
$Rd$	2	5.6526	-4.7252	5.6651	-4.6933	5.6912	-4.6443	5.7101	-4.6148	5.7294	-4.5868	5.7487	-4.5601	5.7680	-4.5333
	3	3.1298	-1.7740	3.1933	-1.7907	3.2568	-1.8162	3.3203	-1.8312	3.3838	-1.8462	3.4473	-1.8612	3.5108	-1.8762
	4	2.4304	-0.8579	2.4898	-0.8670	2.5492	-0.8761	2.6086	-0.8852	2.6680	-0.8943	2.7274	-0.9034	2.7868	-0.9125

**CONCLUSIONS**

The hydromagnetic flow of a Powell-Eyring nanofluid with the oscillatory pressure gradient through the vertical channel was investigated, accounting for the effects of thermal radiation and Joule’s heating. This study is helpful in describing the thermal characteristics of the blood flow in the circulatory system. The Shooting technique along with the 4<sup>th</sup> order R-K method is employed to solve the transformed flow equations. Our analysis indicates that the Joule’s heating and thermal radiation affect the flow. An increase in Grashof

number and frequency parameter enhances the velocity, whereas the velocity decreases as increasing the intensity of the magnetic field and non-Newtonian parameter. The fluid temperature raises for the higher values of the Eckert number, heat source parameter, radiation parameter, and nanoparticle volume fraction. The unsteady velocity of the fluid and unsteady temperature oscillate with time due to the impact of periodic pressure gradient. From the calculated results, we observed that by increasing the rheological parameter of the base fluid and the intensity of the magnetic field, the heat transfer rate weakens at the left wall. Further, highest rate of heat transfer occurs for the case of platelets ( $m = 5.7$ ). The hydrodynamic case of the nanofluid flow with a pulsating pressure gradient can be captured by choosing  $M = 0$  and  $k_l = 0$

**REFERENCES**

1. S. S. Suri, H. Fenniri, B. Singh, *J. Occupat. Med. Toxicol.*, **2**(1), 1 (2007).
2. S. U. S. Choi, J. A. Eastman, *ASME Int. Mech. Eng. Cong. Expos.*, **66**, 99 (1995).
3. M. Hatami, J. Hatami, D. D. Ganji, *Comput. Methods, Programs, Biomedicine*, **113**(2), 632 (2014).
4. Y. Menni, A. J. Chamkha, A. Azzi, *Special. Top. Rev. Porous Media Int. J.*, **9**(4), 1 (2018).
5. J. Raza, A. M. Rohni, Z. Omar, *Int. J. Heat Mass Transfer*, **103**, 336 (2016).
6. M. Sheikholeslami, M. Hatami, D. D. Ganji, *Powder Technol.*, **246**, 327 (2013).
7. A. Vijayalakshmi, S. Srinivas, *J. Mech.*, **33**(2), 213 (2017).
8. K. V. Wong, O. De Leon, *Adv. Mechanical Eng.*, **2**, 519659 (2010).
9. F. G. Fowkes, G. D. Lowe, A. Rumley, S. E. Lennie, F. B. Smith, P. T. Donnan, *European Heart J.*, **14**(5), 597 (1993).
10. I. A. Mirza, M. Abdulhameed, S. Shafie, *Appl. Math. Mech.*, **38**(3), 379 (2017).
11. M. M. Molla, M. C. Paul, *Med. Eng. Phys.*, **34**(8), 1079 (2012).
12. G. B. Thurston, N. M. Henderson, M. Jeng, *Adv. Hemodynamics Hemorheol.*, T. V. How (ed.), Jai Press Inc, 2004.
13. M. Y. Abou-zeid, S. S. El-zahrani, H. M. Mansour, *J. Nucl. Part. Phys.*, **4**(3), 100, (2014).
14. S. Jafarzadeh, A. N. Sadr, E. Kaffash, S. Goudarzi, E. Golabe, A. Karimipourf, *Comput. Methods Programs Biomedicine*, **195**, 105545 (2020).
15. P. B. Kumar, S. Srinivas, *Eur. Phys. J. Special. Top.*, **230**, 1465 (2021).
16. W. Chang, G. Pu-Zhen, T. Si-Chao, X. Chao, *Prog. Nucl. Energy*, **58**, 45 (2012).
17. C. K. Kumar, S. Srinivas, A. S. Reddy, *J. Mech.*, **36**(4), 535 (2020).
18. G. Radhakrishnamacharya, M. K. Maiti, *Int. J. Heat Mass Transfer*, **20**(2), 171 (1977).

19. H. M. Shawky, *Heat Mass Transfer*, **45**(10), 1261 (2009).
20. S. Srinivas, C. K. Kumar, A. S. Reddy, *Nonlinear Anal. Model. Control*, **23**(2), 213 (2018).
21. R. K. Selvi, R. Muthuraj, *Ain Shams Eng. J.*, **9**(4), 2503 (2018).
22. P. B. Kumar, S. Srinivas, *Mater. Today, Proc.*, **9**, 320 (2019).
23. S. B. Islami, B. Dastvareh, R. Gharraei, *Int. J. Heat Mass Transfer*, **78**, 917 (2014).
24. M. Sheikholeslami, T. Hayat, A. Alsaedi, *Int. J. Heat Mass Transfer*, **96**, 513 (2016).
25. S. O. Adesanya, J. A. Falade, O. D. Makinde, *Sci. Bull., Politeh. Univ. Buchar., Ser. D*, **77**(1), 25 (2015).
26. M. R. Eid, A. F. Al-Hossainy, M. S. Zoromba, *Commun. Theor. Phys.*, **71**(12), 1425 (2019).
27. N. S. Akbar, A. W. Butt, D. Tripathi, *Results Phys.*, **7**, 2477 (2017).
28. M. Sheikholeslami, M. Sadoughi, *Int. J. Heat Mass Transfer*, **113**, 106 (2017).

## Flux and separation efficiency in nanofiltration with mixed solvents

M. J. Dencheva-Zarkova<sup>1</sup>, D. Yankov<sup>2</sup>, J. L. Genova<sup>1</sup>, I. Tsibranska<sup>2\*</sup>

<sup>1</sup>*Institute of Solid State Physics, Bulgarian Academy of Sciences, 72 Tzarigradsko Chaussee Blvd., 1784 Sofia, Bulgaria*

<sup>2</sup>*Institute of Chemical Engineering, Bulgarian Academy of Sciences, Acad. G. Bonchev Str. Bl. 103, 1113 Sofia, Bulgaria*

Received: November 30, 2021; Revised: May 11, 2022

Membrane processes meet the requirements for efficient and cost-effective separation methods, although they still have to solve challenges such as insufficient selectivity. The quality of separation is a problem particularly relevant to mixed solvents (ex. water-alcohol mixtures) given their numerous applications such as: extraction of bioactive molecules from renewable sources (plants, seaweed, by-products from the agro-food industry); separation of ethanol from water-ethanol systems. Achieving high flux and rejection is a major challenge for the membrane separation in view of alcohol recovery, production of low-alcohol beverages and others.

This article presents a brief overview of research in the field of mixed solvents nanofiltration, experimental evidence and theoretical interpretation of the observed effects. Own results with NADIR NP030 P membrane are presented. Model water-alcohol mixtures, as well as red wine (Mavrud) nanofiltration are investigated in view of flux and separation behavior relative to ethanol. Lower flux is observed with water-ethanol mixtures as compared to water. Improved separation efficiency towards ethanol and higher permeate flux is observed with increasing transmembrane pressure.

**Keywords:** nanofiltration, mixed solvents, ethanol separation.

### INTRODUCTION

Solute concentration and solvent recovery are among the most important implementations of membrane separation. The traditional practice in this field requires an essential energy input (up to ~50% of the energy required in the production process) [1, 2], while membrane filtration, used either alone or in combination with traditional processes, results in significantly reduced energy consumption. Furthermore, the target molecules, extracted from natural sources, or involved in the pharmaceutical production are often thermally labile, which allows to take advantage of membrane technologies that do not require elevated temperatures. In the field of extraction of bioactive compounds, the use of mixed solvents benefits from their high selectivity, but has to be considered together with the problem of their subsequent separation and the requirements for green technologies.

The transport of neutral and charged molecules across membranes (nanofiltration, reverse osmosis) in hydro-organic media has been poorly studied, both experimentally and theoretically. The effect of the solvent composition and its subsequent separation, as well as the achievable flux and rejection of other organic substances from such solvents, are matters of essential importance. A solution to the problem of membranes selectivity towards mixed solvents is sought in the direction

of: new membranes; membrane processes; integration of several membrane processes [2].

As for the membrane material, the introduction of polymers and hybrid materials with improved permeability, selectivity, and long term stability are regarded as promising. Examples for synthesis and optimization of membranes for highly selective separations can be found, focused on solvent-resistant nano- and reverse osmosis membranes (OSN and OSRO) treatment of mixed solvents. In [3] a polyketone-supported polyamide was proposed with highly improved separation factor towards methanol/toluene solvents. Another successful membrane for binary solvent mixtures separation is proposed, based on the glassy amorphous copolymer (perfluoro-2,2-dimethyl-1,3-dioxole copolymerized with tetrafluoroethylene, (PDD-TFE), supported on an e-PTFE) [4].

Commercial OSN membranes (MPF, StarMem, DuraMem) were studied in view of separation capability towards a number of binary solvent mixtures with different physical and chemical properties [5, 6]. The membrane behavior (flux, contact angle, Hansen solubility parameter) was studied for a number of polyimide membranes in presence of a mixed solvent (hexane-isopropanol, hexane-ethanol) and compared to the pure ones (hexane, i-propanol, ethanol) [7]. A recent study compared the behavior of the NF 270 membrane (polypiperazine-amide) when filtering water-alco-

\*To whom all correspondence should be sent:  
E-mail: tsibranska@gmail.com

holic (methanol, ethanol, isopropanol) mixtures over a wide range of alcohol content and physicochemical characteristics: molecule size, hydrophobicity, Hansen-Hildebrand solubility parameters [8]. Fluxes and rejections were studied for binary mixtures, showing that hydrophilicity/ hydrophobicity and porosity of the membrane have greatest importance with respect to solvent permeability, as well as viscosity and polarity of the solvent mixture [9].

Some successful results have been reported for selective separations of binary and ternary solvent systems, such as water-alcoholic mixtures (methanol, ethanol, isopropanol) [8, 9]; binary alcoholic mixtures - methanol-ethanol [9]; ethanol-NMP, ethanol-DMSO; methanol-DMSO, methanol-NMP, toluene-methanol, toluene-NMP, toluene-DMF [4], methanol, toluene, pentanol, hexane binary and ternary mixtures [3], etc.

Regarding the separation mechanism, the size exclusion has to be considered together with several other important factors resulting from the physicochemical properties of the solute, the solute-membrane and solvent-membrane interactions, the membrane structure, etc. [1]. The important parameters are dielectric constant, surface tension, Hansen solubility and viscosity of the solvent. Concerning the dielectric constant and the Hansen solubility parameter, some authors report larger differences between the two solvents and smaller differences between the membrane and one of the solvents as favorable for a preferential permeation, resp. an improved separation to be observed [5]. Hydrophobic membranes, corresponding to low values of surface tension, are expected to have a small flux for solvents with high surface tension values and *vice versa* [5].

Nanofiltration from a hydro-organic solvent usually results in a lower permeate flow and a lower rejection of the target compounds compared to their values in aqueous medium. The explanation is sought in factors such as different viscosity, molar volume, surface tension, change in the polarity and the dielectric constant of the solvent and swelling of the membrane. In a binary solvent mixture, a preferential solvation results in different surroundings of the molecule, the effect being dependent on the relative amounts of the two solvents. The solvation of the solute and of the pore wall (swelling) affects solute rejection and the partial permeabilities of the components [9]. Polarity changes the solvation of the solutes and their size, while swelling can affect the effective pore size of the membrane.

A number of publications have considered the extraction of biologically active compounds from

mixed solvents [10, 11], but the role of the latter in the membrane separation is rarely commented on. Example of such research, where several membranes (based on polyamide and polypiperazine-polyamide) are studied, is given in [12]. Nanofiltration and reverse osmosis of water-ethanolic solutions containing glucose, proline, tyramine and tartaric acid have been performed. Solvent recovery from micro algae oil-solvent miscellas using OSN membranes was also concerned in view of its potential for industrial application in the oleochemistry [7]. Measured rejections of microalgae oil dissolved in different pure or mixed solvents are presented, highest values being obtained for hexane and hexane-*i*-propanol (3:2) mixtures depending on the membrane type. In [13] purification of omega-3 by nanofiltration was performed and the membrane behavior towards phospholipids and triglycerides from herring roe extract was studied, where dry extract was dissolved in a solvent with different water/ethanol ratio. Another field of membrane application to water-alcoholic systems is focused on the correction of the ethanol content in alcoholic beverages such as wine and beer. According to the properties of the different membranes, membrane technologies are applied both for wine concentration and for reduction of its alcohol content [14, 15]. Thin-film polypiperazine membrane XN45 has been used for red wine concentration [15]. RO98pHt M20 and NF M20 membranes were found suitable for red wine content and aroma enhancement or correction [14]. Reported results after NF or RO treatment are found successful with respect to the whole bouquet of flavors, antioxidants and other biologically active substances.

The effect of the alcoholic content in membrane filtration from water-alcoholic solvents is related both to the observed permeate flux and rejection. The significance, as well as the direction of this effect depends on the affinity of the alcohol for the membrane as compared to water. Polar solvents show lower permeate flux with hydrophobic membranes and higher when using hydrophilic ones; observed rejection coefficients of neutral molecules in organic solvents are usually lower than in aqueous media.

The impact of alcohol presence in water/alcohol mixtures affects the concentration polarization through viscosity and osmotic pressure; the observed mass transfer coefficients are of the order of  $10^{-5}$  m/s [8] and decrease with increasing alcohol content. Commonly used are diffusion coefficients for highly dilute aqueous media, while knowledge of their actual values often remains outside the scope of the

study. The thickness of the concentration polarization layer when filtering with water-alcoholic solvent is estimated at 1–2  $\mu\text{m}$  to 6–8  $\mu\text{m}$  depending on the method used. Fluid viscosity and osmotic pressure influence the concentration polarization in opposite directions.

When nanofiltrating mixed solvents, mutually compensating phenomena may occur. For instance, at higher alcohol content (above 20-30%) the observed resistance of the membrane remained constant because of the simultaneous increase of the pore size and the thickness of the membrane [8]. The latter is due to swelling of the polymer membrane and a changed mobility of the polymer chains. The calculation of the diffusion coefficients in solvent swollen membranes must be approached with care, accounting for the effects of the frame of reference and thermodynamic non-idealities. This also applies to the possibility for development of structure-property correlations and the design of membranes [1].

From a theoretical point of view these phenomena are poorly described. The final effect on permeate flux and selectivity can be observed, but is difficult to model and predict. Experimental observations for binary solvents separation with a number of membranes (MPF, StarMem and DuraMem) and solvent mixtures with different physical and chemical properties were modelled, the Hansen solubility parameters and polarity of membranes and solvents being the main factors affecting the separation [5, 16]. The modelling approach most often referred to the classical solution-diffusion theory [3, 4, 16]. Improved solution-diffusion model, specifically for solvent separation process in OSN, integrating the Hansen solubility parameter and the dielectric constant were proposed [5, 16]. Specific models for pure and mixed solvent flux, allowing the prediction of solute rejection in pure and mixed solvents were developed and tested with a number of experimental data and commercial OSN membranes (Puramem) [17, 18]. The filtration of water-alcoholic mixtures was satisfactorily modelled by the model of Spiegler and Kedem combined with the film theory [8]. The Spiegler – Kedem approach for multicomponent systems works with the differences in chemical potential on both sides of the membrane and does not directly involve interactions such as solute-membrane, or diffusion across the membrane.

The aim of this study is to present a brief overview of research in the field of mixed solvents nanofiltration, as well as own results for nanofiltration of model water-alcohol mixtures and

red wine (Mavrud) with membrane NADIR NP030 P.

## EXPERIMENTAL

The present investigation is focused on water-ethanol separation with model solutions, as well as preliminary experiments with red wine (Mavrud) nanofiltration. Flux behavior and separation ability of the membrane relative to the ethanol is studied.

A laboratory membrane filtration unit, (MaxiMem, Prozesstechnik GmbH) with a rectangular flat-sheet membrane of 215  $\text{cm}^2$  active area was used, Fig. 1. The experimental conditions for operating pressure, temperature, permeate flux, were precisely controlled and recorded for further analysis. Temperature regime with cooling was applied for red wine and ethanol-water model solutions.

The membrane (Microdyn Nadir™ NP030 with MWCO 500 Da) was subjected to previous adaptation with the solvent until constant flux. Cross-flow velocity of 1.2 l/min and transmembrane pressure of 10 bar was used as initial set of experimental conditions. The same initial feed volume ( $V_f = 750$ ) and final permeate volume ( $V_p = 0.6 V_f$ ) were kept in all experiments. Samples were taken after every 10 ml permeated volume.

Feed concentration ( $C_i$ ), final average concentration in the retentate ( $C_r$ ) and in the cumulative permeate volume ( $C_p$ ) were measured in order to estimate the final ethanol distribution  $C_p/C_r$  between the retentate and the permeate.



Fig. 1. MaxiMem membrane filtration unit

Ethanol-water model solutions with different ethanol concentrations in the range of 0 to 80% were subjected to nanofiltration. Dry red wine Mavrud was used in a preliminary set of experiments to check the separation ability in the presence of a complex composition and a number of biologically active substances. The red wine composition before nanofiltration is certified as follows: Specific gravity - 1.0495; Alcohol - 13.0 vol.% EtOH; Sugar - 0.99

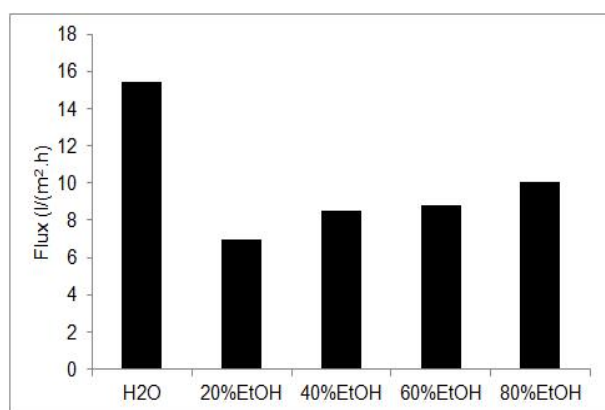
g/l; Total dry extract - 29 g/l; Total acidity - 4.58 g/l, Citric acid - less than 1.0 g/l; Volatile acidity - 0.41 g/l; Free SO<sub>2</sub> - 30.99 mg/l; Total SO<sub>2</sub> - 91.0 mg/l; Metals harmful to health - Iron - 0.01mg/l.

Ethanol concentration was quantified by HPLC analysis. Samples were analyzed on a chromatographic system consisting of a pump Smartline S-100 Knauer, refractometric detector - Perkin-Elmer LC- 25RI, column Aminex HPX-87H, Biorad, 300 × 7.8 mm and specialized software EuroChom, Knauer. 0.01 N H<sub>2</sub>SO<sub>4</sub> was used as mobile phase, at a flow rate of 0.6 ml/min. The temperature of the column was maintained at 65 °C. The standard deviation of the analysis didn't exceed 1.5%.

## RESULTS AND DISCUSSION

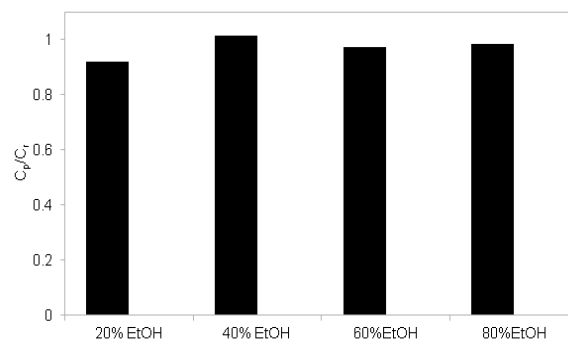
The experimental results with model water-ethanol solutions prove a pronounced decrease in the permeate flux ( $J$ , l m<sup>-2</sup>h<sup>-1</sup>) up to 20% ethanolic content, afterwards an increase is observed; however the flux remains much lower than the one in water, Fig. 2. Similar observations in the same concentration range are reported in [8]. The concentrations of ethanol in the permeate ( $C_p$ ) and the retentate ( $C_r$ ) in the model solutions remain close to each other, the ratio  $C_p/C_r$  being lower than 1. A trend to slight increase of the observed retention with the ethanol content is noticed (Fig. 3).

It was further investigated how this behavior is changing when filtering a complex multicomponent water-alcohol system.



**Fig. 2.** Permeate flux vs ethanol content in the model solutions.

Wine filtration experiments show a much lower permeate flux as compared to the model solutions, so the effects of transmembrane pressure and cross-flow velocity were explored in order to improve the flux behavior, Figs. 4a and 4b.

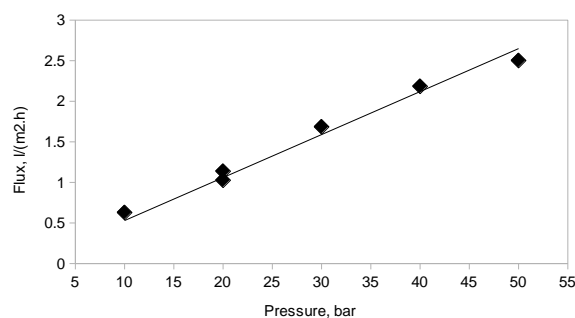


**Fig. 3.** Ethanol concentration ratio in permeate and retentate depending on the ethanol content in the model solutions.

### Effect of transmembrane pressure

In wine filtration at 10 bar, the observed low permeate flux tends to decrease during the experiment due to progressive membrane fouling. The value 0.63 l/(m<sup>2</sup>·h), obtained for 10 bars refers to a much lower filtered volume ( $V_p/V_f=0.08$ ) as compared to the rest of the data. For this reason, higher transmembrane pressures were preferred.

Wine filtration in the range of 10 to 50 bar has shown about a fivefold increase of the permeate flux, the dependence being linear (Flux= 0.053×Pressure, R<sup>2</sup>=0.99). No effect of membrane compressing at higher transmembrane pressure is observed. These results together with the observed linear time evolution of the permeated volume - R<sup>2</sup>>0.99 for transmembrane pressures 20 to 50 bar - confirm that favorable hydrodynamic conditions are assured in all filtration experiments. Fouling effect was observed at lower pressure (10 bar) and was reversible. The membrane regains its characteristics after washing and good reproducibility of the measured flux is observed on repeated experiment. This is illustrated in Fig. 4a with the measured permeate fluxes at 20 bars.



**Fig. 4a.** Permeate flux vs transmembrane pressure

### Effect of cross-flow velocity

Cross-flow velocity can effectively influence the filtration process by reducing possible concentration polarization and fouling and improving the conditions for higher and stable permeate flux. Three



different cross-flow velocities were applied – 1.2, 2 and 3 l/min. The rest of the conditions were transmembrane pressure 30 bar and permeated volume  $V_p=0.6V_f$  ( $V_f=750$  ml). The observed flux is less sensitive to change in the cross-flow velocity. A more significant increase is observed at 3 l/min, but the improvement of the permeate flux does not exceed 15%. An illustration of the flux behavior with different cross-flow velocities is given in Fig.4b.

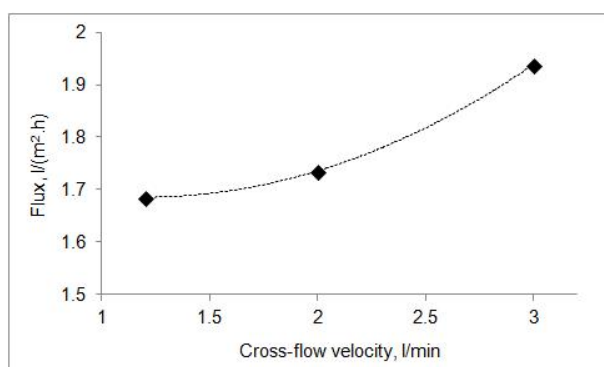


Fig. 4b. Permeate flux vs cross-flow velocity

The tendency of the membrane to retain ethanol is more pronounced in the multicomponent medium than in the model solutions and increases with applied pressure. No noticeable effect of the cross-flow velocity on the  $C_p/C_r$  ratio is observed. Fig. 5 illustrates the ethanol distribution between retentate and permeate, where  $C_p$  and  $C_r$  are average permeate and retentate concentrations.

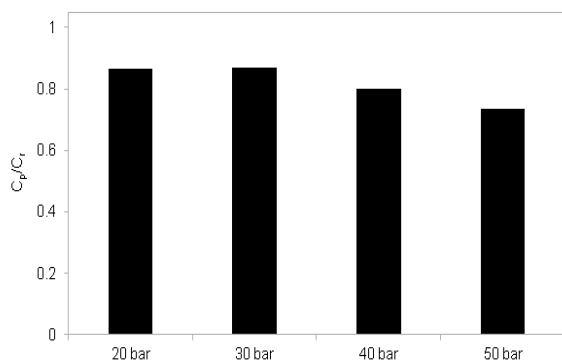


Fig. 5. Ethanol concentration ratio in permeate and retentate for wine filtration.

Results on wine concentration towards ethanol using a membrane with a similar MWCO and separation behavior have been published in [15]. The resulting permeate and retentate have been found useful in the alcohol industry. The observation that both permeate flux and ethanol retention increase with the operating pressure was found in [19].

As a compromise between energy input for pressure and cross-flow velocity on the one hand and flux and membrane separation efficiency on the

other, we preferred the following set of experimental conditions to be maintained in the studies: transmembrane pressure 30 bar, cross-flow velocity 1.2 l/min, temperature 19 °C. The check of the material balance for the before mentioned experimental conditions was fulfilled, the error being 0.24%. It was calculated as a percentage of the initial ethanol mass following the equation:  $V_f C_r = V_p C_p + V_r C_r$ . In general, there are two sources of error in the experiments performed - retention of a small part of the retentate volume in the system (check of  $V_f = V_p + V_r$ ) and insufficient prevention of alcohol loss during the experiment due to its volatile nature. Our experience showed errors up to 10-12% if these considerations are not taken into account.

## CONCLUSIONS

Water-ethanol separation of model solutions with nanomembrane Microdyn Nadir™ NP030 showed lower permeate flux as compared to water and a retention tendency, which is slightly increased with the ethanolic content. In the presence of higher viscosity and complex multicomponent composition, the permeate flux is essentially reduced. However, it can be significantly improved by applying higher pressure and/or cross-flow velocity. The former has stronger effect on both permeate flux and ethanol retention. Their increase with operating pressure, as well as with cross-flow velocity is shown in nanofiltration of red wine Mavrud. The obtained results have to be interpreted in the context of the rest bouquet of biologically active substances contained in the wine, including their antioxidant activity.

**Acknowledgement:** The authors acknowledge with gratitude the financial support from the Bulgarian Science Fund, Ministry of Education and Science under Contract No KP-06-N47/1/26.11.2020.

## REFERENCES

1. M. Galizia, K. P. Bye, *Front. Chem.*, **6**, 511, (2018).
2. L. Peeva, A. Livingston, in: *Current Trends and Future Developments on (Bio-) Membranes*, Elsevier, 2019. p. 97.
3. C. Liu, R. Takagi, D. Saeki, L. Cheng, T. Shintani, T. Yasui, H. Matsuyama, *J. Mem. Sci.*, **618**, 118710 (2021).
4. J. Chau, K. K. Sirkar, *J. Mem. Sci.*, **618**, 118663 (2021).
5. J. Li, J. Wang, M. Huang, Y. Luo, B. Zhang, Q. Yuan, *RSC Advances*, **4** (77), 40740 (2014).
6. P. Silva, S. Han, A. G. Livingston, *J. Mem. Sci.*, **262** (1-2), 49 (2005).
7. C. Lopresto, S. Darvishmanesh, A. Ehsanzadeh, A. Amelio, S. Mazinani, R. Ramazani, B. Van der

- Bruggen, *Biofuels, Bioprod. Bioref.*, **11** (2), 307 (2017).
8. T. V. N. Nguyen, L. Paugam, P. Rabiller, M. Rabiller-Baudry, *J. Mem. Scien.*, **601**, 117907 (2020).
  9. J. Geens, K. Peeters, B. Van der Bruggen, C. Vandecasteele, *J. Mem. Scien.*, **255**, 255 (2005).
  10. A. Trojanowska, I. Tsibranska, D. Dzhonova, M. Wroblewska, M. Haponska, P. Jovancic, V. Marturano, B. Tylkowski, *Chem. Engin. Res. Des.*, **147**, 378 (2019).
  11. I. Saykova, B. Tylkowski, C. Popovici, G. Peev, *J. Chem. Technol. & Metall.*, **53** (2) (2018).
  12. J. Labanda, J. Sabaté, J. Llorens, *Desalination*, **315**, 83 (2013).
  13. M. Uler Zefikj, Performance of Organic Solvent Nanofiltration Membrane for Purification of Omega-3 (Master's thesis, NTNU), 2017.
  14. I. Ivić, M. Kopjar, V. Jukić, M. Bošnjak, M. Maglica, J. Mesić, A. Pichler, *Molecules*, **26** (4), 874 (2021).
  15. S. Banvolgyi, I. Kiss, E. Bekassy-Molnar, G. Vatai, *Desalination*, **198**(1-3), 8 (2006).
  16. J. Li, M. Wang, Y. Huang, B. Luo, Y. Zhang, Q. Yuan, *RSC Advances*, **4** (70), 37375 (2014).
  17. R. Goebel, M. Skiborowski, *Sep. Purif. Technol.*, **237**, 1163 (2020).
  18. R. Goebel, T. Glaser, M. Skiborowski, *Sep. Purif. Technol.*, **248**, 117046 (2020).
  19. D. A. F. Paredes, D. S. Laoretani, B. Morero, R. J. Sánchez, O. A. Iribarren, J. Espinosa, *Sep. Purif. Technol.*, **237**, 116339 (2020).

## A sulfur-based qualitative test for determining the presence of the secondary alcohol functional group of (-)-quinine and (+)-quinidine

I. V. Vasileva, I. N. Kolev\*

Department of Pharmaceutical Chemistry, Faculty of Pharmacy, Medical University "Prof. Dr. Paraskev Stoyanov" – Varna, 84 "Tzar Osvoboditel" Blvd., 9000 Varna, Bulgaria

Received: December 16, 2021; Revised: March 22, 2022

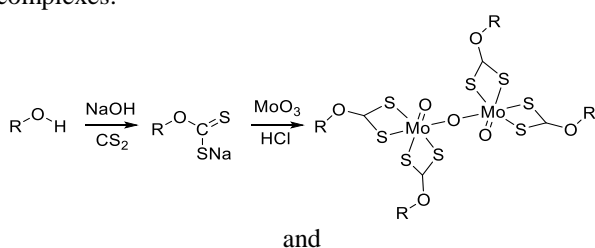
The present study describes a simple analytical qualitative technique for determining the presence of secondary alcohol groups in the composition of the drug enantiomeric pair (-)-quinine and (+)-quinidine. The analysis is based on the oxidation potential of molten sulfur ( $S_8$ ) and on the reactivity of the resulting  $H_2S$  to  $Pb(OAc)_2$ . In addition, a methodology for estimating the limit of detection (LOD) of the alkaloids in question was developed. The magnitude of these values for both analytes was established as  $\sim 0.006$  mg (or  $\sim 6.0$   $\mu$ g).

**Keywords:** pharmaceutical analysis, quinine, quinidine, secondary hydroxyl group, elemental sulfur

### INTRODUCTION

The qualitative analysis of raw drug substances containing secondary alcohol groups is a matter of paramount analytical importance [1, 2]. As a rule, the pharmacopoeial analysis of complexly structured alcohols includes the following two main strategies [3]:

a. implementation of complex-forming reactions; *i. e.* synthesis of distinctively colored mixed-ligand complexes:



b. treatment with the *Lucas' reagent* (an equimolar mixture (a solution) of anhydrous  $ZnCl_2$  and concentrated  $HCl$ ).

Although strictly specific, the first strategy requires the use of expensive, non-conventional, and potentially toxic reagents - inorganic salts and oxides; as well as the usage of larger quantities of hazardous solvents - benzene,  $CS_2$ , *etc.*

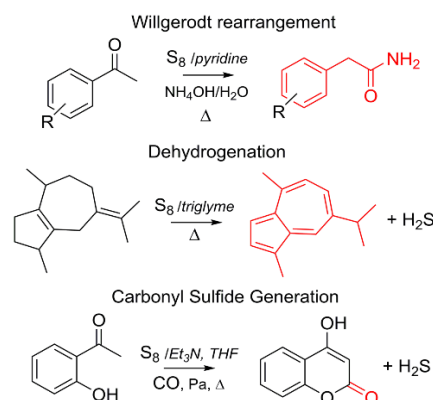
Lucas' reagent, on the other hand, has been usually employed as a "measuring stick" for checking the quality of bottled (the so-called pure commercial) alcohols or as a reagent for the systematic analysis (or even identification) of low-molecular-weight alcohols - saturated mono-functional alcohols having fewer than six or eight carbon atoms [4].

The oxidation-reduction analysis of secondary alcohols (inclusively pharmacologically-active

compounds containing  $2^\circ$  alcoholic groups) began early in 1957, when Feigl *et al.* [5] accomplished qualitative analysis of several artificial and natural compounds in the presence of the titled inorganic reagent - elemental  $S_8$ . Shortly thereafter, however, this redox test lost its practical value, being substituted by the ones pointed out above and by other analytical methods [3].

Sulfur ( $S_8$ ) is a non-toxic chemical element – an environment-friendly substance employed in various key industries [6]. Again, it has been used in the medical practice since ancient times as a mild keratolytic and antiseptic agent. In addition, one should take into account that  $S_8$  is also generally recognized as a safe and effective medicine - a very useful cure for the treatment of different skin diseases, including scabies [7, 8].

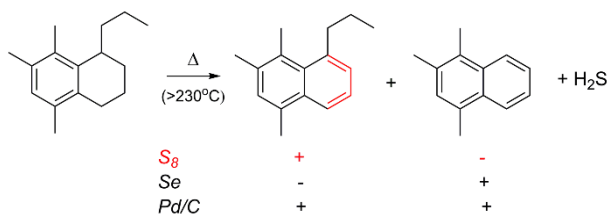
From the chemical point of view, however,  $S_8$  is principally used as a mild oxidizing agent (in the Willgerodt' reaction [9] and catalytic dehydrogenation of various organic substrates [10]) or as a reagent for the *in situ* formation of carbonyl sulfide [11] (Fig. 1).



**Figure 1.** The usage of elemental sulfur in organic synthesis - representative reactions [12].

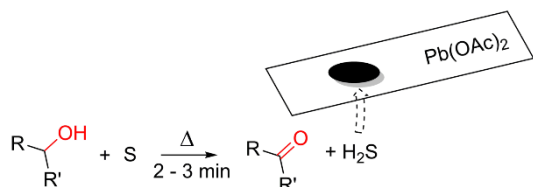
\* To whom all correspondence should be sent:  
E-mail: [ilian.kolev@mu-varna.bg](mailto:ilian.kolev@mu-varna.bg)

Moreover,  $S_8$  is the reagent of choice when performing dehydrogenation of aromatizable substrates (hydrocarbons) (Fig. 2):



**Figure 2.** Illustration of the effectiveness of elemental sulfur in dehydrogenating reactions [12, 13].

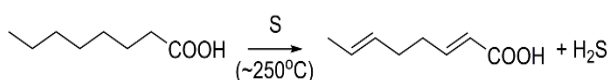
In the majority of cases, however, when nonvolatile organic samples containing secondary alcohol groups are fused for a short time with sulfur, hydrogen sulfide is split off no matter what other functional groups or elements are present in the analytes' composition [14]. From the analytical point of view, the evolved  $H_2S$  gas, in turn, can be readily detected, even in traces, with a piece of filter paper moistened with  $Pb(OAc)_2$  (Fig. 3).



**Figure 3.** Schematic representation of the oxidation reaction of secondary alcohols in the presence of  $S_8$ .

According to Feigl [14] the current redox reaction seems to be especially realizable with analytes that melt at  $120\text{--}180^\circ\text{C}$ .

In this context, an analogous pyrolytic splitting out of  $H_2S$  gas may occur when long-chain fatty acids (e.g., palmitic, stearic, and oleic acid) and waxes (*non-aromatizable representatives*) are heated to about  $250^\circ\text{C}$  along with  $S_8$  [14] by analogy with the ex-mentioned aromatizable hydrocarbons (Fig. 2).



**Figure 4.** Oxidation of long-chain fatty acids with elemental sulfur

In these and other cases (as shown in Figs. 2 and 4; *cf.*), however, the reaction proceeds so sluggishly that no traceable result can be sensitively (and readily) detected within the first three minutes; even when a lot of  $S_8$  is used. (Even when heated with small amounts of  $S_8$ , secondary alcohols rapidly release hydrogen sulfide; unlike other classes of compounds).

A series of positive analytical tests including the pharmacopoeial representatives *Chinidini sulfas* and *Chinini sulfas* was successfully carried out in order to boost the potential of Feigl's test when utilized for pharmaceutical analyses. A strategy for converting both drugs into analytically pure alkaloid bases was also employed. Moreover, the need of introducing  $S_8$  in the form of a  $CS_2$  solution was eliminated by the methodological modification imposed herein. The paper also presents an original microanalytical method for estimating the LOD values of the two alkaloids.

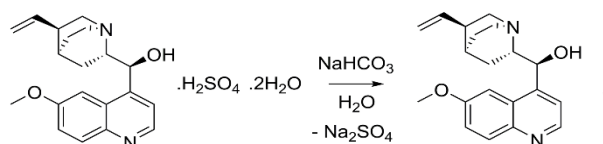
## MATERIALS AND METHODS

All chemicals were of analytical grade and used as received without any further purification: quinidine sulfate salt dihydrate ( $\geq 80\%$  quinidine;  $\leq 20\%$  dihydroquinidine, Sigma-Aldrich), quinine hemisulfate salt monohydrate (BioReagent,  $\geq 98\%$ , Sigma), sulfur (99.5+%, refined, Acros Organics),  $NaHCO_3$  (99.5%, for analysis, Acros Organics),  $NaI$  (99+%, extra pure, Fisher Chemicals). The used solvent (acetone in this case) was received from Fisher Scientific. All tests were performed in a well-ventilated hood. To confirm the repeatability of the current analytic procedure, all trials were repeated thrice three days apart.

### Procedure of acetone purification

As used herein "commercially available acetone" was purified by the following method [15]: In a 100 mL round-bottom flask, approximately 10 g of finely powdered  $NaI$  was dissolved in 50 mL of boiling acetone. Crystals of  $NaI \cdot 3Me_2CO$  were obtained from the solution thus prepared at cooling to  $-8^\circ\text{C}$  (in a freezer). The crystals were filtered off and washed thoroughly with "hot" air. Acetone distils off readily on warming.

### Conversion of quinidine sulfate to quinidine base



**Figure 5.** Synthesis of quinidine base from quinidine sulfate.

The conversion of quinidine sulfate to quinidine (Fig. 5) was accomplished by the following protocol: Quinidine sulfate (0.3 g) was dissolved in 30.0 mL of distilled water in a 50 mL beaker under constant magnetic stirring at room temperature. After 10 minutes, 0.6 g ( $\sim 10$  equivalents) of  $NaHCO_3$  was added in small portions to the resulting solution still under continuous stirring (300 rpm). After

completing the addition of  $\text{NaHCO}_3$ , the resulting slurry was stirred for additional 30 minutes. The obtained precipitate was removed by filtration (*via* a glass funnel filter with sintered glass disc) and washed repeatedly with precooled distilled water. The crude product thus obtained was kept in a vacuum desiccator charged with  $\text{P}_2\text{O}_5$  for a period of 48 hours (yield = 95.0%). Melting range (after drying at  $120^\circ\text{C}$  for 1 hour):  $171.5\div 172.4^\circ\text{C}$  (determined in an open capillary tube with a Krüss Optronic melting point apparatus). Ref. [16]: M.p.  $174\div 175^\circ\text{C}$  (anhyd.).

#### Conversion of quinine sulfate to quinine base

As mentioned previously in the case of the conversion of quinidine sulfate to quinidine base the yield = 97.0%. Melting range (after drying at  $120^\circ\text{C}$  for 1 hour):  $174.5 \div 176.8^\circ\text{C}$ . Ref. [16]: M.p.  $176\div 177^\circ\text{C}$  (anhyd.).

#### Spot test procedure

A glass microtest tube (0.1 mL capacity) was used. A little of the solid ( $\sim 1\div 2$  mg; quinine-*base* or quinidine-*base*, respectively) was treated with a pinch of sulfur. The mouth of the tube was plugged up with a piece of filter paper moistened with  $\text{Pb}(\text{OAc})_2$ . The tube was then placed in a silicone bath previously heated to  $200^\circ\text{C}$ . If necessary, the temperature might be raised to  $210^\circ\text{C}$ . If secondary alcohols were present, a black or brown stain (of  $\text{PbS}$ ) appeared on the paper within three minutes.

#### Limit of detection (LOD)

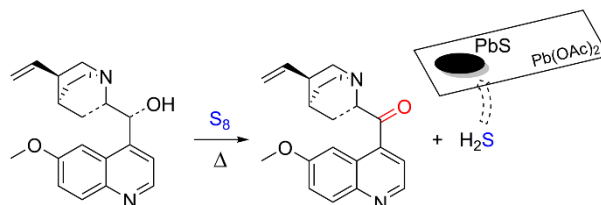
Glass capillary microtubes with a capacity of 0.045 mL were used to evaluate the analytical sensitivity. The tubes were firstly loaded with a minimum amount of elemental sulfur; so as to obtain a  $\text{S}_8$  deposit of about 3.0 mm each in height. Then, by means of a microsyringe, aliquots (2.0  $\mu\text{L}$ ) of each test solution were directly injected into the sulfur content of each test tube. For the purpose of the analysis, a set of standard (acetone) solutions with known concentrations of both alkaloids was prepared, namely: 8.0, 6.0, 4.0, 2.0, 0.8, 0.2, and 0.08 mg/mL. The contents of the tubes were then brought to dryness in a drying oven at  $40^\circ\text{C}$ .

Next, the open ends of the tubes were stopped with a piece of filter paper moistened with a drop ( $\sim 5.0$   $\mu\text{L}$  in volume) of 10% lead acetate solution. The tubes were then immersed a few millimeters deep into a silicone bath pre-heated to  $200^\circ\text{C}$ . The appearance of traces of  $\text{PbS}$  (which we interpreted as a positive response) on the reagent paper revealed the formation of hydrogen sulfide. All tests were performed in triplicate. In addition, when testing

acetone solutions, it is advisable to perform a blank test with the solvent used.

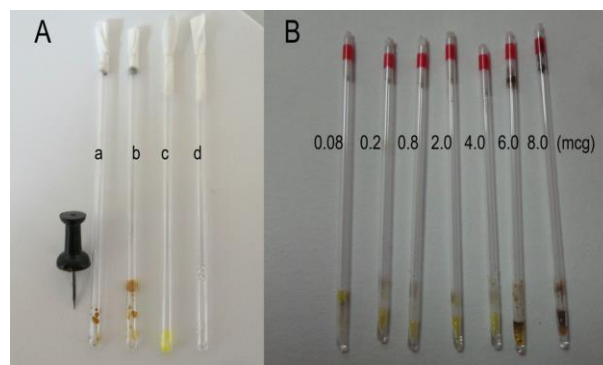
## RESULTS AND DISCUSSION

To supplement the potential of Feigl's test in the field of the pharmaceutical analysis, we initiated a series of tests for investigating with  $\text{S}_8$  the reactivity (reduction one) of the medicines in question (Fig. 6). It should be pointed out that, in the cases where salts of organic bases are analyzed, it is necessary beforehand to release the organic constituent (low-melting organic base) from the inorganic one. That is why, in the current work, the procedures for the synthesis of the relevant alkaloid bases are presented in more details. The chosen strategies for purifying the corresponding bases and solvent (acetone), at large, exclude the possibility of the appearance of artifacts.



**Figure 6.** Proposed route of the applied redox reaction between the used Cinchona' alkaloids and elemental  $\text{S}_8$ .

Actually, as expected, a positive analytical response was observed when an insignificant amount of the examined compounds (powders) was fused with elemental sulfur (Fig. 7A). The appearance of black-colored spots of  $\text{PbS}$  on the impregnated caps was recorded within one minute. The maximum time required to reach the level of assured analytical perception (maximum intensity), however, was estimated to be 3.0 minutes.



**Figure 7. A.** A photograph illustrating the appearance of a dark stain (of  $\text{PbS}$ ) on  $\text{Pb}(\text{OAc})_2$  paper piece when a little of quinidine base was fused with  $\text{S}_8$  (tubes **a** and **b**), as well as the absence of a false-positive result from the independent melting of sulfur (**c**) and quinidine (**d**); **B.** A photograph illustrating the result of the LOD determination technique thus applied.

From an analytical point of view, however, the so-formed PbS spots may also be used as a means (analytical marker) for estimation of the so-called "limit of detection" - the numerical expression of the sensitivity (organoleptic one) in the present analytical test (Fig. 7B). So, properly "configured", the present method can also be employed as an analytical tool for detecting traces of the investigated analytes. Though, to register extremely small amounts of the analytes in question it is necessary to select reaction vessels with the smallest possible capacity. For this purpose, glass capillary microtubes with a total capacity of 45 microliters were selected as completely suitable. Regarding the precise and accurate transfer of submicrograms of both analytes in each microtube, the *dried droplet sample deposition technique* was employed in preparing all the samples [17, 18]. Actually, this technique allowed us to examine the two analytes in the form of micro-residues evaporated from acetone (onto the surface of S<sub>8</sub> particles).

Aliquots of each working solution were withdrawn using a 10- $\mu$ l GC micro-syringe to be delivered exactly where needed, *i.e.* at the bottom of each capillary microtube; and then transferred directly into the volume of S<sub>8</sub> already introduced. The total length of the needle used has, however, a direct bearing on the reproducibility of the test; it must reach the bottom of each capillary microtube. As expected, the analysis revealed that the examined analytes thus deposited into the vessel content, do come into direct contact with the introduced oxidizing agent - S<sub>8</sub>. Otherwise, a part of the analyte will be deposited outside the reaction zone, *i.e.* far from the deposited sulfur. As for the analytical sensitivity already achieved, its value will be reduced drastically in this case.

Special precautions must also be observed when evaporating the solvent (acetone) used. Much attention should be paid to avoid localized overheating the samples. Otherwise, significant amounts of the introduced samples can be pushed out of the capillary volume. That is why the resulting suspensions were allowed to evaporate slowly in a drying oven - at 40 °C in a matter of hours. The little that ultimately remains in every capillary must visually resemble the sulfur implemented - the reagent used in excess. All capillaries were then plugged with small pieces of tightly wound filter paper. The latter should be wetted with a specific amount of freshly prepared solution of lead acetate; taking care, here, the droplets deposited not to exceed the sorption capacity of the paper stoppers used. After being thus charged and plugged, the

capillaries were placed in a silicone bath preheated to 200°C. The total annealing time of the samples was 3 minutes. During this time, the main analytical (oxidation) reaction took place. Along with this, the resulting melt also changes both its color and its texture. The resulting dark brown color of the melts was preserved even after their cooling/solidifying. Cooled to room temperature, the samples were allowed to stand for another 3 minutes, but in a horizontal position. That allowed the residual H<sub>2</sub>S to react exhaustively with the impregnated lead acetate. Thus conducted, the method is able to establish minimal amounts of the analytes studied.

Using the newly developed analytical protocol, we were able to establish accurately the limits of detection (LODs) of the two alkaloids - *quinine* and *quinidine*. The analysis showed that the magnitudes of these values for both analytes were equal to ~ 0.006 mg (or ~ 6.0  $\mu$ g). Furthermore, the results established here, are very similar to those recorded by Feigl, but for other alkaloids [5, 16].

In order to justify the above-proposed route of the applied redox reaction and exclude a possible presence of false-positive reactions, additional tests were separately performed both with S<sub>8</sub> (Fig. 7A-c) and with quinidine (Fig. 7A-d).

As expected, none of the blank samples used gave a false-positive outcome. A negative response was also registered even at fusing of larger amounts of the high-melting drug salts used - *Chinidini sulfas* and *Chinini sulfas*.

Moreover, the proposed method applied on a much larger scale, may be particularly useful in the production of the alkaloid *quininone* (Fig. 6).

## CONCLUSION

The present paper describes yet another analytical strategy for the *quinidine* and *quinine* qualitative analysis - a strategy that selectively registers the presence of hydroxyl groups in the analytes studied. The need of using harmful solvents has also been rejected by the imposed herein modifications of the method.

Being accurate and reproducible, the presented approach appears to be completely applicable and suitable for the routine second identification analysis (pharmaceutical one) of the raw drug substances *Chinidini sulfas* and *Chinini sulfas*.

The benefits of the method are: its employing inexpensive and easily available chemicals - elemental sulfur, acetone, and its being easy to implement by a wide range of researchers and even students.

REFERENCES

1. European Pharmacopoeia, Strasbourg: Council of Europe, 10th edn., vol. 1 and 2, 2019.
2. O. Pedersen, Pharmaceutical Chemical Analysis: Methods for Identification and Limit Tests, Boca Raton, Taylor & Francis Group, 2006.
3. S. K. Bhasin, R. Gupta, Pharmaceutical Organic Chemistry, Elsevier, 2012.
4. R. A. Kjonaas, B. A. Riedford, *J. Chem. Educ.*, **68**, 704 (1991).
5. F. Feigl, V. Gentil, C. Stark-Mayer, *Microchim. Acta*, **45**, 341 (1957) (in German).
6. C. T. Walsh, The Chemical Biology of Sulfur, Royal Society of Chemistry, 2020.
7. M. W. Mann, D. L. Popkin, Handbook of Dermatology: a Practical Manual, Wiley Blackwell, 2020.
8. L. E. Millikan, Drug Therapy in Dermatology (Basic and Clinical Dermatology), Informa Healthcare, 2000.
9. B. P. Mundy, M. G. Eller, F. G. Favalaro Jr., Name Reactions and Reagents in Organic Synthesis, 2005.
10. N. S. Gill, F. Lions, *J. Am. Chem. Soc.*, **72**, 3468 (1950).
11. K. Konishi, I. Nishiguchi, T. A. Hirashima, *Synthesis*, 254 (1984).
12. J. A. Morrison, Sulfur. Encyclopedia of Reagents for Organic Synthesis, Wiley, doi:10.1002/047084289x.rs132, 2021.
13. W. Cocker, B. E. Cross, J. T. Edward, D. S. Jenkinson, J. McCormick, *J. Chem. Soc.*, 2355 (1953).
14. F. Feigl, Spot Tests in Organic Analysis, Elsevier, Amsterdam, 1966.
15. W. L. F. Armarego, Purification of Laboratory Chemicals, 8th edn., Elsevier Butterworth-Heinemann, 2017.
16. J. Buckingham, K. H. Baggaley, A. D. Roberts, L. F. Szabo, Dictionary of Alkaloids, 2nd edn., CRC Press, 2010.
17. Y. Liu, J. Pan, G. Zhang, Z. Li, Z. Hu, Y. Chu, L. Guo, C. Lau, *Anal. Chim. Acta*, **1151**, 338253 (2021).
18. M. Šebela, E. Jahodářová, M. Raus, R. Lenobel, P. Hašler, *PLoS One*, **13**, e0208275 (2018).

## Optimization of the operating parameters of microbial electrolysis cell assisted anaerobic digester for generating bioenergy from an ethanol stillage

P. G. Velichkova\*, M. R. Popova, A. T. Angelov

*Department of Engineering Geoecology, University of Mining and Geology "St. Ivan Rilski", Sofia 1700, Bulgaria*

Received: January 05, 2022; Revised: April 13, 2022

In order to improve the process of biomethanation, a hybrid system anaerobic digester - microbial electrolysis cell (AD-MEC) was created. The influence of different technological parameters on the operation of the installation in the purification of ethanol stillage was studied. It was found that 0.8 V is the optimal external load at which 80 % of methane in the biogas and a yield of 18.10 l CH<sub>4</sub>/kg COD is reached. The applied external voltage of 1.0 V did not promote the yield of methane (14.13 l CH<sub>4</sub>/kg COD), but the amount of methane in the biogas was 70 %, which is higher than the 52 % obtained for a stand-alone process. The influence of working pH and temperature was studied at different values for the biomethanation process. The best results for the hybrid AD-MEC system were obtained at pH 7.5 and temperature 35 °C. Such values are characteristic of the biomethanation process, as methanogenic bacteria are very sensitive to abrupt changes in the environment (pH below 6.8, presence of oxygen, very low or high temperatures, etc.).

**Keywords:** anaerobic digester, microbial electrolysis cell, ethanol stillage, bioenergy, parameters

### INTRODUCTION

Anaerobic digestion (AD) is a key technology for converting organic matter into methane-rich biogas. However, there are still limitations such as destabilization and poor decomposition of some substrates, as well as low biogas production [1-3]. This is mainly due to the accumulation of volatile fatty acids (VFAs), which rapidly lower the pH of the medium and the process becomes unstable.

A microbial electrolysis cell (MEC) system is similar to that of a microbial fuel cell and overcomes the thermodynamic barrier by means of small applied voltages (0.5-1.0 V). This makes the process independent of the reactor surface area, which benefits the economic feasibility. The biocatalyzed electrolysis achieves this by utilizing electrochemically active microorganisms, which convert dissolved organic material to bicarbonate, protons and electrons. Externally, the anode and the cathode are connected to the power supply using an electrical circuit. The power supply drives the released electrons from the anode to the cathode. At the cathode, protons and electrons combine to form hydrogen [3-6]. Electromethanogenesis synthesizes methane in two ways, either by direct uptake of electrons from the electrode, called direct electromethanogenesis, or mediated by hydrogen and other compounds such as acetate, formate which are produced and combined with carbon dioxide to form methane, called mediated or indirect electromethanogenesis [7, 8]. MEC is a promising technology for the removal of organic

pollutants and for biogas production. Many studies have revealed higher rates of degradation of different substrates in AD-MEC systems than in a single AD system [9-12]. The integration of MEC into an anaerobic reactor stabilizes the process by helping the decomposition of the substrate and thus leads to the production of hydrogen and methane. In addition, the rate of degradation of inflexible compounds or complex wastewater is higher in AD-MEC [3, 13, 14]. So, integrated AD-MEC systems have the ability to not only simultaneously produce biogas but also upgrade it. The combination of wastewater treatment along with biomethane production may help in compensating the cost of wastewater treatment, making the MEC technology more sustainable.

There are literature data on the study of the influence of one or two operating parameters on the work of AD-MEC, but there is not enough generalized data on the optimal operating conditions of such a system. This is extremely important as it saves time and money, especially when scaling up the installation. In both the single anaerobic digestion process and the AD-MEC hybrid system, the operating conditions must be optimal in order to obtain the maximum amount of biogas with a high methane content. In the present work, the influence of several technological parameters will be studied - the magnitude of the applied external voltage, temperature and pH. The variation of the external voltage can indirectly affect the solution pH and alkalinity due to abiotic reactions on the electrode surface of MEC and

\*To whom all correspondence should be sent:  
E-mail: polina.velichkova@mgu.bg

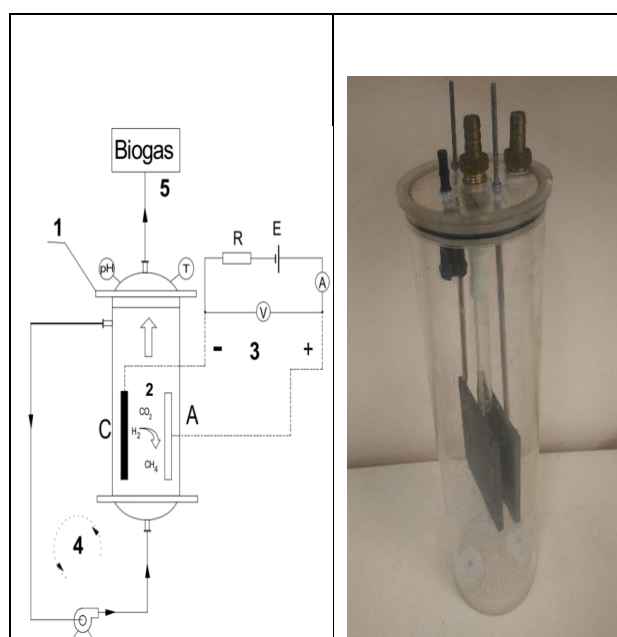


plays a key role in CH<sub>4</sub> generation and COD degradation [15, 16].

## EXPERIMENTAL

### Integrated AD-MEC system

Scheme and picture of a laboratory installation are shown on Figure 1. The anaerobic reactor is a Plexiglas tube with a diameter of 150 mm, a height of 400 mm and a working volume of 2.7 dm<sup>3</sup>. Two graphite plates measuring 100 × 100 × 6 mm were used for the electrodes and the distance between them – 20 mm, which were fastened with pins to the cover. Recirculation pumps moved the flow. The reactor system was filled with ethanol stillage and 10 % of volume of substrate inoculum from a mixed methanogenic consortium (activated sludge).



**Fig. 1.** Scheme of laboratory installation and pictures of AD-MEC. 1 - anaerobic bioreactor (UASB), 2 - MEC, 3 - MEC load chain, 4 - recirculation flow, 5 - biogas.

### Wastewater and activated sludge

Wastewaters were from “Almagest”, Verinsko Village, Bulgaria. They are obtained after the separation of ethanol obtained by enzymatic hydrolysis of maize. After obtaining the ethanol stillage, it was stored in a cool place at 4 °C. Before use the wastewater was neutralized to pH 7.5 with NaOH.

Activated sludge was also from “Almagest”. The culture is granulated in the form of spherical flocs (soft pellets). The particles have diameters varying in the range of 2-3 mm. The pellets displayed good mechanical stability, maintaining its intact structure at low stirring speeds, especially if no direct mechanical impact was applied.

### Analytical methods

Chemical oxygen demand (COD) was measured with a HANNA INSTRUMENTS kit. The contents of CO<sub>2</sub>, CH<sub>4</sub>, O<sub>2</sub>, H<sub>2</sub>S and H<sub>2</sub> in the emitted gas were measured using a portable gas analyzer "Draeger X-am 7000". The sulfate concentration was determined using a spectrophotometric method at λ 420 nm using BaCl<sub>2</sub> as reagent. Reducing sugars were determined as glucose using dinitrosalicylic acid (DNS) reagent by the method described by Miller [17]. The protein content was determined according to the method of Lowry *et al.* [18]. Dry weight was measured using a Kern DAB moisture analyzer balance.

## RESULTS AND DISCUSSION

### Characterization of the ethanol stillage

The values of the main parameters of ethanol stillage are shown on Table 1. As can be seen from the results, the ethanol stillage has a high organic load (COD 60-88 g/l), low pH (3.88) and relatively high contents of protein (9.4 g/l) and sugar (4.55 g/l, of which 0.28 g/l glucose). However, the best method for purification of this wastewater is its biochemical transformation accompanied by the generation of additional energy, i.e. the process of biomethanation. In addition, it was assumed that the stillage has a relatively good ratio of micro- and macronutrients necessary for the development of microorganisms in methanogenic consortia. For the fully balanced composition of the substrate both ammonium and phosphate salts are added [19].

**Table 1.** Characterization of the ethanol stillage

Parameter	Value
pH	3.88
Dry matter, %	4.15
COD, g O <sub>2</sub> /l	60-88
SO <sub>4</sub> <sup>2-</sup> , mg/l	288
Total protein, g/l	9.4
Reducing sugars, g/l	4.55
Glucose, g/l	0.28
Fructose, g/l	0.53
Maltose, g/l	3.34

### Influence of the magnitude of the applied external voltage

According to Choi *et al.* [20], increasing the external voltage from 0.5 to 1.0 V improves the decomposition while voltage higher than 1.0 V has a negative effect. Linji *et al.* [21] found that 0.8 V is the optimal external voltage. Lee *et al.* [22] found

that high voltages kill microorganisms. They also proved that there are different dominant populations in the anaerobic digestion reactor and the hybrid system. This means that the optimal external voltage is different for specific substrates in the AD-MEC system. The study will compare the kinetics of biogas production from an ethanol stillage without external voltage (independent process of anaerobic digestion) and at external voltages of 0.8 and 1.0 V in the AD-MEC system. The other conditions were kept the same - pH 7.5 and temperature 35 °C. The hydraulic retention time (HRT) required to be 10 days. The effect of external supplemental voltage of 0.8 and 1.0 V was tested on the CH<sub>4</sub> generation by using ethanol stillage. The cathode and anode electrodes were connected to the power supply, with an external resistance of 10 Ω. Figure 2 shows the graphs of the kinetics of a process without external voltage (only process of biomethanation), and at external voltages of 0.8 V and 1.0 V.

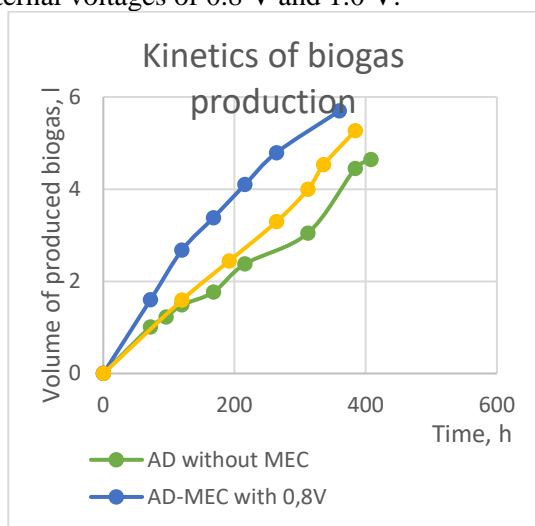


Fig. 2. Graphs of biogas production using different technology modes.

The biogas production was almost doubled by MEC with 0.8 V external voltage on the 240<sup>th</sup> hour, (10<sup>th</sup> day) compared to the other two modes. Therefore, the process is faster at MEC with 0.8 V. The relatively even release of biogas in the hybrid installation with 0.8 V is impressive, which is a prerequisite for a more stable process.

The data in Table 2 show that despite the higher organic load in the system with MEC, degradation is achieved up to about 74 % at 0.8 V and 59 % at 1.0 V external voltage. In the system without MEC, the degradation is 48 %. This means that the integration of MEC into AD improves the absorption of the substrate and speeds up the process. Methane yield per 10 days (required contact time) is also highest with a 0.8 V system (18.10 l CH<sub>4</sub>/kg COD), followed by a MEC-free process (16.48 l CH<sub>4</sub>/kg COD) and finally a 1.0 V AD-MEC system (14.13 l CH<sub>4</sub>/kg COD). The amount of sulfates also decreases at the output of the system, the greatest reduction being in a 0.8 V AD-MEC system (from 287 to 120 ppm). The biogas composition produced under the three modes is shown on Table 3. As can be seen, the biogas richest in methane was generated by the MEC-AD system with 0.8 V (80 %), followed by the system with 1.0 V (70 %) and without MEC (52 %).

#### Influence of operating temperature

Operating temperature is well known as one of the most effective factors for microbial kinetics and is therefore important for the identification and evaluation of the bacterial activity. Anaerobic digestion usually develops in the mesophilic (30–40 °C) and thermophilic state (45–60 °C) [23, 24].

Thermophilic operating temperature leads to an increase in the reaction rate, which increases the production of biogas and the rate of destruction of organic material; however, thermophilic bacteria are more sensitive than mesophilic ones to changes in the environment [25].

Table 2. Input and output parameters of the installation

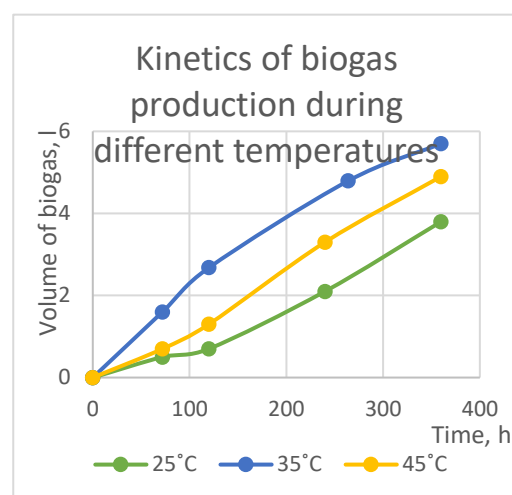
Parameter	System	AD without MEC	AD-MEC with 0.8 V	AD-MEC with 1.0 V
COD <sub>input</sub> , g/l		61	88	86
COD <sub>output</sub> , g/l		32.10	23.25	35.20
SO <sub>4</sub> <sup>2-</sup> input, mg/l		289	287	288
SO <sub>4</sub> <sup>2-</sup> output, mg/l		174	120	122
Methane yield, l CH <sub>4</sub> /kg COD on 10 <sup>th</sup> day		16.48	18.10	14.13

**Table 3.** Composition of produced biogas

System	Composition of biogas	CH <sub>4</sub> , vol. %	CO <sub>2</sub> , vol. %	H <sub>2</sub> S, ppm	H <sub>2</sub> , vol. %
AD without MEC		52	31	496	> 4
AD-MEC with 0.8 V		80	12	306	0.8
AD-MEC with 1.0 V		70	24	320	0.9

Kyazze *et al.* [26] reported that the optimum temperature of acetate-fed two-chamber MEC was about 30 °C. Production of biogas decreased at temperatures below 25 °C or above 40 °C due to lower activity of electroactive bacteria (EAB). In another study [27], the maximum current density generated by a single-chamber MEC was obtained at a temperature of 29-31 °C and also the decrease in COD shows a similar trend in the system. According to the results by Feng *et al.* [28], the performance of the AD-MEC under 25 °C and that of the AD system at 35 °C was almost similar. In a previous study the optimal temperature was determined as 35 °C for the same consortium for biomethanation of vinasse [29]. Meta-analysis presented by Amin *et al.* showed the established optimal temperature intervals and found that for AD-MEC it is between 30 and 40 °C [30]. They also found that the optimal activity of acidogenic, acetogenic and electrogenic bacteria is at a lower pH than the optimal pH for methanogenic bacteria. Methanogens, which are sensitive to changes in pH, have optimal activity in the pH range of 6.8–7.2. As a result, it is logical that the optimal temperature conditions to improve methane yield be different from the TCOD removal rate. According to the result, the choice of a temperature range of 30-40 °C, as made in many studies, has the best impact on methane yield. Therefore, the processes of biogas production from an ethanol stillage with AD-MEC at 25, 35 and 45 °C were studied at 0.8 V external voltage and pH 7.5.

The graphs on Figure 3 show that the highest biogas production is at 35 °C, followed by 45 °C and 25 °C, respectively. After 240 hours, (10 days) biogas production is almost doubled at 35 °C (4.5 l) vs 25 °C (2.1 l). At 45 °C, the produced biogas is 3.3 l. Low temperatures such as 25 °C have no positive effect on the biomethanation process, even when there is an integrated MEC. Higher temperatures such as 45 °C reduce biogas production, but manage to keep the process stable. This may be related to the type of methanogenic consortium which is immobilized on activated carbon and protects it from adverse external influences.

**Fig. 3.** Graphs of biogas production at different temperatures in AD-MEC.

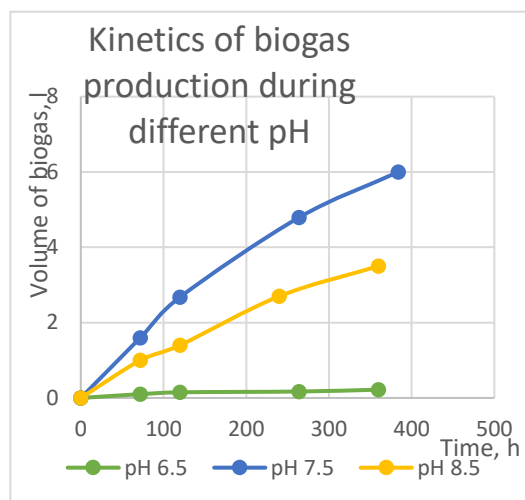
Perhaps maintaining a high temperature in the reactor for a long time will also lead to negative effects and inactivation of microorganisms. It is also economically unprofitable. Huang *et al.* [31] suggested that because of decreasing of methanogens activity, operation of anaerobic digesters under 25 °C could lead to an accumulation of VFAs. These results showed that the AD-MEC system could be a suitable alternative to elevate methane production at ambient temperature. Therefore, the optimal temperature for the combined AD-MEC system is 35 °C.

#### *Influence of operating pH*

The ideal conditions for methanogenic microorganisms are in a narrow pH range: 6.8-7.2. For systems, the optimal pH during hydrolysis and acidogenesis was reported to be between 5.5 and 6.5, while for methanogenesis the optimal pH was 7.0. In anaerobic bioreactors, pH defines the balance between carbonic acid, bicarbonate alkalinity and carbonate alkalinity, as well as between ammonia and ammonium ions [32, 33]. The process of biogas production with AD-MEC at pH 6.5, 7.5 and 8.5 was studied by keeping constant the other conditions - 0.8 V external voltage and 35 °C.

The graphs on Figure 4 show that the highest biogas production is at pH 7.5, followed by 8.5. As expected, at pH 6.5 almost no biogas was produced

because processes of hydrolysis and acidogenesis instead of methanogenesis took place. Therefore, the optimal pH for the combined AD-MEC system is the same as that for methanogenesis (7-7.5).



**Fig. 4.** Graphs of biogas production at different pH in AD-MEC

## CONCLUSION

The influence of different parameters on the operation of the hybrid system AD-MEC was studied. The optimal values of these parameters were established. The optimal external load is 0.8 V at which 80% methane in the biogas and yield of 18.10 l CH<sub>4</sub>/kg COD is reached. Unfortunately, at the applied external voltage of 1.0 V, the methane yield turned out to be even lower (14.13 l CH<sub>4</sub>/kg COD) compared to a stand-alone biomethanation process (16.48 l CH<sub>4</sub>/kg COD). Increasing the applied voltage above 1.2 V can lead to electrolysis of water and oxygen production, which not only affects electron transfer, but also has a negative effect on methanogenic bacteria. We found that low temperatures and low pH negatively affect the AD-MEC system, so the optimal values are 35 °C and pH 7.5.

**Acknowledgement:** This research is supported by the Bulgarian National Science Fund, Grant № KP-06-M47/3 from 26.11.2020.

## REFERENCES

- Z. Guo, W. Liu, C. Yang, L. Gao, S. Thangavel, L. Wang, Z. He, W. Cai, A. Wang, *Water Res.*, **125**, 170 (2017).
- J. Park, B. Lee, D. Tian, H. Jun, *Bioresour. Technol.*, **247**, 226 (2018).
- Z. Yu, X. Leng, S. Zhao, J. Ji, T. Zhou, A. Khan, A. Kakde, P. Liu, X. Li, *Bioresour. Technol.*, **255**, 340 (2018);

- B. E. Logan, D. Call, S. Cheng, H. V. Hamelers, T. H. Sleutels, A. W. Jeremiasse, R. A. Rozendal, *Environ. Sci. Technol.*, **42** (23), 8630 (2008).
- R. A. Rozendal, H. V. Hamelers, G. J. Euverink, S. J. Metz, C. J. Buisman, *Int. J. Hydrogen Energy*, **31** (12), 1632 (2006).
- E. Croese, A. W. Jeremiasse, I. P. Marshall, A. M. Spormann, G.-J. W. Euverink, J. S. Geelhoed, A. J. Stams, C. M. Plugge, *Enzyme Microbial Technol.*, **61**, 67 (2014).
- Aryal N., T. Kvist, F. Ammam, D. Pant, L. D. M. Ottosen, *Bioresour. Technol.*, **264**, 359 (2018).
- A. B. T. Nelabhotla, C. Dinamarca, *Appl. Sci.*, **9** (6), 1056 (2019).
- W. Cai, T. Han, Z. Guo, C. Varrone, A. Wang, W. Liu, *Bioresour. Technol.*, **208**, 13 (2016).
- L. Lu, Z. J. Ren, *Bioresour. Technol.*, **215**, 254 (2016).
- B. E. Logan, K. Rabaey, *Science*, **337** (6095), 686 (2012).
- R. C. Wagner, J. M. Regan, S.-E. Oh, Y. Zuo, B. E. Logan, *Water Res.*, **43** (5), 1480 (2009).
- B. R. Dhar, E. Elbeshbishy, H. Hafez, H. S. Lee, *Bioresour. Technol.*, **198**, 223 (2015).
- M. Mahmoud, P. Parameswaran, C. I. Torres, B. E. Rittmann, *Bioresour. Technol.*, **151**, 151 (2014).
- X. Guo, J. Liu, B. Xiao, *Int. J. Hydrogen Energy*, **38** (3), 1342 (2013).
- Z. Zhao, Y. Zhang, X. Quan, H. Zhao, *Bioresour. Technol.*, **200**, 235 (2016).
- G. L. Miller, *Anal. Chem.*, **31**(3), 426 (1959).
- O. Lowry, N. Rosebrough, A. Farr J. Randall, *J. Biol. Chem.*, **193**, 265 (1951).
- C. Eskicioglu, K. Kennedy, J. Marin, *Bioresour. Technol.*, **102**(2) 1079 (2011).
- K.-S. Choi, S. Kondaveeti, B. Min, *Bioresour. Technol.*, **245**, 826 (2017).
- X. Linji, L. Wenzong, W. Yining, W. Aijie, L. Shuai, J. Wei, *Int. J. Hydrogen Energy*, **38** (35), 15801 (2013).
- B. Lee, J.-G. Park, W.-B. Shin, D.-J. Tian, H.-B. Jun, *Bioresour. Technol.*, **234**, 273 (2017).
- J.K. Kim, B.R. Oh, Y.N. Chun, S.W. Kim, *J. Biosci. Bioeng.*, **102**, 328 (2006).
- T. Tian, S. Qiao, C. Yu, Y. Yang, J. Zhou, *Chemosphere*, **218**, 119 (2019).
- B. S. Zakaria, B. R. Dhar, *Bioresour. Technol.*, **289**, 121738 (2019).
- G. Kyazze, A. Popov, R. Dinsdale, S. Esteves, F. Hawkes, G. Premier, *Int J Hydrogen Energy*, **35**, 7716 (2010).
- H. Omid, A. Sathasivan, *Int Biodeterior. Biodegradation*, **85**, 688 (2013).
- Q. Feng, Y.-C. Song, D.-H. Kim, M.-S. Kim, D.-H. Kim, *Int. J. Hydrog. Energy*, **44**, 2170 (2019).
- P. G. Velichkova, T. V. Ivanov, I. G. Lalov, *Bulgarian Chemical Communications*, **49**, 74 (2017).
- M. Amin, A. Arvin, A. Feizi, B. Dehdashti, A. Torkian, *Biochemical Engineering Journal*, **178**, 108301 (2022).

31. Q. Huang, Y. Liu, B. R. Dhar, *Critical Reviews in Environ. Sci. Technol.*, **50**, 50 (2020).
32. M. H. Gerardi, *The microbiology of anaerobic digesters*, John Wiley & Sons, 2003.
33. C. M. Drapcho, N. P. Nhuan, T. H. Walker, *Biofuels engineering process technology*, McGraw Hill, 2008, ISBN: 9780071487498.

## A kinetic study on the effect of short-term frying cycles on the properties of cold-pressed peanut oil

G. Sangavi<sup>1</sup>, J. Jayapriya<sup>2</sup>, G. Nandhini Devi<sup>1\*</sup>

<sup>1</sup>Centre for Food Technology, Department of Biotechnology, Anna University, Chennai, Tamil Nadu, India

<sup>2</sup>Department of Applied Science and Technology, Anna University, Chennai, Tamil Nadu, India

Received: January 16, 2022; Revised: February 03, 2022

The present study investigated the effect of frying cycles on the fatty acid profile and physicochemical properties of cold-pressed peanut oil during preparation of French fries. The quality indices monitored are acid value, peroxide value, iodine value, total polar materials, hunter 'L', 'b' value, total colour difference and fatty acid composition. Results showed that significant changes ( $p < 0.05$ ) were observed in quality indices. Fatty acid profiling showed gradual increase in saturated fatty acid content and decrease in unsaturated fatty acid content during repeated deep fat frying cycles. Kinetic modelling reveals that the change in acid value, and total polar materials followed first-order kinetic model whereas iodine value, hunter 'L', 'b' value and total colour difference followed zero-order kinetic model. The correlation of frying cycle with the oil quality indices showed that frying cycle has strong positive correlation with total colour difference ( $r: 0.9966$ ) and strong negative correlation with hunter 'L' value ( $r: -0.9971$ ).

**Keywords:** cold-pressed peanut oil, kinetic modelling, fatty acid profiling, GC-MS.

### INTRODUCTION

Edible oil is an excellent reserve of energy and essential fatty acids which act as a carrier of fat-soluble vitamins in our body. Deep frying is one of the oldest and popular food preparations, which is a process of immersing food in oil at a high temperature of 150 to 200 °C [1]. The desirable flavour, colour and crispy texture makes deep-fat fried foods very popular [2, 3]. Physicochemical reactions such as thermo-oxidation, hydrolysis, polymerization, isomerisation or cyclization take place at the high temperature of the frying process, leading to the decomposition of frying oil and formation of oxidative compounds, which affects the quality of oil and fried product [4]. The decline in quality of frying oils can be monitored using quality parameters such as total polar materials (TPM), acid value (AV), peroxide value (PV), iodine value (IV), total colour difference (TCD), density and refractive index, etc. [5]. According to reports, cold-pressed oils are healthier than refined oils, since nutritive capacity of refined oil is lost after the refining process. Cold-pressed peanut oil (CPO) is pale yellow in colour and has the characteristic "nutty" flavour of roasted peanuts. It is highly nutritious due to high level of polyunsaturated fatty acids, tocopherols, phytosterols, carotenoids, chlorophylls and polyphenolics, as well as significant amount of resveratrol. The antioxidant and antimicrobial efficiency of resveratrol provides health benefits, such as the prevention of cardiovascular diseases, atherosclerosis and cancer [6]. The major fatty acids

of peanut oil are palmitic, stearic, oleic, linoleic and arachidic acid. Linoleic and oleic acids constitute up to 75 % of peanut oil [7, 8]. Oleic acid contributes to higher stability of peanut oil over other oils rich in polyunsaturated fatty acids, viz. sunflower oil, safflower oil, etc. [9].

The rate of deterioration of frying oil and formation of breakdown products differs based on various factors [10]. The optimum frying life, performance and quality changes of edible oil during frying can be estimated using kinetic models and the knowledge of kinetics helps us to predict quality changes and to determine the threshold reject point [11]. The objectives of the present work were to evaluate the effect of frying cycles on the physicochemical properties of CPO during frying experiments. The changes in physical and chemical parameters were modelled using kinetic equations and the relationship between the parameters and the frying cycle was also investigated.

### EXPERIMENTAL

#### *Frying experiment*

CPO and fresh potatoes were purchased from the local market in Chennai, Tamil Nadu. Potatoes were washed, peeled and cut into strips (1 cm × 1 cm × 6 cm). The samples of the potato slices (200 g) were randomly selected for frying. The frying operation was carried out in an Orbit DF30 3.5 L stainless steel electric deep fryer. The frying pot was filled with 3 kg of fresh oil and the frying oil-to-product ratio was maintained at 20:1 (w/w). Frying was carried out at 180 °C for 7 min. One frying cycle includes deep

\* To whom all correspondence should be sent:  
E-mail: projectsagnlabs@gmail.com

of French fries for seven min and draining of oil in the frying basket for one min. Seven consecutive frying cycles were carried out and oil was collected after each frying cycle, stored in tight screw cap bottles at -20 °C till further analysis.

#### *Physicochemical analysis of the oil samples*

##### *Fatty acid profiling*

Fatty acid methyl esters (FAMES) of the oil samples were prepared using a sodium methoxide-methanol solution [12]. FAMES were analysed by GC-MS (Thermo Scientific, Trace 1300- TSQ 8000 Evo). Separation of fatty acid methyl esters was carried out on a TG 5-MS column (30 m × 0.25 mm I.D; 0.25 µm film thickness). The GC-MS interface temperature was maintained at 240°C. Helium was used as a carrier gas at a constant flow rate of 1.0 ml/min. 1 µl of sample was injected by split-less mode with the injector port at 240 °C. The column temperature programme was as follows: 55 °C, held for 2 min; 7.5 °C/min to 180°C, held for 15 min; 8 °C/min to 230 °C, held for 15 min. For MS detection, electron ionization with 70 eV was used, with scan range of 50 -500 amu, scan rate 0.2012 s<sup>-1</sup>. The ion source temperature and transfer line temperature were at 240°C. Solvent cut of time/delay time of 2.3 min was used for detection. The peaks identification was according to retention times of the reference FAME standard. Peak areas were determined by ICIS peak detection algorithm.

##### *Physicochemical properties*

AV of the oil samples were determined by titration method [13] expressed as mg KOH/g of oil. For the determination of PV, 5 g of oil sample was mixed with 30 ml of acetic acid-chloroform (3:2 (v/v)). Then 0.5 ml of freshly prepared saturated potassium iodide solution was added followed by addition of 30 ml of distilled water. The liberated iodine was titrated with 0.01 N sodium thiosulfate solution using starch (1 %) as indicator. The values were expressed as meqO<sub>2</sub>/kg of oil [14]. IV was determined by adding 10 ml of carbon tetrachloride and 25 ml of Wijs solution to one gram of oil. The solution was kept in dark for 30 min followed by addition of 15 ml of potassium iodide (10 %) and 100 ml of distilled water. The solution was then titrated with 0.1 N sodium thiosulfate solution using starch as an indicator. A blank titration was carried out without the oil samples [15]. TPM (%) of the frying oil samples were measured directly with a cooking oil monitor (Testo 270 cooking oil tester).

Colour measurements of the oil samples were carried out using a Hunter Lab Ultra-Scan Vis spectrophotometer. The colour values were expressed as L (whiteness or brightness/darkness), a (redness/greenness) and b (yellowness/blueness). An optically clear glass cell with fixed path length of 20 mm was used for measurements [16].

##### *Kinetic modelling*

During frying various complex reactions take place and change in quality parameters are analysed using kinetic equations [11]. Chemical reaction kinetics is applied to quantify individual attribute of an ideal food system in form of the general rate law [17]:

$$dP/dt = \pm k P_n$$

where k is the rate constant (1/min), t the reaction time (min), n the reaction order and P represents a quantitative value for a quality attribute.

The food quality changes are generally modelled as zero- and first-order rate reactions. The rate equations (Equations 1 and 2) are as follows [17, 18]:

$$\text{Zero-order equation: } P = P_0 \pm kt \quad (1)$$

$$\text{First-order equation: } P = P_0 e^{\pm k.t} \quad (2)$$

where P<sub>0</sub> represents the value of a quality attribute at t=0. The coefficient of determination (r<sup>2</sup>) was used as primary criterion to select the best fit of the tested mathematical model to the experimental data. The higher the value of r<sup>2</sup> the better the model was taken to fit [19].

##### *Statistical analysis*

The physicochemical properties of oil samples were analysed in triplicate and the fatty acid profile was analysed in duplicate. The results of the experiments were expressed as the mean ± standard deviation. The data were subjected to analysis of variance (ANOVA) and the Duncan's test for the 5 % significance level using the SPSS software (Version 21, IBM, New York, USA).

## RESULTS AND DISCUSSION

### *Impact of frying cycles on fatty acid profile*

The fatty acid composition, monounsaturated /saturated fatty acid ratio (m/s) and polyunsaturated/ saturated fatty acid ratio (p/s) of fresh oil and oil samples of initial and final frying cycle are represented in Table 1.

**Table 1.** Fatty acid composition (%) of fresh cold-pressed oil and at first and seventh frying cycle

Fatty acids	Fresh oil	First frying cycle	Seventh frying cycle
C14:0	0.504 <sup>a</sup>	0.592 <sup>b</sup>	1.160 <sup>c</sup>
C16:0	20.440 <sup>a</sup>	22.092 <sup>b</sup>	32.942 <sup>c</sup>
C18:0	0.174 <sup>a</sup>	0.897 <sup>b</sup>	1.198 <sup>c</sup>
C20:0	3.313 <sup>a</sup>	3.894 <sup>b</sup>	4.606 <sup>c</sup>
C22:0	0.217 <sup>a</sup>	0.407 <sup>b</sup>	0.546 <sup>c</sup>
C24:0	0.142 <sup>a</sup>	0.183 <sup>b</sup>	0.428 <sup>c</sup>
C14:1	0.156 <sup>c</sup>	0.137 <sup>b</sup>	0.107 <sup>a</sup>
C16:1	1.418 <sup>c</sup>	1.197 <sup>b</sup>	0.883 <sup>a</sup>
C18:1	46.586 <sup>c</sup>	44.911 <sup>b</sup>	40.794 <sup>a</sup>
C18:2	25.234 <sup>c</sup>	24.375 <sup>b</sup>	16.760 <sup>a</sup>
C18:3	1.799 <sup>c</sup>	1.266 <sup>b</sup>	0.532 <sup>a</sup>
m/s	1.943	1.648	1.022
p/s	1.091	0.914	0.423

The values reported are mean values of duplicate experiments. Values with different superscripts within a row are significantly different ( $P < 0.05$ ). [C14:0-myristic acid; C16:0-palmitic acid; C18:0-stearic acid; C20:0-arachidic acid; C22:0-behenic acid; C24:0-lignoceric acid; C14:1-myristoleic acid; C16:1-palmitoleic acid; C18:1-oleic acid; C18:2-linoleic acid; C18:3-linolenic acid; m/s: monounsaturated/saturated fatty acid ratio; p/s: polyunsaturated/saturated fatty acid ratio].

A significant increase ( $p < 0.05$ ) in the saturated fatty acid content and decrease in the unsaturated fatty acids during the frying cycles was observed. The decrease in unsaturated fatty acids during repeated frying is due to oxidation and thermal degradation [20].

The decrease was particularly noticeable in polyunsaturated fatty acids contributing to their multiple unsaturated bonds' instability [21]. The fatty acids with double bonds are prone to oxidation due to the presence of  $\pi$  (pi) bonds [22]. The decrease in oleic and linoleic acid content of peanut oil during deep frying has been previously reported [9]. The m/s and p/s ratio of fresh oil was 1.943 and 1.091. The ratio decreased to 1.022 and 0.423 at the end of the seventh frying cycle.

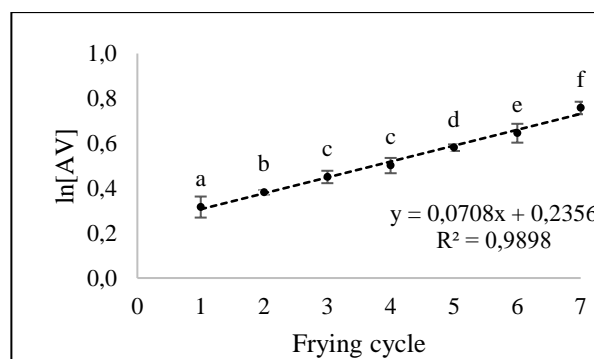
#### Impact of frying cycles on AV

AV is used as an indicator of hydrolytic rancidity of vegetable oils [9], which is associated with the amount of free fatty acids present in the oil. During frying water, steam and oxygen initiate a series of chemical reactions in oil and food which form carbonyl compounds which are then oxidized to low molecular weight free fatty acids [23, 24]. As shown in Table 2, the AV of fresh CPO was found to be  $1.309 \pm 0.030$  mg KOH/g of oil, which is within the limit suggested by the Codex Alimentarius Commission [25].

**Table 2.** Quality indices of fresh CPO

S. No	Quality index	Values
1	AV	$1.309 \pm 0.030$
2	PV	$4.290 \pm 0.587$
3	IV	$95.36 \pm 0.48$
4	TPM	$3.0 \pm 0.00$
5	Hunter 'L'	$83.685 \pm 0.056$
	Hunter 'b'	$30.937 \pm 0.040$

The values are expressed as mean  $\pm$  standard deviation. AV – acid value (mg KOH/g of oil); PV – peroxide value (meqO<sub>2</sub>/kg of oil); IV – iodine value (gI<sub>2</sub>/100 g); TPM – total polar materials (%).



**Figure 1.** Change in AV with respect to frying cycles on a natural log scale. The dotted line represents first-order fit. The standard deviation is denoted as error bars. Values with different data labels are significantly different ( $P < 0.05$ ).

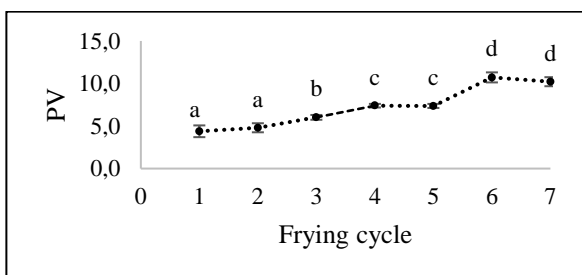
Fig. 1 shows the results of the kinetic study of the increase in AV of oil sample with each frying cycle. The AV of CPO increased significantly ( $p < 0.05$ ) with frying cycles. The AV of frying oil was reported to increase with the number of frying cycles and it is recognized that hydrolysis of oil/fat results in formation of free fatty acids, di-acyl glyceride, mono-acyl glyceride and glycerol [9, 26]. The first order kinetic model ( $r^2 = 0.9898$ ) was found to be adequate in describing the increase in AV with respect to the frying cycles. AV showed positive correlation with frying cycles, PV, TPM, hunter 'b' value, TCD and it showed negative correlation with IV and Hunter 'L' value (Table 3).

#### Impact of frying cycles on PV

The PV is the measure of primary oxidation products i.e., hydro-peroxides formed by oxidation of oil during frying [9]. PV of oil also varies with respect to the storage time, temperature and contact with air of the oil samples. As shown in Table 2, the PV of fresh CPO ( $4.290 \pm 0.587$  meqO<sub>2</sub>/kg of oil) was also within the limit suggested by the Codex Alimentarius Commission [25]. A significant change of PV is noted but there are inconsistencies in the change during each frying cycle (Fig. 2). The inconsistencies are due to the unstable nature of



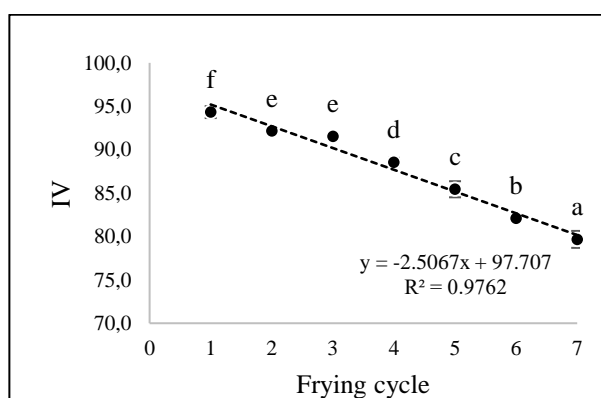
peroxides at high temperatures [27]. The peroxides break down to secondary oxidation products like carbonyl and aldehyde compounds causing the decrease in PV [28]. The similar phenomenon has been widely reported in the literature [9, 29]. PV showed positive correlation with frying cycles, AV, TPM, Hunter 'b' value, TCD and it showed negative correlation with IV and Hunter 'L' value (Table 3).



**Figure 2.** Change in PV with respect to frying cycles. The standard deviation is denoted as error bars. Values with different data labels are significantly different ( $P < 0.05$ ).

#### Impact of frying cycles on IV

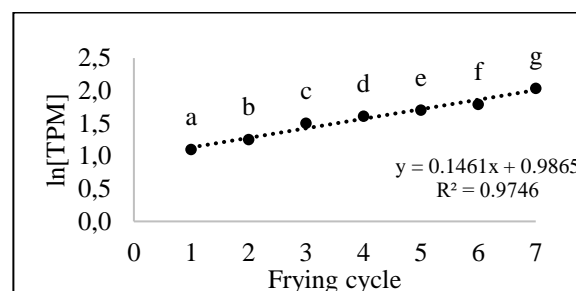
IV, a measure of degree of unsaturation of the edible oils is used to determine the oxidative stability of oils [30]. The IV of fresh oil was found to be  $95.36 \pm 0.48$  g I<sub>2</sub>/100 g (Table 2) and decreased significantly ( $p < 0.05$ ) with respect to frying cycles (Fig. 3). The decrease in IV is due to the oxidative and thermal degradation reactions which occurs during the deep frying [31]. The zero order kinetic model was found to be satisfactory in describing the change in IV (Fig. 3). IV showed positive correlation with hunter 'L' and negative correlation with frying cycles, AV, PV, TPM, hunter 'b' value, TCD (Table 3).



**Figure 3.** Change in IV with respect to frying cycles. The dotted line represents zero order fit. The standard deviation was denoted as error bars. Values with different data labels are significantly different ( $P < 0.05$ ).

#### Impact of frying cycles on TPM

TPM has been considered as one of the best indicators of the overall quality of frying oils since it represents the accurate estimation of the thermo-oxidative deterioration of frying oils by assessing the entire degraded components existing in the oil [26]. The factors which influence the formation of polar materials are fatty acid composition of oil, frying temperature, ratio of the surface oil area to oil volume in the fryer, food composition and turnover ratio [32]. The TPM of fresh CPO is 3.0 % (Table 2) and it increased significantly ( $p < 0.05$ ) with each frying cycle (Fig. 4). The increase in TPM is strongly related to the number of frying cycles and frying time [33]. The change in TPM with respect to frying cycles was best fitted using first-order kinetic model (Fig. 4). TPM showed positive correlation with frying cycles, AV, PV, Hunter 'b' value, TCD and it showed negative correlation with IV and Hunter 'L' value (Table 3).

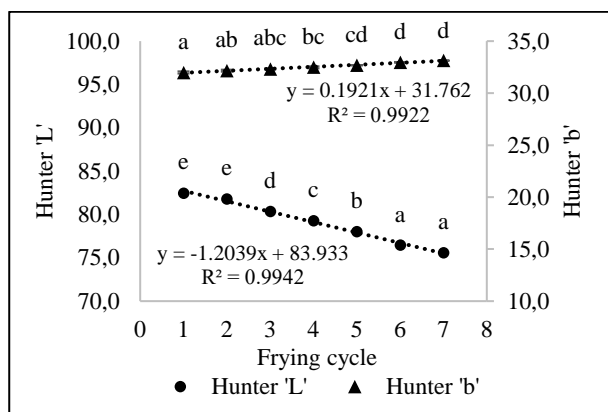


**Figure 4.** Change in TPM with respect to frying cycles on a natural log scale. The dotted line represents first order fit. The standard deviation is denoted as error bars. Values with different data labels are significantly different ( $P < 0.05$ ).

#### Impact of frying cycles on colour

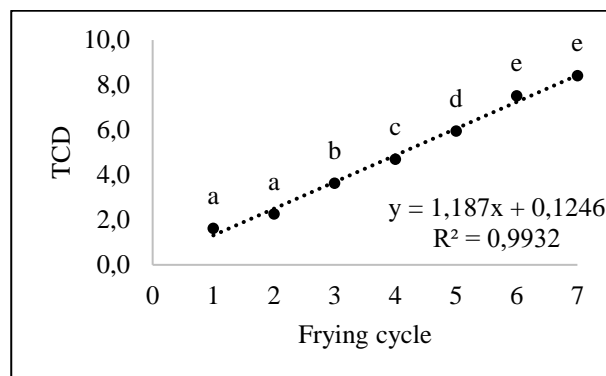
Colour is the prominent physical property of the edible oils. The colour of oils darkens during frying which mainly depends on the temperature of deep frying, time of frying and the type of food fried. Typically the colour of edible oil changes from pale yellow to light brown and then dark brown during repeated frying [16, 24]. When food is fried at high temperatures, chemical reactions such as thermal oxidation and polymerization of the unsaturated fatty acids lead to the formation of non-volatile decomposition products like polymers and non-polar compounds which contribute to the colour change [34]. The Hunter 'L' and 'b' values represent light/dark and yellow/blue colour of the sample. In the current study, the 'L' value reduced significantly ( $p < 0.05$ ) with frying cycles (Fig. 5). The change indicates darkening of the frying oil caused by oxidised products, products of Maillard reaction and chemical reactions of the oxidised products with

Maillard reaction products, charred food residues, leaching of pigments from food particles into the oil [16, 35, 36]. It has been reported that during frying of potatoes, reactions between sugar aldehyde groups and amino acids produce brown products [37]. The change of 'L' value was best fitted in zero-order kinetic model (Fig. 5). The Hunter 'b' value increased significantly ( $p < 0.05$ ) with frying cycles (Fig. 5). The increase in yellow colour might be due to the pigments present in the food particles, the colour induced from Maillard reactions, formation of the chroman-5,6-quinones by partial oxidation of vegetable oils [16, 36, 38]. The zero-order kinetic model was found to be adequate in fitting the Hunter 'b' value (Fig. 5).



**Figure 5.** Change in hunter 'L' and 'b' with respect to frying cycles. The dotted line represents zero order fit. The standard deviation is denoted as error bars. Values with different data labels are significantly different ( $P < 0.05$ ).

The TCD represents, overall, that the oil darkness increased significantly ( $p < 0.05$ ) with each frying cycle and it was best fitted in zero-order reaction kinetic model (Fig. 6). The TCD following zero-order kinetic model has also been reported [10, 16, 39].



**Figure 6.** Change in yellowness with respect to frying cycles. The dotted line represents zero order fit. The standard deviation is denoted as error bars. Values with different data labels are significantly different ( $P < 0.05$ ).

### CONCLUSION

In conclusion the current study reports the impact of frying cycles on the quality deterioration of CPO during frying of French fries. Our findings suggest that the frying cycles declined the quality of oil proven by increase in AV, PV, TPM and darkening of oil. Frying cycle showed strong correlation with the colour of the oil. Kinetic modelling showed change in AV, and TPM followed first-order kinetic model while IV, Hunter 'L', 'b' and TCD followed zero-order kinetic model. Fatty acid profile showed significant decline in unsaturated fatty acids. The marginal changes in the quality changes in CPO subjected to frying, indicated its stability as a frying medium.

**Acknowledgements:** The authors would like to acknowledge "Small molecular techniques laboratory, Anna University" for providing GC-MS analysis facility.

**Funding:** This study was funded by Centre for Research, Anna University-ACRF grant (Grant No-CRF/ACRF/17245297143-AR1).

**Conflicts of interest:** The authors have no conflicts of interest to declare.

**Table 3.** Pearson correlation of quality indices of CPO

	Frying cycles	AV	PV	IV	TPM	Hunter 'L'	Hunter 'b'	TCD
Frying cycles		0.9867	0.9583	-0.9880	0.9849	-0.9971	0.9961	0.9966
AV	0.9867		0.9388	-0.9881	0.9923	-0.9849	0.9911	0.9862
PV	0.9583	0.9388		-0.9603	0.9260	-0.9711	0.9696	0.9717
IV	-0.9880	-0.9881	-0.9603		-0.9689	0.9896	-0.9948	-0.9912
TPM	0.9849	0.9923	0.9260	-0.9689		-0.9794	0.9810	0.9793
Hunter 'L'	-0.9971	-0.9849	-0.9711	0.9896	-0.9794		-0.9971	-0.9999
Hunter 'b'	0.9961	0.9911	0.9696	-0.9948	0.9810	-0.9971		0.9977
TCD	0.9966	0.9862	0.9717	-0.9912	0.9793	-0.9999	0.9977	

AV – acid value (mg KOH/g of oil); PV – peroxide value (meqO<sub>2</sub>/kg of oil); IV – iodine value (gI<sub>2</sub>/100g); TPM – total polar materials; TCD – total colour difference.

REFERENCES

1. R. Yamsaengsung, R. G. Moreira, *J. Food Eng.*, **53**, 11 (2002).
2. G. Boskou, F. N. Salta, A. Chiou, E. Troullidou, N. K. Andrikopoulos, *Eur. J. Lipid Sci. Technol.*, **108**, 109 (2006).
3. E. Choe, D. B. Min, *J. Food Sci.*, **72**, R77 (2007).
4. N. K. Andrikopoulos, N. Kalogeropoulos, A. Falirea, M. N. Barbagianni, *Int. J. Food Sci. Technol.*, **37**, 177 (2002).
5. G. Bansal, W. Zhou, P. J. Barlow, P. S. Joshi, H. L. Lo, Y. K. Chung, *Crit. Rev. Food Sci. Nutr.*, **50**, 503 (2010).
6. S. K. Veličkowska, S. Mitrev, L. Mihajlov, *Grasas y Aceites*, **67**, (2016).
7. E. Yol, R. Ustun, M. Golukcu, B. Uzun, *J. Am. Oil Chem. Soc.*, **94**, 787 (2017).
8. R. Mora-Escobedo, P. Hernández-Luna, I. C. Joaquín-Torres, A. Ortiz-Moreno, M. del C. Robles-Ramírez, *CyTA - J. Food.*, **13**, 300 (2015).
9. A. K. Das, R. Babylatha, A. S. Pavithra, S. Khatoon, *J. Food Sci. Technol.*, **50**, 1186 (2013).
10. O. I. Mba, M.-J. Dumont, Michael Ngadi, *J. Am. Oil Chem. Soc.*, **93**, 1243 (2016).
11. F. Hindra, O. D. Baik, *Crit. Rev. Food Sci. Nutr.*, **46**, 239 (2006).
12. S. Z. Abidin, D. Patel, B. Saha, *Can. J. Chem. Eng.*, **91**, 1896 (2013).
13. N. Idun-acquah, G. Y. Obeng, E. Mensah, *Sci. Technol.*, **6**, 8 (2016).
14. R. FM Ali, *J. Food Process. Technol.*, **03**, (2012).
15. O. A. Babatunde, G. S. Bello, *IOSR J. Appl. Chem.*, **9**, 26 (2016).
16. M. Maskan, *Eur. Food Res. Technol.*, **218**, 20 (2003).
17. B. Ling, J. Tang, F. Kong, E. J. Mitcham, S. Wang, *Food Bioprocess Technol.*, **8**, 343 (2015).
18. M. A. J. S. Van Boekel, Kinetic modeling of food quality: A critical review, in: *Compr. Rev. Food Sci. Food Saf.*, John Wiley & Sons, Ltd, 2008, p. 144.
19. L. M. Bal, A. Kar, S. Satya, S. N. Naik, *Int. J. Food Sci. Technol.*, **46**, 827 (2011).
20. H. K. Sharma, B. Kaur, B. C. Sarkar, C. Singh, *Grasas y Aceites*, **57**, 376 (2006).
21. T. T. Xu, J. Li, Y. W. Fan, T. W. Zheng, Z. Y. Deng, *Int. J. Food Prop.*, **18**, 1478 (2015).
22. S. Debnath, N. K. Rastogi, A. G. Gopala Krishna, B. R. Lokesh, *Food Bioprod. Process.*, **90**, 249 (2012).
23. A. Chatzilazarou, O. Gortzi, S. Lalas, E. Zoidis, J. Tsaknis, *J. Food Lipids*, **13**, 27 (2006).
24. P. K. Nayak, U. Dash, K. Rayaguru, K. R. Krishnan, *J. Food Biochem.*, **40**, 371 (2016).
25. FAO, WHO, Standard for Named Vegetable Oils, 1999.
26. R. Sayyad, *J. Food Sci. Technol.*, **54**, 2224 (2017).
27. C. W. Fritsch, *J. Am. Oil Chem. Soc.*, **58**, 272 (1981).
28. S. Paul, G. S. Mittal, *Crit. Rev. Food Sci. Nutr.*, **37**, 635 (1997).
29. G. M. F. Aragao, M. G. Corradini, M. Peleg, *J. Am. Oil Chem. Soc.*, **85**, 1143 (2008).
30. E. Zahir, R. Saeed, M. A. Hameed, A. Yousuf, *Arab. J. Chem.*, **10**, S3870 (2017).
31. R. Mishra, H. K. Sharma, *J. Food Sci. Technol.*, **51**, 1076 (2014).
32. J. Mlcek, H. Druzvikova, P. Va Lasek, J. Sochor, T. Jurikova, M. Borkovcova, M. Baron, S. Balla, *Ital. J. Food Sci.*, **27**, 32 (2015).
33. A. M. Sharoba, M. Fawzy Ramadan, *J. Food Process. Technol.*, **3**, 161 (2012).
34. C. P. Tan, H. Mirhosseini, Y. B. C. Man, A. Serjouie, *Am. J. Food Technol.*, **5**, 310 (2010).
35. D. Goburdhun, P. Seebun, A. Ruggoo, *J. Consum. Stud. Home Econ.*, **24**, 223 (2000).
36. D. Günal-Köroğlu, S. Turan, M. Kiralan, M. F. Ramadan, *Int. Food Res. J.*, **26**, 1269 (2019).
37. J. K. Kim, H. J. Lim, D. H. Shin, E. C. Shin, *J. Korean Soc. Appl. Biol. Chem.*, **58**, 527 (2015).
38. M. Gharachorloo, M. Ghavami, M. Mahdiani, R. Azizinezhad, *J. Am. Oil Chem. Soc.*, **87**, 355 (2010).
39. D. P. Houhoula, V. Oreopoulou, C. Tzia, *J. Am. Oil Chem. Soc.*, **79**, 133 (2002).

## Study of the kinetics and mechanism of the oxidative conversion of ethyl alcohol to acetic acid over the modified natural zeolite catalyst clinoptilolite

A. M. Aliyev, A. R. Safarov\*, G. A. Ali-zadeh, F. V. Aliyev

*Institute of Catalysis and Inorganic Chemistry named after Academician M. F. Nagiyev, AZ1143, H. Javid Avenue 113, Baku, Azerbaijan*

Received: February 01, 2022; Revised: April 13, 2022

In this study, we aimed to investigate the kinetic laws of the vapor-phase oxidation of ethyl alcohol into acetic acid over natural clinoptilolite modified by ion exchange method and containing 0.25% wt.  $\text{Cu}^{2+}$ , 0.05% wt.  $\text{Mn}^{2+}$  and 0.05% wt.  $\text{Pd}^{2+}$  ions. Experimental studies were carried out in the temperature range of 180-230°C, partial pressure of  $\text{C}_2\text{H}_5\text{OH}$  – 0.05÷0.25 atm and of  $\text{O}_2$  – 0.3÷0.55 atm, space velocity of the mixture 3600-5400  $\text{h}^{-1}$ . Based on the experimental data the total kinetic scheme of the reaction mechanism, as well as kinetic stage schemes for product formation were proposed, and a theoretically grounded kinetic model of the process was developed. The numerical values for the constants of the kinetic model were calculated using the Matlab software package. The results of the studies showed that the developed kinetic model satisfactorily describes the experimental kinetic data.

**Keywords:** Ethyl alcohol, Acetic acid, Zeolites, Mechanism, Kinetic model

### INTRODUCTION

Acetic acid is one of the main products of organic synthesis and is widely used in the textile and food industries. It is also used for the synthesis of ethyl acetate.

On an industrial scale organic acids are obtained *via* heterogeneous catalytic oxidation of aliphatic alcohols. The catalysts are metals (e.g., Cu, Ag, Au, Fe, and Mo), transition metal oxides (e.g.,  $\text{CuO}+\text{Cu}_2\text{O}$ ,  $\text{V}_2\text{O}_5$ ,  $\text{Cr}_2\text{O}_3$ ,  $\text{MoO}_3$ , etc.), mixed oxides, and salts of transition metals (e.g., vanadates, tungstates, stannates, and molybdates of zinc, cobalt, and bismuth). These processes occur in the temperature range of 350-450°C and have relatively low selectivity toward the target product [1-4].

In our previous works [5-8] we showed that zeolites modified with metal cations *via* ion exchange exhibit fairly high catalytic activity and selectivity in the oxidative conversion of aliphatic alcohols at relatively low temperatures (250-350°C).

Based on a study of experimental data in the literature and on physicochemical methods of analysis, it was established that – like the liquid-phase variant of the process, which is performed in an acid medium, includes protons, and proceeds through the formation of an intermediate compound (chromate ester) – the heterogeneous vapor-phase partial oxidation of aliphatic alcohols on metal-zeolite catalysts also yields surface alkoxides that form during the interaction of medium-strength Brønsted acid sites with molecules of aliphatic alcohols adsorbed on the catalyst's surface. The heterogeneous partial oxidation of aliphatic alcohols

on the surfaces of metal-zeolite catalysts occurs as a result of the interaction between these alkoxide compounds and the surfaces' nucleophilic oxygen [9].

In [10] we have shown that natural zeolite – clinoptilolite (crystallinity 80-85%,  $\text{SiO}_2/\text{Al}_2\text{O}_3 = 8.68$ ) of the Aydag deposit of Azerbaijan modified *via* ion exchange with cations  $\text{Cu}^{2+}$ (0.25% wt.),  $\text{Mn}^{2+}$ (0.05% wt.) and  $\text{Pd}^{2+}$ (0.05% wt.) possesses high activity and selectivity in the reaction of vapor-phase oxidation of ethyl alcohol to acetic acid.

In the present paper, the results of the investigation of the kinetic laws for the vapor-phase process of oxidation of ethyl alcohol into acetic acid on the catalyst described above are given and a theoretically grounded kinetic model of the process is developed, which takes a central place in the mathematical model serving as the basis for its optimal design.

### EXPERIMENTAL

Catalysts were prepared from natural clinoptilolite (from Azerbaijan deposit) with silicate modulus  $\lambda=\text{SiO}_2/\text{Al}_2\text{O}_3 = 8.68$  and crystallinity of 80-85%. The zeolite's type and crystallinity were determined *via* X-ray diffraction on a D-2 diffractometer (Bruker). The original samples of natural zeolites were converted into the hydrogen form in two ways: decationization with 1 N  $\text{NH}_4\text{Cl}$  solution and dealumination with 0.5 N hydrochloric acid solution for 60 min at 85-90°C. By dealumina-

\*To whom all correspondence should be sent:  
E-mail: agil\_s@mail.ru

tion in a solution of 0.5 N HCl, the silicate modulus of the zeolite was adjusted to  $\lambda=10.8$ . Dealuminated samples were subjected to decationization by treatment with a solution of  $\text{NH}_4\text{Cl}$ . Then the samples were washed with distilled water until the absence of  $\text{Cl}^-$  ions, dried at a temperature of 80-120°C (3 hours), and annealed at a temperature of 400°C (4 hours) and 550°C (3 hours). Then 50 grams of a fraction with 0.25-0.63 mm grain size were taken and poured into a 1 L flask, where it was treated with a 0.1 N HCl solution at a temperature of 95-98°C 3 times for 2 hours each time, then the samples were washed, dried and thermally treated.

The zeolites were modified with  $\text{Cu}^{2+}$ ,  $\text{Mn}^{2+}$ ,  $\text{Pd}^{2+}$  metal cations *via* ion exchange in aqueous solutions of  $\text{CuCl}_2$ ,  $\text{MnCl}_2$ , and  $[\text{Pd}(\text{NH}_3)_4]\text{Cl}_2$ , respectively. Upon completion of the exchange, the catalyst was washed from  $\text{Cl}^-$  ions with distilled water, dried at a temperature of 120-150°C (3-5 hours) and thermally treated at a temperature of 350-400°C for 30 min in a stream of air at a volumetric flow rate of 2400  $\text{h}^{-1}$ .

The mixture was stirred until the complete input of ions into the composition of the zeolite. To establish the completeness of the exchange of inputted cations a qualitative analysis procedure was used. To determine the number of cations, in addition to the above analytical method, elemental analysis was performed on the ICP-MS Agilent 7700 X (method of mass spectrometry with inductively coupled plasma in elemental analysis) and X-ray phase analysis on a D-2 diffractometer (Bruker).

Experiments were performed on a flow-through unit connected directly to the DB-624 column of an Agilent 7820A gas-liquid chromatography system at a gas (He) flow rate of 1.5 mL/min. The separation of reaction products was carried out under conditions of linearly programmed rising temperature of the chromatograph thermostat with a gas carrier velocity ( $\text{N}_2$ ) – 3.6 liter per hour. Into the reactor made of Pyrex glass with an inner diameter  $d_{\text{in}}=20$  mm, with zones for preheating of the initial reaction mixture 3  $\text{cm}^3$  of the catalyst with a particle size 0.25-0.63 mm was loaded and then was activated for 2 hours in an air stream at temperature 450°C and then the temperature was lowered to the reaction temperature and the reaction mixture was supplied at a certain volumetric rate. The reactor was placed in an air electric oven with automatic temperature control. The raw material was fed with a pump. Using a ME-1600 microdoser, the initial materials were supplied to a mixer in a thermostated cabinet equipped with an electric heater and a fan. A stable temperature in the thermostat was maintained using a MICROMAX temperature microcontroller. During the tests, a certain temperature was individually set and

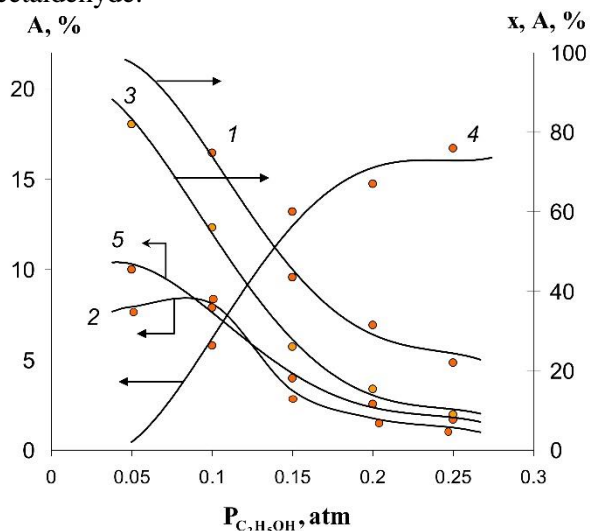
maintained for each experiment. The mixture of vapors of ethyl alcohol, together with oxygen and nitrogen was fed to one of the knees of the reactor with a catalyst bed. The temperature in the middle of the catalyst layer with granulated Pyrex (2÷3 mm) was measured with a thermocouple and recorded with a potentiometer. The composition of the reaction mixture was determined at various intervals by gas chromatography, taking samples from the reaction zone directly through a six-way crane mounted on the output of the reactor. In experiments ethyl alcohol with purity of 96% was used. The reaction products together with unreacted raw materials were fed to a cooled receiver. Runs performed at several feed rates and using granules of the catalyst with different sizes (0.3÷1.0) showed that external and internal mass transfer effects were negligible under the studied experimental conditions, so the process was carried out under conditions allowing the reaction to proceed in the kinetic range. To determine the effect of water on the process of oxidative conversion of ethyl alcohol into acetic acid, a series of additional experiments were carried out. It was established that the addition of water to ethyl alcohol does not affect the course of the reaction. During the experiments no traces of carbon monoxide were detected on the chromatograms.

The experimental studies of the kinetic laws of vapor-phase oxidation of ethyl alcohol into acetic acid were carried out in a U-shaped flow reactor directly connected to a column of a gas-liquid chromatography system in the temperature range of 180-230°C, with partial pressures of  $\text{C}_2\text{H}_5\text{OH}$  – 0.05÷0.25 atm and  $\text{O}_2$  – 0.3÷0.55 atm, and space velocity of the mixture – 3600-5400  $\text{h}^{-1}$ .

## RESULTS AND DISCUSSION

The effect of the partial pressure of ethyl alcohol on the course of the reaction was studied in the range of 0.05-0.25 atm at a temperature of 220°C, space velocity of 4800  $\text{h}^{-1}$ , and partial pressure of oxygen of 0.4 atm. Along with the main product – acetic acid, acetaldehyde, ethyl acetate, and carbon dioxide were formed in the reaction. Figure 1 shows the curves of the conversion of ethyl alcohol and the yield of reaction products as a function of the partial pressure of ethanol at 220°C. As can be seen from the figure increasing the partial pressure of alcohol from 0.05 atm to 0.25 atm leads to decreasing conversion from 97.4 to 22.2%, wherein the yield of acetic acid and carbon dioxide decreases, the yield of acetaldehyde increases, and that of ethyl acetate passes through a maximum. The change in the course of the curves can be explained as follows. At

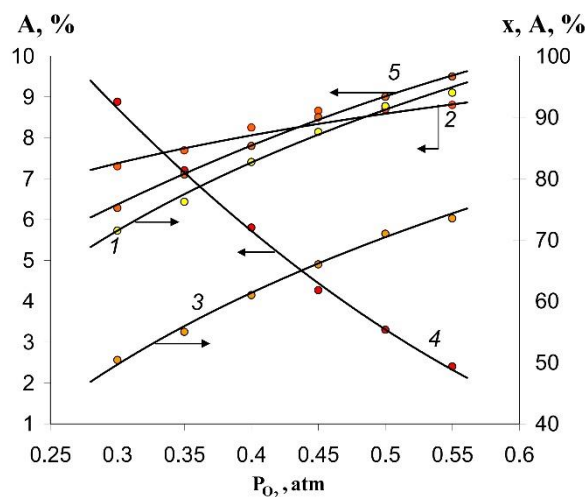
partial pressures of ethanol less than 0.1 atm, the process occurs in an excess of oxygen, which provides relatively high oxidation rates of alcohol to acetaldehyde and acetaldehyde to acetic acid, while the lack of alcohol inhibits the esterification reaction leading to the formation of ethyl acetate. The maximum yield of ethyl acetate is observed at the partial pressure of alcohol, approximately equal to 0.1 atm. Increasing the partial pressure of ethyl alcohol above 0.1 atm leads to obstruction of the coordination of oxygen on the active sites of the metal-zeolite catalyst, which reduces the conversion and yields of all reaction products except acetaldehyde.



**Fig. 1.** Effect of the partial pressure of ethyl alcohol on the course of the reaction at a temperature of 220°C, space velocity of 4800 h<sup>-1</sup>, and partial pressure of oxygen of 0.4 atm. x – conversion, A – yields of reaction products. 1 – alcohol; 2 – ethyl acetate; 3 – acetic acid; 4 – acetaldehyde; 5 – carbon dioxide.

The effect of the partial pressure of oxygen on the yield of the products of the reaction at a space velocity of 4800 h<sup>-1</sup>, partial pressure of ethyl alcohol of 0.1 atm, and temperature of 220°C is shown in Fig. 2. The partial pressure of oxygen was varied in the range of 0.3-0.55 atm. The figure shows that with increasing the partial pressure of oxygen, there is an increase in the degree of conversion of ethyl alcohol. In the entire studied range of the partial pressure of oxygen, a decrease of the yield of acetaldehyde and an increase of the yields of all other reaction products is observed.

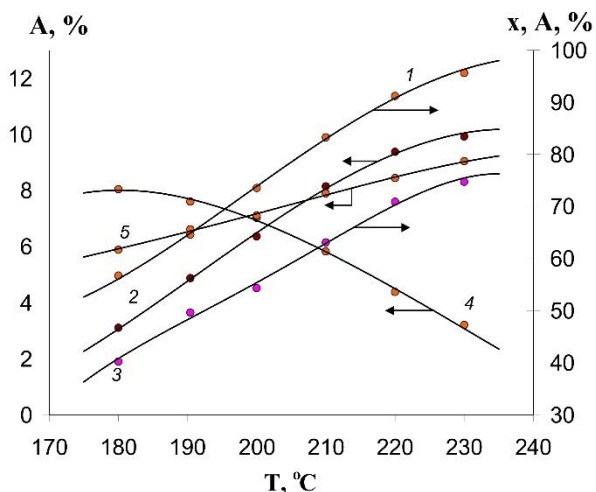
The yield of ethyl acetate is stabilized at ethanol partial pressures above 0.4 atm. The course of the curves can be explained by the sequential mechanism of the formation of acetaldehyde, acetic acid, and carbon dioxide and the sequentially parallel mechanism of the formation of ethyl acetate from ethyl alcohol and acetic acid.



**Fig. 2.** Effect of the partial pressure of oxygen on the course of the reaction at a temperature of 210°C, space velocity of 4800 h<sup>-1</sup>, and partial pressure of ethyl alcohol of 0.1 atm. x – conversion, A – yields of reaction products. 1 – alcohol; 2 – ethyl acetate; 3 – acetic acid; 4 – acetaldehyde; 5 – carbon dioxide.

The effect of temperature of the process on the activity of the catalytic system at partial pressures of ethyl alcohol – 0.1 atm, oxygen – 0.4 atm, and space velocity of 4800 h<sup>-1</sup> is shown in Figure 3. The figure shows that on increasing the temperature of the process, the degree of conversion of ethyl alcohol also increases. A sharp increase of the conversion of alcohol is observed with increasing temperature up to 210°C. The observed change in the course of the curves of the yields of reaction products depending on temperature is explained by the formation of acetic acid and carbon dioxide by the oxidation of acetaldehyde.

The effect of the space velocity on the course of the reaction was studied in the range of 3000-5400 h<sup>-1</sup> at a temperature of 220°C. Figure 4 shows the dependence of the activity of the catalyst on the space velocity at the temperature of 220°C. It follows from the figure that with increasing the space velocity, the conversion of ethyl alcohol decreases. Increasing yield of acetaldehyde and decreasing conversion of ethyl alcohol is explained by shortening of the contact time.

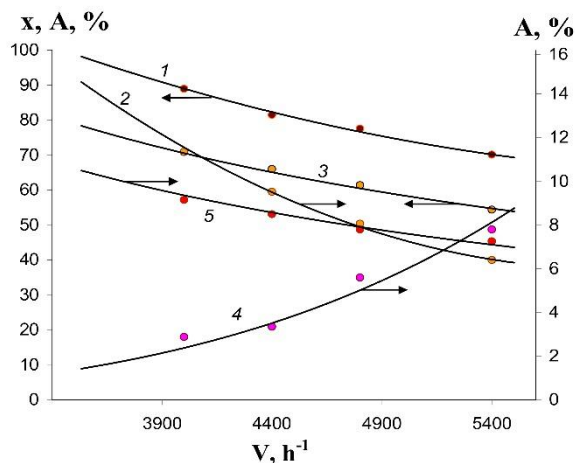
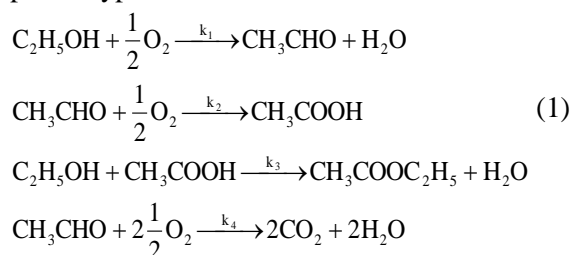


**Fig. 3.** Effect of the temperature on the course of the reaction at a space velocity of 4800 h<sup>-1</sup> and partial pressures of ethyl alcohol of 0.1 atm, and oxygen of 0.4 atm. x – conversion, A – yields of reaction products. 1 – alcohol; 2 – ethyl acetate; 3 – acetic acid; 4 – acetaldehyde; 5 – carbon dioxide.

Increasing the yield of acetaldehyde over the entire studied range of space velocities and decreasing the yields of the remaining products confirms the formation of acetic acid and carbon dioxide by the oxidation of acetaldehyde and the sequentially parallel mechanism of formation of ethyl acetate.

Based on the above analysis and literature data the following hypothesis about the reaction mechanism was proposed: acetaldehyde is formed by the interaction of adsorbed ethanol molecules with dissociatively adsorbed oxygen molecules. Acetic acid is formed by the interaction of adsorbed acetaldehyde molecules with dissociatively adsorbed oxygen molecules. Ethyl acetate is formed by the interaction of strongly adsorbed acetic acid molecules with weakly adsorbed molecules of ethyl alcohol. Carbon dioxide is formed by the interaction of adsorbed acetaldehyde molecules with oxygen molecules from the gas phase.

The following gross-stoichiometric equations for the formation of acetaldehyde, acetic acid, ethyl acetate, and carbon dioxide correspond to the proposed hypothesis:



**Fig. 4.** The effect of the influence of the space velocity on the course of the reaction at the temperature 210°C and partial pressures of ethyl alcohol of 0.1 atm and oxygen of 0.4 atm. x – conversion, A – yields of reaction products. 1 – alcohol; 2 – ethyl acetate; 3 – acetic acid; 4 – acetaldehyde; 5 – carbon dioxide.

In adsorption of the gas mixture components, the molecules of these components interact with the free surface of the catalyst according to the Langmuir scheme, wherein is assumed that molecules of the components are adsorbed on the same free sites on the surface. It is known that the sum of the occupied and free sites on the surface of the catalyst equal one, i.e.:

$$1 = Z + Z_{\text{C}_2\text{H}_5\text{OH}} + Z_{\text{O}_2} + Z_{\text{CH}_3\text{COOH}} + Z_{\text{CH}_3\text{CHO}}, \quad (2)$$

where Z – fraction of the free surface of the catalyst;  $Z_{\text{C}_2\text{H}_5\text{OH}}$ ,  $Z_{\text{O}_2}$ ,  $Z_{\text{CH}_3\text{COOH}}$ ,  $Z_{\text{CH}_3\text{CHO}}$  – fractions of surface coverage by ethyl alcohol, oxygen, acetic acid and acetaldehyde, respectively.

The calculation of surface concentrations proposed by Langmuir is based on the concepts of equality of the processes of adsorption and desorption. Adsorption equilibrium can be described by the isotherm  $\theta = f(p)_{T=\text{const}}$ , which is the basis for the mathematical description of adsorption processes. Expressing surface concentrations in terms of the fraction of the free surface of the catalyst Z and the partial pressures of the corresponding components, we obtain:

$$\begin{aligned}
 1 &= Z + b_1 P_1 Z + b_2 \sqrt{P_2} Z + b_3 P_4 Z + b_4 P_5 Z \\
 Z &= \frac{1}{1 + b_1 P_1 + b_2 \sqrt{P_2} + b_3 P_4 + b_4 P_5},
 \end{aligned} \quad (3)$$

where  $b_1$ ,  $b_2$ ,  $b_3$ ,  $b_4$  – adsorption equilibrium constants of ethyl alcohol, oxygen, acetic acid and acetaldehyde;  $P_i$  ( $i = \overline{1,8}$ ) partial pressures of ethyl alcohol –  $P_1$ , oxygen –  $P_2$ , ethyl acetate –  $P_3$ , acetic acid –  $P_4$ , acetaldehyde –  $P_5$ , carbon dioxide –  $P_6$ ,

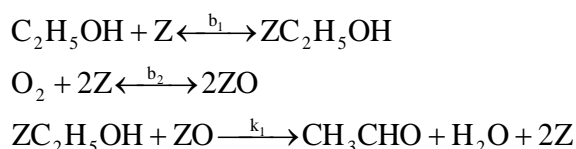
water – P<sub>7</sub>, nitrogen – P<sub>8</sub>; k<sub>i</sub> (i = 1,4) – reaction rate constants.

For convenience of calculations, marking Z<sub>C<sub>2</sub>H<sub>5</sub>OH</sub>, Z<sub>O<sub>2</sub></sub>, Z<sub>CH<sub>3</sub>COOH</sub>, Z<sub>CH<sub>3</sub>CHO</sub> over θ<sub>1</sub>, θ<sub>2</sub>, θ<sub>3</sub>, θ<sub>4</sub> and using (3), we obtain the dependences of surface concentrations through their partial pressures:

$$\begin{aligned}\theta_1 &= b_1 P_1 Z = \frac{b_1 P_1}{1 + b_1 P_1 + b_2 \sqrt{P_2} + b_3 P_4 + b_4 P_5} \\ \theta_2 &= b_2 \sqrt{P_2} Z = \frac{b_2 \sqrt{P_2}}{1 + b_1 P_1 + b_2 \sqrt{P_2} + b_3 P_4 + b_4 P_5} \\ \theta_3 &= b_3 P_4 Z = \frac{b_3 P_4}{1 + b_1 P_1 + b_2 \sqrt{P_2} + b_3 P_4 + b_4 P_5} \\ \theta_4 &= b_4 P_5 Z = \frac{b_4 P_5}{1 + b_1 P_1 + b_2 \sqrt{P_2} + b_3 P_4 + b_4 P_5}\end{aligned}\quad (4)$$

Kinetic staged schemes for the formation of reaction products can be presented as follows:

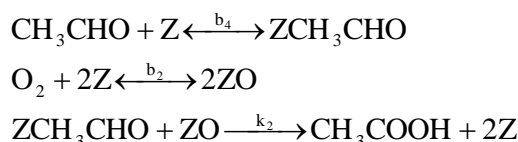
For acetaldehyde:



The rate of formation of acetaldehyde, according to this scheme takes the form:

$$r_1 = k_1 \theta_1 \theta_2 \quad (5)$$

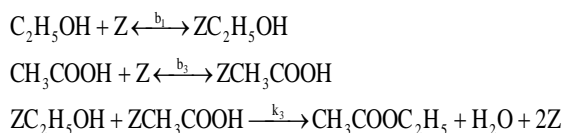
For acetic acid:



The rate of formation of acetic acid, according to this scheme takes the form:

$$r_2 = k_2 \theta_4 \theta_2 \quad (6)$$

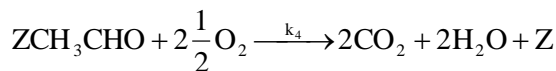
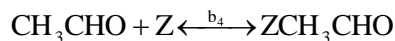
For ethyl acetate:



The kinetic equation corresponding to this scheme can take the form:

$$r_3 = k_3 \theta_1 \theta_3 \quad (7)$$

For carbon dioxide:



The kinetic equation corresponding to this scheme takes the form:

$$r_4 = k_4 \theta_4 P_2 \quad (8)$$

Expressing the rate of formation of each component through the rates of the stages in which this component is involved and taking into account the corresponding stoichiometric coefficients, we obtain:

$$\left\{\begin{aligned}\frac{dn_1}{dG_{kat}} &= -r_1 - r_3 \\ \frac{dn_2}{dG_{kat}} &= -\frac{1}{2}r_1 - \frac{1}{2}r_2 - \frac{5}{2}r_4 \\ \frac{dn_3}{dG_{kat}} &= r_3 \\ \frac{dn_4}{dG_{kat}} &= r_2 - r_3 \\ \frac{dn_5}{dG_{kat}} &= r_1 - r_2 - r_4 \\ \frac{dn_6}{dG_{kat}} &= 2r_4 \\ \frac{dn_7}{dG_{kat}} &= r_1 + r_3 + 2r_4 \\ \frac{dn_8}{dG_{kat}} &= 0,\end{aligned}\right. \quad (9)$$

where n<sub>1</sub> – ethyl alcohol, mol/h; n<sub>2</sub> – oxygen, mol/h; n<sub>3</sub> – ethyl acetate, mol/h; n<sub>4</sub> – acetic acid, mol/h; n<sub>5</sub> – acetaldehyde, mol/h; n<sub>6</sub> – carbon dioxide, mol/h; n<sub>7</sub> – water, mol/h; n<sub>8</sub> – nitrogen, mol/h.

This system of differential equations takes into account the changes of all components of the process. Such a system is quite difficult for solving. Therefore, we transform it. We select the following substances as the key components (linearly independent components): ethyl acetate (n<sub>3</sub>); acetic acid (n<sub>4</sub>); acetaldehyde (n<sub>5</sub>); carbon dioxide (n<sub>6</sub>). The remaining components will be expressed through these key components. Thus, after some mathematical transformations, as well as expressing the ratio of the current amount of the component to the initial amount of ethyl alcohol through the dimensionless quantity A, i.e.: A<sub>i</sub> = n<sub>i</sub>/N<sub>1</sub><sup>0</sup>, i = 3, 4, 5, 6, we obtain the following kinetic model of the process:



$$\left\{ \begin{aligned} \frac{dA_1}{d\left(\frac{G_{kat}}{N_1^0}\right)} &= \frac{k_3 b_1 b_3 P_1 P_4}{\left(1 + b_1 P_1 + b_2 \sqrt{P_2} + b_3 P_4 + b_4 P_5\right)^2} \\ \frac{dA_2}{d\left(\frac{G_{kat}}{N_1^0}\right)} &= \frac{k_2 b_2 \sqrt{P_2} b_4 P_5 - k_3 b_1 b_3 P_1 P_4}{\left(1 + b_1 P_1 + b_2 \sqrt{P_2} + b_3 P_4 + b_4 P_5\right)^2} \\ \frac{dA_3}{d\left(\frac{G_{kat}}{N_1^0}\right)} &= \frac{k_1 b_1 b_2 P_1 \sqrt{P_2} - k_2 b_2 \sqrt{P_2} b_4 P_5 - k_4 P_2 b_4 P_5 \left(1 + b_1 P_1 + b_2 \sqrt{P_2} + b_3 P_4 + b_4 P_5\right)}{\left(1 + b_1 P_1 + b_2 \sqrt{P_2} + b_3 P_4 + b_4 P_5\right)^2} \\ \frac{dA_4}{d\left(\frac{G_{kat}}{N_1^0}\right)} &= \frac{2k_4 b_4 P_5 P_2}{1 + b_1 P_1 + b_2 \sqrt{P_2} + b_3 P_4 + b_4 P_5}, \end{aligned} \right. \quad (10)$$

where  $k_i = \exp(\ln k_{0i} - E_i/RT)$ ,  
 $b_i = \exp(\ln K_{0i} + Q_i/RT)$ , ( $i = \overline{1,4}$ );  $A_i$  ( $i = \overline{1,4}$ ) – yields of ethyl acetate, acetic acid, acetaldehyde and carbon dioxide, respectively;  $T$  – reactor temperature, °C;  $G_{kat}$  – catalyst mass, kg;  $Q_i$  – heat of adsorption of the  $i$ -th component.

Using the gross-stoichiometric equations (1), yields of reaction products and initial molar amounts of input reagents have determined the current molar amounts of all components in the stream. So, the conversion of ethyl alcohol is determined by the following expression:

$$X = 2A_1 + A_2 + A_3 + 0.5A_4 \quad (11)$$

The current number of moles of all components was determined by the following balance equations:

$$\begin{aligned} n_1 &= N_1^0 (1 - X) \\ n_2 &= N_2^0 - N_1^0 (A_1 + A_2 + 0.5A_3 + 1.5A_4) \\ n_3 &= N_1^0 A_1 \\ n_4 &= N_1^0 A_2 \\ n_5 &= N_1^0 A_3 \\ n_6 &= N_1^0 A_4 \\ n_7 &= 2n_3 + n_4 + n_5 + 1.5n_6 \\ n_8 &= N_8^0, \end{aligned}$$

where  $N_1^0, N_2^0, N_8^0$  – input reagents of ethyl alcohol, oxygen, nitrogen, respectively, mol/h.

The partial pressures of the components are determined as follows:

$$P_i = \frac{n_i}{\sum_{i=1}^8 n_i} P, \quad (12)$$

where  $P$  – total pressure of the system ( $P=1$  atm).

The results of the experimental study of the kinetic laws of this process are shown in Table 1.

Calculations of pre-exponential factors of the reaction constants ( $\ln k_{0i}, \ln K_{0i}$ ), activation energies ( $E_i$ ), and heats of adsorption ( $Q_i$ ) were performed on the Matlab software package [11] by using the simplex search method of Nelder-Mead [12], wherein the objective function has the form:

$$F = \min \sum_{i=1}^m \sum_{j=1}^n \left( \frac{|A_{ij}^{\exp} - A_{ij}^{\text{calc}}|}{A_{ij}^{\exp}} \right) \rightarrow \min, \quad (13)$$

where  $A_{ij}^{\exp}, A_{ij}^{\text{calc}}$  – experimental and calculated values of yields for the  $j$ -th component in the  $i$ -th experiment;  $m$  is the number of experiments;  $n$  is the number of components. The values of the found parameters of the kinetic model are shown in Table 2. The average relative error of the experimental and calculated values of the yields of the reaction products did not exceed 5-6%. All graphs in Figures (1-4) confirm the closeness of the experimental and calculated values. Here, the dots indicate the experimental data, and the solid lines are the results calculated from the kinetic model.

**Table 1.** Experimental kinetic data.

№	T, °C	V, hour <sup>-1</sup>	Molar ratio of reagents C <sub>2</sub> H <sub>5</sub> OH:O <sub>2</sub> :N <sub>2</sub>	Conversion of alcohol, X, %	A <sub>1</sub> , % Ethyl acetate	A <sub>2</sub> , % Acetic acid	A <sub>3</sub> , % Acetaldehyde	A <sub>4</sub> , % Carbon dioxide
1	190	4200	1:4:5	63.5	2.2	44.5	9.5	9.1
2	200	4200	1:4:5	77.6	3.0	55.4	8.1	11.1
3	210	4200	1:4:5	92.0	4.4	71.1	4.0	12.5
4	220	4200	1:4:5	96.2	5.0	76.1	0.3	14.8
5	220	6600	1:4:5	76.1	2.1	50.8	13.1	10.1
6	220	6000	1:4:5	80.0	2.8	56.2	9.3	11.7
7	220	5400	1:4:5	90.5	3.6	67.3	6.3	13.3
8	220	4800	1:4:5	98.4	4.7	77.2	1.7	14.8
9	220	3600	1:4:5	92.6	5.0	70.3	0.3	17.0
10	220	3000	1:4:5	98.4	4.9	77.7	0.3	15.5
11	220	4800	1:5.5:3.5	93.4	4.0	72.2	0.3	16.9
12	220	4800	1:5:4	98.0	3.6	77.0	0.3	17.1
13	220	4800	1:4.5:4.5	99.1	5.4	81.4	0.3	12.0
14	220	4800	1:3.5:5.5	91.4	4.9	68.8	4.2	13.5
15	220	4800	1:3:6	87.3	4.1	64.3	6.3	12.6
16	220	4800	0.5:4.5:5	97.6	2.1	78.5	0.3	16.7
17	220	4800	1.5:4.5:4	60.0	1.9	32.7	17.1	8.3
18	220	4800	2:4.5:3.5	50.8	1.1	24.6	19.7	5.4
19	220	4800	2.5:4.5:3	40.4	0.9	15.5	21.0	3.0
20	230	4200	1:4:5	91.0	4.2	70.6	0.2	16.0
21	240	4200	1:4:5	97.5	4.0	77.0	0.2	16.3

**Table 2.** Values of the constants of the kinetic model.

lnk <sub>0i</sub> (lnK <sub>0i</sub> )		E <sub>i</sub> (Q <sub>i</sub> ), kcal/mol	
lnk <sub>01</sub>	19.12	E <sub>1</sub>	17.61
lnk <sub>02</sub>	10.77	E <sub>2</sub>	12.15
lnk <sub>03</sub>	12.05	E <sub>3</sub>	12.85
lnk <sub>04</sub>	9.79	E <sub>4</sub>	13.27
lnK <sub>01</sub>	4.1	Q <sub>1</sub>	1.2
lnK <sub>02</sub>	-4.5	Q <sub>2</sub>	7.5
lnK <sub>03</sub>	2.79	Q <sub>3</sub>	2.5
lnK <sub>04</sub>	5.61	Q <sub>4</sub>	3.25

### CONCLUSION

Based on natural clinoptilolite (from Azerbaijan deposit) with silicate modulus  $\lambda = \text{SiO}_2/\text{Al}_2\text{O}_3 = 8.68$  and crystallinity of 80-85%, a high-efficiency catalyst for the reaction of vapor-phase oxidation of ethyl alcohol to acetic acid – clinoptilolite Cu<sup>2+</sup>(0.25% wt.) Mn<sup>2+</sup>(0.05% wt.) Pd<sup>2+</sup>(0.05% wt.) was synthesized *via* ion exchange. The kinetic laws of vapor-phase oxidation of ethyl alcohol to acetic acid over this catalyst were studied. Based on the study of experimental data in the literature and the results of physicochemical methods of analysis, a probable stepwise mechanism and a theoretically

grounded kinetic model of the process was proposed.

### REFERENCES

1. S. M. Brailovskii, O. N. Temkin, I. V. Trofimova, *Problemy Kinetiki i Kataliza*, **19**, 146 (1985) (in Russian).
2. T. V. Lazareva, N. A. Osipova, L. N. Kurina. *Izvestiya Vysshikh Uchebnykh Zavedenii. Khimiya i Khimicheskaya Tekhnologiya*, **33** (4), 49 (1990) (in Russian).
3. L. N. Kurina, A. A. Davudov, N. A. Osipova, in: Proceedings of the 5th International Symposium on Relations between Homogenous and Heterogenous Catalysis, Novosibirsk, 1986, p. 140.
4. G. S. Wong, D. D. Kragten, J. M. Vohs, *J. Phys. Chem. B*, **105** (7), 1366 (2001).
5. T. N. Shakhtakhtinsky, A. M. Aliyev, A. R. Kuliyeu, S. M. Medjidova, M. X. Muradov, *Dokladi AN Rossii*, **343** (4), 496 (1995) (in Russian).
6. A. M. Aliev, M. F. Bakhmanov, F. A. Agaev, V. Sh. Agaev, Z. A. Shabanova, A. R. Safarov, *Russian Journal of Physical Chemistry*, **92**(4), 656 (2018).
7. T. N. Shakhtakhtinskii, A. M. Aliev, A. R. Kuliev, S. M. Medzhidova, K. I. Matiev, M. Kh. Muradov, A. Yu. Kasumzade, *Kinetics and Catalysis*, **37**(2), 267 (1996), ([https://www.pleiades.online/contents/kincat/kincat2\\_96v37cont.htm](https://www.pleiades.online/contents/kincat/kincat2_96v37cont.htm)).
8. A. M. Aliyev, S. M. Mejidova, G. A. Ali-zade, R. Yu. Agayeva, *Azerbaijan Chemical Journal*, **1**, 9 (2013).

- (<https://akj.az/uploads/journal/az/19121491455309.pdf>)
9. A. M. Aliyev, Z. A. Shabanova, F. V. Aliyev, *European Applied Sciences*, **5**, 67 (2015).
10. T. N. Shakhtakhtinsky, A. M. Aliyev, A. R. Kuliyeu, F. A. Mamedov, SU Patent # 1549945 A1, 1985, (<https://patents.su/3-1549945-sposob-polucheniya-uksusnoj-kisloty.html>).
11. Y. K. Yeo, *Chemical engineering computation with Matlab*, Taylor & Francis, CRC Press, 2017.
12. J. C. Lagarias, J. A. Reeds, M. H. Wright, P. E. Wright, *SIAM Journal of Optimization*, **9**, 112 (1998).

## Efficient palladium *N*-heterocyclic carbene catalytic system for the synthesis of cinnamic acid and derivatives in water

M. B. Ibrahim\*, S. A. Rufa'i, H. U. Yaqub, U. B. Suleiman

Department of Pure and Industrial Chemistry, Bayero University, Kano, Nigeria

Received: March 02, 2022; Revised: April 04, 2022

Imidazolium salts (**1a** and **1b**) were synthesized by alkylation of *N*-methyl imidazole with benzyl bromide and isopropyl bromide, respectively. The reaction of the imidazolium salts (**1a** and **1b**) with palladium bromide in 3-methylpyridine afforded the corresponding palladium-*N*-heterocyclic carbene pyridine (Pd-NHC-Py) complexes (**2a** and **2b**) in good yields. The synthesized compounds were characterized using <sup>1</sup>H NMR and FT-IR spectroscopic techniques. Elemental compositions of the synthesized compounds were established using C, H, N elemental analyses. The complexes (**2a** and **2b**) were used as catalysts to develop a convenient system for the synthesis of cinnamic acid and derivatives from the coupling reaction of aryl halides with methyl acrylates, acrylic acids, and acrylamides using water as solvent. Various substituted cinnamic acids were obtained in excellent yields (84 – 97%). Moreover, the pre-catalysts were effective in the synthesis of cinnamates. A reaction mechanism based on the formation of active Pd(0) species and the *in-situ* generation of acrylic ions is proposed.

**Keywords:** Green chemistry; Mizoroki-Heck; imidazolium salts; organometallics; reaction mechanism

### INTRODUCTION

For decades, cinnamic acid has been used as a component of scents and flavorings [1]. cinnamates and cinnamides have shown promising anticancer and antituberculosis activities [2, 3]. Classical synthesis of these valuable materials suffers from many limitations, such as a multistep procedure which is associated with side reactions resulting in poor yield of the product; the use of acyl intermediates which are toxic and costly [4]. A mild and straightforward alternative for the synthesis of this important class of compounds is the palladium-catalyzed coupling reaction. Palladium catalysts have been reported to work effectively under mild conditions with a high reaction rate, excellent product yield, high functional group tolerance, and outstanding turnover number [5-9].

In parallel, the Heck reaction is recognized as the most powerful and widely used tool for the preparation of substituted alkenes from organic moieties bearing an appropriate leaving group. It is employed in the synthesis of quite a lot of intermediates for the fine chemical and pharmaceutical industries [6, 8-13].

Until recently, the Heck reaction and most organic transformations employing organometallic catalysts were predominantly carried out in a rigorously dried organic solvent. This is because water is considered the “natural enemy” of organometallic compounds [14]. Nevertheless, the

growing concern about environmental safety and protection leads to increased interest in developing a greener alternative to the use of organic solvents. Studies in this area have uncovered cleaner and relatively benign chemical processes that avoid or minimize the use of traditional organic solvents. Among the remarkable discoveries were the solventless (neat) reactions [15], reactions in inorganic solvents such as ionic liquids and per-fluorinated liquids [16], reactions in supercritical carbon dioxide [17], and reactions in aqueous media [18].

Water is the most abundant solvent on earth. It is easily accessible, inexpensive, non-flammable, and of course, harmless to the environment and the living system. Without any doubt, water is the natural solvent for biochemical transformations in the living systems because a large number of such reactions occur in this medium. Over the past few decades there has been growing interest in developing organic synthesis in water and tremendous progress has been made. The acceleration of pericyclic reactions in water discovered by Breslow [19, 20], and the “click” reactions [14] are a few examples.

In our continued effort to uncover green, mild and easy protocols for Heck and other coupling reactions [6, 8, 9, 13, 21], we wish to report the synthesis of new palladium *N*-heterocyclic carbene pyridine complexes (Pd-NHC-Py) and a method for their application in the production of cinnamic acids and derivatives in water.

\* To whom all correspondence should be sent:  
E-mail: mansurbi.chm@buk.edu.ng

## EXPERIMENTAL

### Materials

Starting material for the synthesis of the pre-carbenes and their palladium complexes were purchased from Sigma-Aldrich and used as received. Materials for the coupling reactions were of high purity and were also purchased from Sigma Aldrich. For reactions that require anhydrous conditions, the solvents were distilled and were kept under molecular sieves until when they are required. Distilled-deionized water was used for reactions in water. Purification of the products was carried out by flash column chromatography with silica gel 60 – 120 mesh LOBA Chemie AG (India). Thin-layer chromatography (TLC) analyses were performed on silica gel Merck 60 F<sub>254</sub> plates.

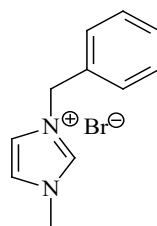
### Instrumentation

NMR spectral analyses were carried out at the Chemistry Department, King Fahd University of Petroleum and Minerals, Dhahran, Saudi Arabia. The samples were dissolved in CDCl<sub>3</sub> solvent and the spectra were recorded using either Bruker 400MHz ultra shield instrument or 500 MHz NMR machine (Joel 1500 model). Chemical shifts ( $\delta$ ) were recorded in ppm using tetramethylsilane (TMS) as reference. Coupling constants (*J*) were given in Hertz (Hz). <sup>1</sup>H NMR signals were labeled as singlet (*s*), doublet (*d*), triplet (*t*), and multiplet (*m*). An Agilent technology FT-IR spectrometer was used for recording the FT-IR spectra of the synthesized compounds in wavenumbers (cm<sup>-1</sup>). The samples were analyzed neat, either as solids or liquids. Elemental analyses were performed with a Perkin Elmer Series 11 (CHNS/O) Analyzer 2400.

### Procedure for the synthesis of *N*, *N*-dialkylated imidazolium salts (pre-carbenes) (**1a** and **1b**)

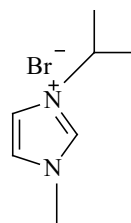
Under nitrogen atmosphere, *N*-methyl imidazole (or its derivative) (12.50 mmol), alkyl bromide (13.00 mmol, 1.54 mL) and THF (10 mL) were measured and transferred into a 25 mL two-necked round-bottom flask. A condenser was attached and the mixture was refluxed with magnetic stirring for 6 h. After completion of the reaction, the mixture was cooled to room temperature to obtain the crude product. The mixture was allowed to settle and the solvent was decanted. The product was washed several times with THF. The isolated product was then subjected to characterization using analytical and spectroscopic techniques [22, 23].

### 1-Benzyl-3-methyl imidazolium bromide (**1a**)



Yellow oil, 77% yield, <sup>1</sup>H NMR (500 MHz, CDCl<sub>3</sub>)  $\delta$  (ppm) 3.92 (*s*, 3H, NCH<sub>3</sub>) 5.66 (*s*, 2H, NCH<sub>2</sub>C), 7.00-7.60 (*m*, 7H, Ar-H), 10.44 (*s*, 1H, NCHN), <sup>13</sup>C NMR  $\delta$  (ppm): (100 MHz, CDCl<sub>3</sub>) 34.96 (NCH<sub>3</sub>), 53.29 (NCH<sub>2</sub>), 118.73 (*CH*), 124.51 (*CH*), 129.16 (*CH*), 129.21 (*CH*), 129.26 (*CH*), 130.50 (C), 132.98 (*CHN*), 135.65 (NCHC), 137.71 (NCHN) FT-IR (Neat) ( $\nu$  cm<sup>-1</sup>); 1626.77, 1458.68, 1160.44, 2854.91, 724.28. Anal. Calcd.: for C<sub>11</sub>H<sub>13</sub>BrN<sub>2</sub> C, 52.38; H, 4.76, N, 11.11, Found: C, 52.44; H, 5.02; N, 11.12.

### 1-Isopropyl-3-methyl imidazolium bromide (**1b**)

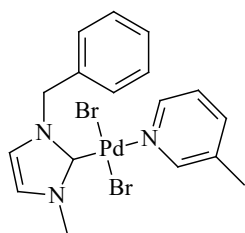


Runny brown oil, 68 % yield, <sup>1</sup>H NMR (500MHz, CDCl<sub>3</sub>)  $\delta$  (ppm): 1.04 (*d*, *J* = 6.56 Hz, 6H CH(CH<sub>3</sub>)<sub>2</sub>), 4.04 (*s*, 3H NCH<sub>3</sub>), 4.25-4.24 (*m*, 1H, NCH), 7.72 – 7.31 (*m*, 1H NCHC<sub>x2</sub>), 10.38 (*s*, 1H NCHN); <sup>13</sup>C NMR  $\delta$  (ppm): (125 MHz, CDCl<sub>3</sub>) 19.45 (CHCH<sub>3</sub>), 19.51(CHCH<sub>3</sub>), 35.15 (NCH<sub>3</sub>), 58.83 (NCH), 119.63 (CCHN), 130.54 (NCHC), 137.29 (NCHN); FT-IR (Neat) ( $\nu$  cm<sup>-1</sup>); 1629.85, 1462.72, C–N 1167.41, 2959.70, 2933.73, 2869.80. Anal. Calcd. (C<sub>7</sub>H<sub>13</sub>N<sub>2</sub>Br): C, 40.97; H, 6.34; N, 13.65. Found: C, 41.00; H, 6.51; N 13.69.

### Procedure for the synthesis of Pd-NHC-Py complexes (the pre-catalysts) (**2a** and **2b**)

A cleaned and oven-dried 25 mL round-bottom flask, purged with nitrogen gas, was charged with the NHC ligand precursor (**1a** or **1b**; 0.939 mmol), palladium bromide (0.939 mmol, 0.25 g), potassium carbonate (2.00 mmol, 0.28 g) and 5 mL of 3-methylpyridine. The mixture was purged with nitrogen for about 15 min. The reaction flask was covered with a septum and stirred at 90 °C for 24 h. At the completion of the reaction, the crude product was cooled to room temperature and transferred to an open beaker. The mixture was kept under fume hood until all the pyridine was removed. The product was dissolved in dichloromethane and the solution was passed through a microcolumn packed with silica gel. The eluent was dried to obtain yellow crystals which were further purified by recrystallization from dichloromethane and *n*-hexane. The crystals were finally washed several times with diethyl ether [22, 23].

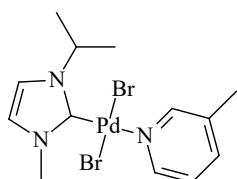
**Dibromido(1-benzyl-3-methylimidazol-2-ylidene)3-methylpyridinepalladium(II) (2a)**



Yellow crystals, 81% yield, <sup>1</sup>H NMR (400 MHz, CDCl<sub>3</sub>) δ (ppm): 2.36 (s, 3H, NCH<sub>3</sub>), 4.14 (s, 3H, Ar-CH<sub>3</sub>), 6.90 (s, 2H, NCH<sub>2</sub>C), 7.21-7.57 (m, 9H, Ar-H), 8.82 (t, J = 6.4 Hz,

2H, NCHC\*2), FT-IR (Neat) (ν cm<sup>-1</sup>); C-H SP<sup>3</sup> 2851.73, C=C aromatic 1406.71, NHC-Pd 2344.85; Anal. Calcd. for C<sub>17</sub>H<sub>20</sub>Br<sub>2</sub>N<sub>3</sub>Pd: C, 38.38; H, 3.58; N, 7.90. Found: C, 38.64; H, 3.56; N, 7.67.

**Dibromido[(1-isopropyl-3-methylimidazole-2-ylidene)(3-methylpyridine)palladium (II)] (2b)**



Yellow crystals, 62 % yield, <sup>1</sup>H NMR (500MHz, CDCl<sub>3</sub>) δ (ppm): 1.061-1.043 (d, 6H CHCH<sub>3</sub>), 2.371 (s, 3H Py-CH<sub>3</sub>), 4.200-4.112 (t, 3H NCH<sub>3</sub>),

4.579-4.511 (t, 1H NCH), 7.571-7.237 (m, 4H, Ar-H), 8.837 (s, 2H NCHC) FT-IR (Neat) (ν cm<sup>-1</sup>); C=C aromatic 1424.51, C=C aromatic 1462.50, NHC-Pd 2344.80, C-H aliphatic 2955.63, C-H aliphatic 2925.59, CH<sub>3</sub> stretching 2858.66. Anal. Calcd. for (C<sub>13</sub>H<sub>19</sub>N<sub>3</sub>PdBr<sub>2</sub>): C (32.28), H (3.93), N (8.69). Found: C (32.00), H (4.32), N (8.51).

**Procedure for the Mizoroki-Heck cross-coupling reaction**

A modification of a published procedure was used [11]. Pd-NHC-Py complex (**2a** or **2b**; 0.005 mmol), aryl halide (1.0 mmol), alkene (1.5 mmol), base (2.0 mmol) and solvent (4.0 mL) were introduced into a 25 mL round-bottom flask. A condenser was attached and the mixture was stirred at the required temperature for the required time. Progress of the reaction was monitored using TLC until no free aryl halide was observed. The reaction was stopped and cooled down to room temperature. In the case of the reaction involving water as solvent, the crude product was acidified using 5 mL of 1M HCl prior to the extraction. The product was then extracted three times with 10 mL of ethyl acetate. The combined ethyl acetate extracts were dried with anhydrous magnesium sulfate. The solvent was removed in a rotary evaporator to afford the corresponding internal alkenes. The alkene was then analyzed with TLC before further purification. The characterization data of the product were found to agree with the reported literature [6, 21].

**(E)-Cinnamic acid (5a)**

White solid, 96 % yield; <sup>1</sup>H NMR (500 MHz, CDCl<sub>3</sub>) δ (ppm): 7.78 (d, J = 15.9 Hz, 1H, CH), 7.65 – 7.45 (m, 2H, CH arom.), 7.40 – 7.37 (m, 3H, CH arom), 6.44 (d, J = 15.9 Hz, 1H, CH). <sup>13</sup>C NMR (125 MHz, CDCl<sub>3</sub>) δ (ppm): 172.3, 147.03, 134.01, 130.72, 128.94, 128.35, 117.28; GC-MS m/z 148 (M<sup>+</sup>).

**(E)-Methyl cinnamate (5h)**

White solid, 89% yield; <sup>1</sup>H NMR (500 MHz, CDCl<sub>3</sub>) δ (ppm): 7.68 (d, J = 15.9 Hz, 1H, CH), 7.51 – 7.49 (m, 2H, CH arom.), 7.38 – 7.35 (m, 3H, CH arom), 6.43 (d, J = 16.2 Hz, 1H, CH), 3.79 (s, 3H, CH<sub>3</sub>). <sup>13</sup>C NMR (125 MHz, CDCl<sub>3</sub>) δ (ppm): 167.4, 144.8, 134.4, 130.3, 129.5, 129.1, 128.9, 117.8, 51.7; GC-MS m/z 162 (M<sup>+</sup>).

**(E)-Methyl 3-(4-methoxyphenyl)acrylate (5i)**

White solid, 76 % yield; <sup>1</sup>H NMR (500 MHz, CDCl<sub>3</sub>) δ (ppm): 7.63 (d, J = 15.9 Hz, 1H, CH), 7.44 (d, J = 5.8 Hz, 2H, CH arom), 6.87 (d, J = 5.8 Hz, 2H, CH arom), 6.29 (d, J = 15.9 Hz, 1H, CH), 3.79 (s, 3H, CH<sub>3</sub>), 3.77 (s, 3H, CH<sub>3</sub>). <sup>13</sup>C NMR (125 MHz, CDCl<sub>3</sub>) δ (ppm): 167.6, 161.2, 144.3, 129.6, 126.9, 115.1, 114.1, 55.1, 51.4; GC-MS m/z 192 (M<sup>+</sup>).

**(E)-Methyl 3-(4-aminophenyl)acrylate (5j)**

Yellow solid; 70 % yield; <sup>1</sup>H NMR (500 MHz, CDCl<sub>3</sub>) δ (ppm): 7.60 (d, J = 15.8 Hz, 1H, CH), 7.32 (d, J = 5.8 Hz, 2H, CH arom), 6.60 (d, J = 8.6 Hz, 2H, CH arom), 6.19 (d, J = 15.8 Hz, 1H, CH), 3.98 (s, 2H, NH<sub>2</sub>), 3.76 (s, 3H, CH<sub>3</sub>); <sup>13</sup>C NMR (125 MHz, CDCl<sub>3</sub>) δ (ppm): 168.0 (C), 148.9, 145.2, 129.7, 124.3, 114.6 (CH), 113.0 (CH), 51.2 (CH<sub>3</sub>); GC-MS m/z 197 (M<sup>+</sup>).

**(E)-Methyl 3-(4-acetylphenyl)acrylate (5k)**

White solid; 95 % yield; <sup>1</sup>H NMR (500 MHz, CDCl<sub>3</sub>) δ (ppm): 7.90 (d, J = 6.5 Hz, 2H, CH arom), 7.65 (d, J = 16.0 Hz, 1H, CH), 7.55 (d, J = 6.6 Hz, 2H, CH arom), 6.47 (d, J = 16.0 Hz, 1H, CH), 3.77 (s, 3H, CH<sub>3</sub>), 2.57 (s, 3H, CH<sub>3</sub>); <sup>13</sup>C NMR (125 MHz, CDCl<sub>3</sub>) δ (ppm): 197.0 (C), 166.7 (C), 143.2 (CH), 138.6 (C), 138.0 (C), 128.7 (CH), 128.1 (CH), 120.2 (CH), 51.2(CH<sub>3</sub>), 26.7 (CH<sub>3</sub>); GC-MS m/z 205 (M+1).

**(E)-Methyl 3-(4-nitrophenyl)acrylate (5l)**

Yellow solid; <sup>1</sup>H NMR (500 MHz, CDCl<sub>3</sub>) δ (ppm): 8.23 (d, J = 8.8 Hz, 2H, CH arom), 7.69-7.62 (m, 3H), 6.52 (d, J = 16.1 Hz, 1H, CH), 3.80 (s, 3H, CH<sub>3</sub>); <sup>13</sup>C NMR (125 MHz, CDCl<sub>3</sub>) δ (ppm): 166.5 (C), 148.6, 141.7, 140.3, 128.5, 124.0, 122.0, 52.0 (CH<sub>3</sub>); GC-MS m/z 207 (M<sup>+</sup>).

## RESULTS AND DISCUSSION

### *Synthesis of imidazolium bromides (1a and 1b)*

The pre-carbenes (imidazolium bromides **1a** and **1b**) were prepared in good yields by the direct alkylation of the 1-methyl imidazole with benzyl bromide (Scheme 1). Formation of the imidazolium bromides was confirmed by the appearance of downfield singlet peaks at 10.44 ppm (**1a**) and 10.38 ppm (**1b**) in the proton NMR spectra, which were assigned to the acidic C-2 protons of the imidazole rings [13, 23-25]. These peaks would not be observed in the spectrum of 1-methyl imidazole. Furthermore, the benzylic protons in **1a** were observed as a single peak ( $\delta = 5.66$  ppm) whereas the isopropyl 1H in **1b** was observed as multiplet ( $\delta = 4.25 - 4.24$  ppm) in their respective proton NMR spectrum. This indicates successful alkylation of 1-methyl imidazole. All the remaining signals observed in the 1H and 13C NMR spectra of both **1a** and **1b**, as well as the functional groups identified from their respective FT-IR spectra were in total agreement with the proposed structures.

### *Synthesis of Pd(II)-NHC-Py complexes (2a and 2b) (pre-catalysts)*

The dibromido palladium(II) pyridine (Pd-NHC-Py) complexes (**2a** and **2b**) were isolated as yellow solids, in good yields. In the proton NMR spectra of both complexes **2a** and **2b**, the signals due to the acidic C-2 protons observed at 10.44 and 10.38 ppm in the spectrum of the pre-carbenes (**1a** and **1b**), have completely disappeared, indicating the palladation of the NHC-precursors and therefore, successful formation of the complexes. Moreover, signals due to neighboring protons were observed to shift as a result of the complexes' formation. The proposed structures were further confirmed from the FT-IR spectral data and the elemental analyses results and were supported by the relevant literature [13, 23, 24, 26].

### *Evaluation of the catalytic activities of the Pd-NHC-Py complexes (2a and 2b) in the synthesis of cinnamic acids and derivatives. Optimization of reaction conditions*

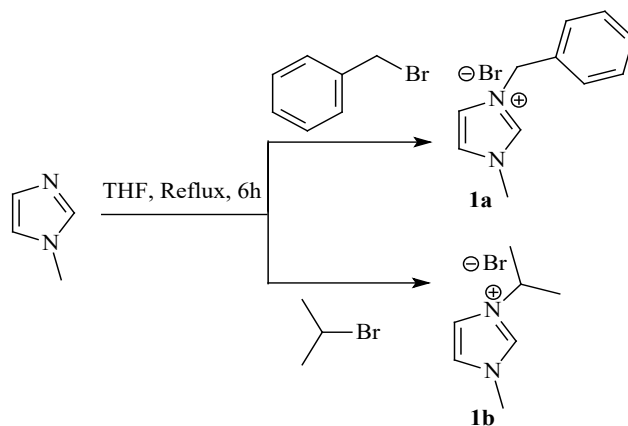
The cross-coupling reaction of aryl halides with olefins catalyzed using palladium (0) or palladium (II) compounds, known as the Mizoroki-Heck reaction, is a well-established and widely used protocol for the regioselective synthesis of internal alkenes under mild reaction conditions [6, 8, 9, 13]. The new Pd-NHC-Py complexes were used to

develop a mild and friendly method for Mizoroki-Heck coupling reactions of alkenes and aryl halides. Several aryl halides including iodides (**3a - c**) and bromides (**3d - f**) were coupled with acrylates, acrylic acids, and acrylamides.

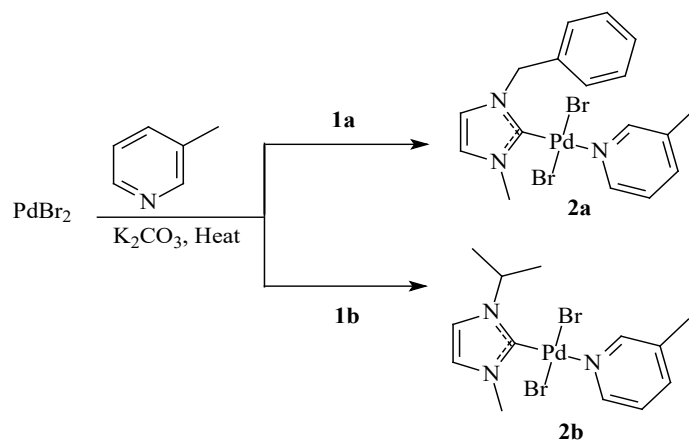
In order to find suitable experimental conditions, bromobenzene (**3d**) and methyl acrylate were selected as model substrates (Table 1). The catalytic activities of the Pd-NHC-Py complexes (**2a** and **2b**) were studied alongside commercially available palladium (II) salts. Initially, the reaction was carried out for 6 h using DMF as a solvent and KOH as a base. The conversion of the bromobenzene (**3d**) to the corresponding methyl cinnamate was poor (**5a**; 38%) (Table 1, entry 1). However, upon changing the solvent system to DMF/H<sub>2</sub>O (3:1 v/v) the yield of the product was improved to 78 % (Table 1, entry 2) with subsequent hydrolysis of the ester to the corresponding salt of the carboxylic acid. Moreover, the cinnamic acid (**5h**) was obtained in 95% yield upon changing the solvent DMF/H<sub>2</sub>O (1:1 v/v) (Table 1, entry 3). Interestingly, the yield remained excellent (96%) when the reaction was carried in neat water (Table 1, entry 4) thus, water was chosen as the optimum solvent. We went further and studied the effect of temperature on the reaction. Amazingly, the high yield was maintained when the temperature was reduced to 100 °C (Table 1, entry 5). As expected, the yield of the cinnamic acid (**5h**) isolated was found to decrease with a decrease in the reaction temperature up to 22 % at room temperature (Table 1, entries 6 - 8) therefore, 100°C was adopted as optimum. The effect of time on the reaction was then studied and the yield of the product was found to decrease with a decrease in reaction time (Table 1, entries 9, 10). We further studied the effect of a base on the reaction. As expected, no product was obtained in the absence of base (Table 1, entry 13) [7, 21] however, a similar yield was obtained with K<sub>2</sub>CO<sub>3</sub> as a base (Table 1, entry 11).

### *Mizoroki-Heck coupling reactions of alkenes with aryl halides using Pd-NHC-Py (2a) as catalyst. Synthesis of cinnamic acids*

Complex (**2a**) was further tried in a substrate scope study using the optimized reaction conditions [**2a** (1.0 mol%), KOH (2.0 mmol), water (4.0 mL), 100°C]. Aryl halides (nonactivated, deactivated, and activated, **3a - 3j**) were reacted with methyl acrylate (**4a**), acrylic acid (**4b**) methyl methacrylate (**4c**), and acrylamide (**4d**) to afford smoothly the corresponding cinnamic acid derivatives (**5a - 5g**) in moderate to excellent isolated yields.

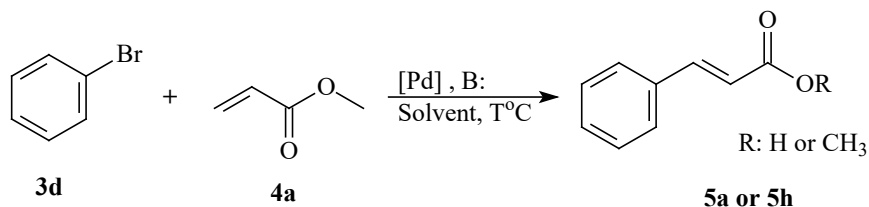


**Scheme 1.** Synthesis of 1,3-dialkylatedimidazolium bromides (NHC ligand precursors, **1a** and **1b**).



**Scheme 2.** Synthesis of NHC-pyridine palladium(II) bromides (**2a** and **2b**).

**Table 1.** Optimization of reaction conditions for the Mizoroki-Heck reaction of aryl halides with alkenes.



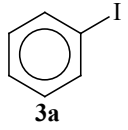
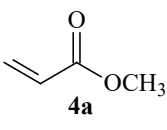
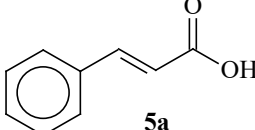
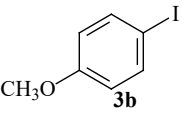
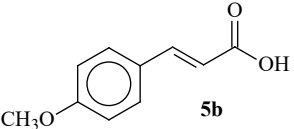
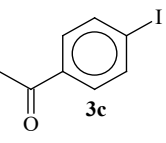
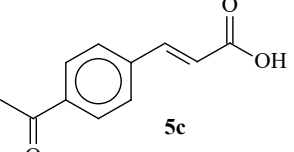
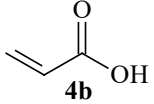
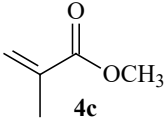
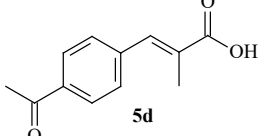
S/N	Catalyst	Solvent (4 mL)	Base	Temp. (°C)	Time (h)	Yield (%) <sup>b</sup>
1	2a	DMF	KOH	120	6	38
2	2a	DMF/Water (3:1)	KOH	120	6	78
3	2a	DMF/Water (1:1)	KOH	120	6	95
4	2a	Water	KOH	120	6	96
5	2a	Water	KOH	100	6	95
6	2a	Water	KOH	80	6	62
7	2a	Water	KOH	60	6	59



8	2a	Water	KOH	Rt	6	22
9	2a	Water	KOH	100	4	80
10	2a	Water	KOH	100	2	69
11	2a	Water	K <sub>2</sub> CO <sub>3</sub>	100	6	90
12	2a	Water	Et <sub>3</sub> N	100	6	22
13	2a	Water	-	100	6	00
14	-	Water	KOH	100	6	00
15	2b	Water	KOH	100	6	90
16	PdBr <sub>2</sub>	Water	KOH	100	6	60
17	PdCl <sub>2</sub> (PPh <sub>3</sub> ) <sub>2</sub>	Water	KOH	100	6	69
18	Pd(OAc) <sub>2</sub>	Water	KOH	100	6	59

<sup>a</sup> Reaction conditions: aryl halide (1.0 mmol), alkene (1.5 mmol), base (2.0 mmol), solvent (4.0 mL), catalyst loading (0.005 mmol). <sup>b</sup> Isolated yield.

**Table 2.** Mizoroki-Heck coupling reactions of alkenes with aryl halides using complex (2a) in water.

Entry	Aryl halide	Alkene	Coupling Product	Time (h)	Yield (%) <sup>b</sup>
1				1.5	96
2		4a		1.5	97
3		4a		1.5	96
4	3a		5a	1.5	94
4	3c			1.5	84

7	<b>3a</b>		<b>5a</b>	1.5	96
8		<b>4a</b>	<b>5a</b>	3	92
9		<b>4a</b>		3	94
10		<b>4a</b>		3	95
11	<b>3d</b>	<b>4c</b>		3	90
12	<b>3f</b>	<b>4d</b>	<b>5f</b>	6	92
13		<b>4a</b>	-	12	00
14	<b>3g</b>	<b>4b</b>	-	12	00
15	<b>3g</b>	<b>4d</b>	-	12	00

<sup>a</sup> Reaction conditions: *Pd-NHC-Py* (**2a**) (0.0100 mmol), aryl halide (1.00 mmol), alkene (1.50 mmol), KOH (2.00 mmol), H<sub>2</sub>O (4 mL), 100 °C. <sup>b</sup> Isolated yield.

Various functional groups on the aryl halides were well tolerated during the reaction, however, both the ester and the amide functional groups on the alkene were hydrolyzed during the reaction to the corresponding potassium salts of the carboxylic acids. The corresponding cinnamic acids were obtained upon acidification with 1 M HCl. Aryl iodides (**3a** - **3c**) were found to be most reactive and were converted quantitatively to the corresponding cinnamic acids (Table 2, entries 1-7) within an hour and a half. To our satisfaction, aryl bromides (**3d** - **3f**) cooperated well in the reaction though they required longer time relative to their iodo-counterparts (Table 2, entries 8 - 12). Aryl chloride (**3g**) (Table 2, entries 13-15) on the other hand, was found to be unreactive even for a longer reaction time of 12 h. The results were in agreement with the literature [27].

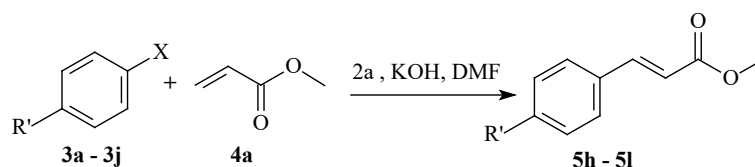
*Mizoroki-Heck coupling reactions of alkenes with aryl halides using Pd-NHC-Py (2a) as catalyst. Synthesis of cinnamates*

In addition to their use in the production of drugs, cinnamates are common raw materials for the cosmetic and perfumery industries [28, 29] A direct route to this important class of compounds is the palladium-catalyzed Mizoroki-Heck coupling reaction. Owing to the outstanding catalytic activity and selectivity displayed by the Pd-NHC-Py complexes in the synthesis of cinnamic acid derivatives, we envisaged that the new system can be adopted in the synthesis of cinnamates. However, as observed during the optimization reactions (Table 1), hydrolysis of the ester can easily be avoided by adopting anhydrous solvents such as anhydrous dimethylformamide. In fact, complex **2a** efficiently catalyzed the reaction of aryl iodides (**3a** - **3c**, **3h**,

and **3i**) and aryl bromides (**3d**, **3e**, and **3j**) with methyl acrylate (**4a**) in dried DMF, resulting in the corresponding cinnamate esters (**5h** – **5l**). We are delighted to report that all the activated and deactivated aryl iodides (Table 3, entries 1 - 5) and bromides (Table 3, entries 6 - 8) coupled with the methyl acrylate to afford the corresponding methyl

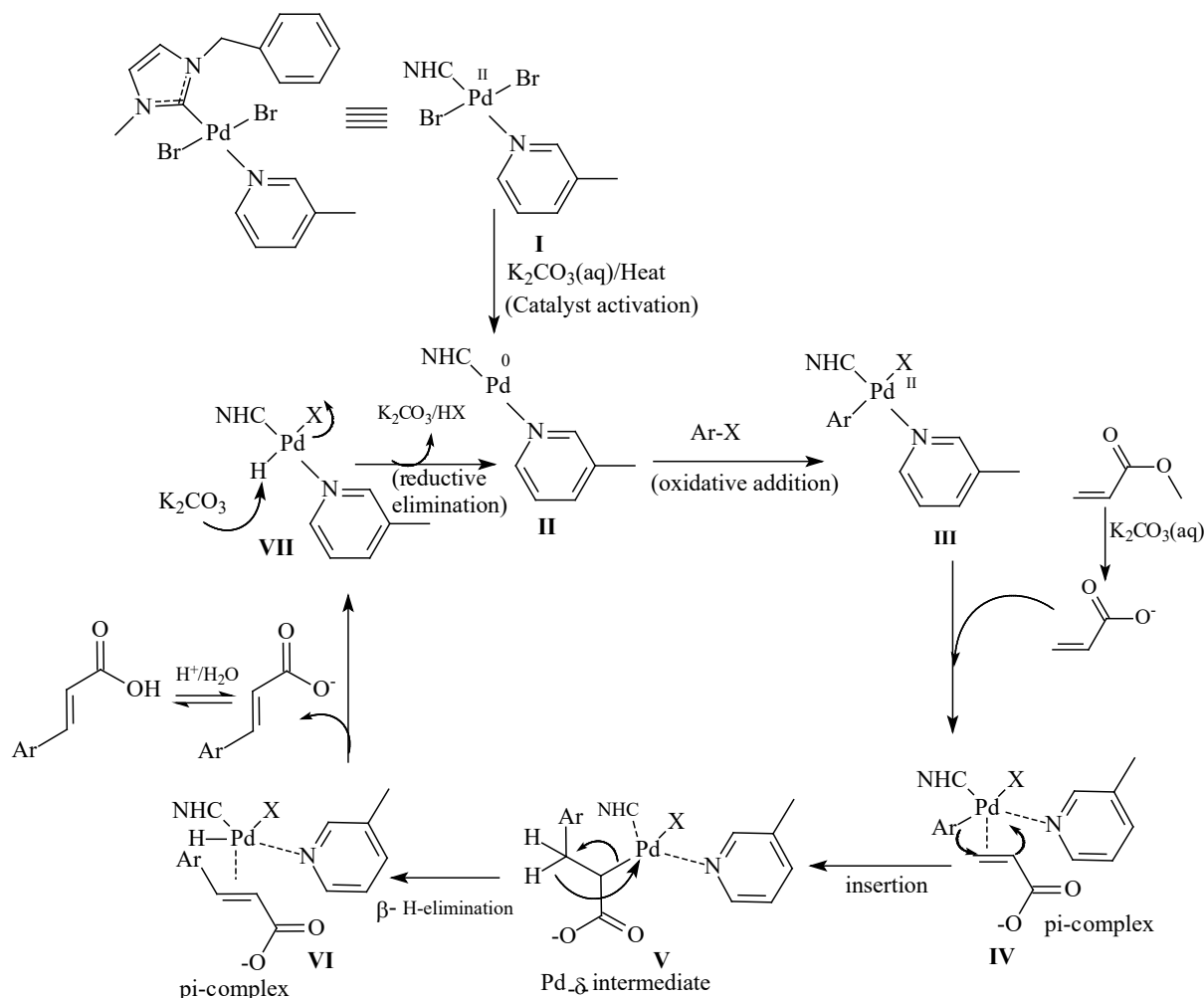
cinnamate in good to excellent yields. It is worth mentioning that the aryl bromides required higher temperatures and longer reaction times to afford a reasonable yield of the ester. This is not surprising due to the higher reactivity of the aryl iodides compared to the bromides.

**Table 3.** Mizoroki-Heck coupling reactions of methyl acrylate with aryl halides using **2a** as catalyst under anhydrous conditions.



Entry	Aryl halide	Alkene	Cinnamate obtained	Yield (%) <sup>b</sup>
	<b>3a</b>	<b>4a</b>	<b>5h</b>	89
2	<b>3b</b>	<b>4a</b>	<b>5i</b>	76
3	<b>3h</b>	<b>4a</b>	<b>5j</b>	70
4	<b>3c</b>	<b>4a</b>	<b>5k</b>	95
5	<b>3i</b>	<b>4a</b>	<b>5l</b>	92
6 <sup>c</sup>	<b>3d</b>	<b>4a</b>	<b>h</b>	74
7 <sup>c</sup>	<b>3e</b>	<b>4a</b>	<b>5m</b>	81
8 <sup>c</sup>	<b>3j</b>	<b>4a</b>	<b>5i</b>	66

<sup>a</sup> Reaction conditions: (**2a**) (0.0100 mmol), aryl halide (1.00 mmol), methylacrylate (1.50 mmol), KOH (2.00 mmol), DMF (4 mL), 12h, 100°C. <sup>b</sup> Isolated yield. <sup>c</sup> 110°C



**Scheme 3.** Plausible mechanism for the Pd-NHC-Py catalyzed Mizoroki-Heck cross-coupling reaction.

The mechanism of the Mizoroki-Heck cross-coupling is proposed based on established methods. The pre-catalyst Pd(II)-(S<sub>1</sub>)(Py)Br<sub>2</sub> (**I**) is activated through base-promoted reductive elimination of the bromo ligands to generate active Pd(0)-(S<sub>1</sub>)(Py) catalyst (**II**). This step is followed by oxidative addition of the aryl halide to the activated palladium (0) species to form a palladium (II) intermediate ArPdS<sub>1</sub>PyX (**III**). The alkene then coordinates to the intermediate (**III**) to form a π complex (**IV**). At this stage, there is insertion of the alkene into the Ar-Pd bond to yield a palladium-sigma intermediate (**V**), then beta hydride elimination to produce another π complex (**VI**). Release of the cross-coupled product followed by reductive elimination regenerates the active palladium catalyst (**II**).

The higher catalytic activity realized using the Pd-NHC-Py system compared to the palladium/phosphine systems could be attributed to the following: contrary to the phosphine ligands, NHCs are known to be stronger sigma donors and form more stable transition metal complexes than the phosphine-based analogues [22, 30]. Furthermore,

both the pre-catalyst Pd(II)-(S<sub>1</sub>)(Py)Br<sub>2</sub> (**I**) and the proposed active species Pd(0)-(S<sub>1</sub>)(Py) (**II**) are more stable compared with the phosphines and other commercially available palladium precursors and catalysts (Table 1). In the proposed new systems, both the oxidative addition and substitution steps are likely to be enhanced by the more electron-rich species Pd(0)-(S<sub>1</sub>)(Py) (**II**). Moreover, the inductive and mesomeric effects of the benzyl substituent resulted in a more electron-rich palladium centre leading to a catalyst of higher activity.

## CONCLUSION

Imidazolium salts and their corresponding palladium-pyridine complexes (Pd-NHC-Py) were successfully synthesized and characterized. The synthesis of cinnamic acids and cinnamates was achieved under mild reaction conditions using the synthesized pre-catalysts. Various cinnamic acids derivatives and cinnamates were obtained in good to excellent yields. A reaction mechanism was proposed based on the formation of an active palladium (0) species.

**Acknowledgement:** Authors wish to thank the Department of Pure and Industrial Chemistry, Bayero University, Kano, Nigeria for providing some of the materials used in this study.

#### REFERENCES

1. I. M. C. M., Rietjens, S. M. Cohen, G. Eisenbrand, S. Fukushima, N. J. Gooderham, F. P. Guengerich, S. S. Hecht, T. J. Rosol, J. M. Davidsen, L. Harman, I. J. Murray, S. V. Taylor, *Food and Chemical Toxicology*, **135**, 110949 (2020), (<https://doi.org/10.1016/j.fct.2019.110949>).
2. P. De, M. Baltas, F. Bedos-Belval, *Curr. Med. Chem.*, **18**, 1672 (2011), (<https://doi.org/10.2174/092986711795471347>).
3. T. W. Lyons, M. S. Sanford, *Chem. Rev.*, **110**, 1147 (2010), (<https://doi.org/10.1021/cr900184e>).
4. G. K. Rao, A. Kumar, S. Kumar, U. B. Dupare, A. K. Singh, *Organometallics*, **32**, 2452 (2013), (<https://doi.org/10.1021/om4001956>).
5. T. Szilvasi, T. Veszpremi, *ACS Catal.*, **3**, 1984 (2013), (<https://doi.org/10.1021/cs400429j>).
6. S. M. Shakil-Husseini, M. B. Ibrahim, A. Fazal, R. Suleiman, M. Fettouhi, B. El Ali, *Polyhedron*, **70**, 39 (2014), (<http://dx.doi.org/10.1016/j.poly.2013.12.023>).
7. M. Nikoorazm, M. Khanmoradi, Z. Abdi, *J. Iran. Chem. Soc.*, **17**, 2577 (2020), (<https://doi.org/10.1007/s13738-020-01952-9>).
8. M. B. Ibrahim, B. El Ali, M. Fettouhi, L. Ouahab, *Appl. Organomet. Chem.*, **29**, 400 (2015), (<https://doi.org/10.1002/aoc.3305>).
9. M. B. Ibrahim, S. M. Shakil Hussain, A. Fazal, M. Fettouhi, B. El Ali, *J. Coord. Chem.*, **68**, 432 (2015), (<http://dx.doi.org/10.1080/00958972.2014.995100>).
10. G. Hamasaka, S. Ichii, Y. Uozumi, *Adv. Synth. Catal.*, **360**, 1833 (2018), (<http://doi.org/10.1002/adsc.201800099>).
11. L. Jin, L. Qian, N. Sun, B. Hu, Z. Shen, X. Hu, *Chem. Commun.*, **54**, 5752 (2018), (<http://doi.org/10.1039/C8CC02571A>).
12. W. Li, C. Y. Li, H. Y. Xiong, Y. Liu, W. Y. Huang, G. J. Ji, Z. Jiang, H. T. Tang, Y. M. Pan, Y. J. Ding, *Angew. Chem. Int. Ed.*, **58**, 2448 (2019), (<http://doi.org/10.1002/anie.201814493>).
13. V. H. Nguyen, M. B. Ibrahim, W. W. Mansour, B. M. El Ali, H. V. Huynh, *Organometallics*, **36**, 2345 (2017), (<https://doi.org/10.1021/acs.organomet.7b00329>).
14. E. Levin, E. Ivry, C. E. Diesendruck, N. G. Lemcoff, *Chem. Rev.*, **115**, 4607 (2015), (<https://doi.org/10.1021/cr400640e>).
15. K. Tanaka, *Angew. Chem. Int. Ed.*, **42**, 4851 (2003), (<https://doi.org/10.1002/anie.200300585>).
16. P. G. Jessop, W. Leitner, *Chemical synthesis using supercritical fluids*, Wiley-VCH, 2007, p. 1.
17. J. A. Gladysz, D. P. Curran, *Tetrahedron*, **58**, 3823 (2002), ([https://doi.org/10.1016/s0040-4020\(02\)00222-3](https://doi.org/10.1016/s0040-4020(02)00222-3)).
18. C. J. Li, *Chem. Rev.*, **105**, 3095 (2005), (<https://doi.org/10.1021/cr030009u>).
19. R. Breslow, *Acc. Chem. Res.*, **24**, 159 (1991), (<http://doi.org/10.1021/ar00006a001>).
20. R. Breslow, *Acc. Chem. Res.*, **37**, 471 (2004), (<http://doi.org/10.1021/ar040001m>).
21. M. B. Ibrahim, S. Rami, M. Fettouhi, B. El Ali, *Transit. Met. Chem.*, **42**, 1 (2017), (<https://doi.org/10.1007/s11243-016-0072-1>).
22. M. B. Ibrahim, I. Malik, W. Mansour, M. Sharif, M. Fettouhi, B. El Ali, *Appl. Organometal. Chem.*, **32**, 4 (2018), (<https://doi.org/10.1002/aoc.4280>).
23. M. B. Ibrahim, I. Malik, W. Mansour, M. Sharif, M. Fettouhi, B. El Ali, *J. Organometal. Chem.*, **859**, 44 (2018), (<https://doi.org/10.1016/j.jorganchem.2018.01.028>).
24. D. J. D. Wilson, S. A. Couchman, J. L. Dutton, *Inorg. Chem.*, **51**, 7657 (2012), (<https://doi.org/10.1021/ic300686n>).
25. A. Valls, J. J. Andreu, E. Falomir, S. V. Luis, E. Atrian-Blasco, S. G. Mitchell, B. Altava, *Pharmaceuticals*, **13**, 482 (2020), (<https://doi.org/10.3390/ph13120482>).
26. I. Slimani, L. Mansour, I. Ozdemir, N. Gurbuz, N. Hamdi, *Inorg. Chim. Acta*, **515**, 120043 (2021), (<https://doi.org/10.1016/j.ica.2020.120043>).
27. P. G. Bangar, P. D. Nahide, H. K. Meroliya, S. A. Waghmode, S. Iyer, *Synthetic Communications*, **51**, 308 (2021), (<https://doi.org/10.1080/00397911.2020.182669>).
28. A. Gunia-Krzyzak, K. Slocynska, J. Popiol, P. Koczurkiewicz, H. Marona, E. Pekala, *International Journal of Cosmetic Science*, **40**, 356 (2018), (<https://doi.org/10.1111/ics.12471>).
29. S. P. Bhatia, G. A. Wellington, J. Cocchiara, J. Lalko, S. S. Letizia, A. M. Api, *Food and Chemical Toxicology*, **566**, 308 (2007), (<https://doi.org/10.1016/j.fct.2007.09.030>).
30. J. Jover, N. Fey, M. Purdie, G. C. Lloyd-Jones, J. N. A. Harvey, *J. Mol. Catal. A*, **39**, 324 (2010), (<https://doi.org/10.1016/j.molcata.2010.02.021>).

## BULGARIAN CHEMICAL COMMUNICATIONS

### Instructions about Preparation of Manuscripts

**General remarks:** Manuscripts are submitted in English by e-mail or by mail (in duplicate). The text must be typed double-spaced, on A4 format paper using Times New Roman font size 12, normal character spacing. The manuscript should not exceed 15 pages (about 3500 words), including photographs, tables, drawings, formulae, etc. Authors are requested to use margins of 3 cm on all sides. For mail submission hard copies, made by a clearly legible duplication process, are requested. Manuscripts should be subdivided into labelled sections, e.g. **Introduction, Experimental, Results and Discussion, etc.**

**The title page** comprises headline, author's names and affiliations, abstract and key words.

Attention is drawn to the following:

a) **The title** of the manuscript should reflect concisely the purpose and findings of the work. Abbreviations, symbols, chemical formulas, references and footnotes should be avoided. If indispensable, abbreviations and formulas should be given in parentheses immediately after the respective full form.

b) **The author's** first and middle name initials, and family name in full should be given, followed by the address (or addresses) of the contributing laboratory (laboratories). **The affiliation** of the author(s) should be listed in detail (no abbreviations!). The author to whom correspondence and/or inquiries should be sent should be indicated by asterisk (\*).

**The abstract** should be self-explanatory and intelligible without any references to the text and containing not more than 250 words. It should be followed by key words (not more than six).

**References** should be numbered sequentially in the order, in which they are cited in the text. The numbers in the text should be enclosed in brackets [2], [5, 6], [9–12], etc., set on the text line. References, typed with double spacing, are to be listed in numerical order on a separate sheet. All references are to be given in Latin letters. The names of the authors are given without inversion. Titles of journals must be abbreviated according to Chemical Abstracts and given in italics, the volume is typed in bold, the initial page is given and the year in parentheses. Attention is drawn to the following conventions:

a) The names of all authors of a certain publications should be given. The use of “*et al.*” in

the list of references is not acceptable.

b) Only the initials of the first and middle names should be given.

In the manuscripts, the reference to author(s) of cited works should be made without giving initials, e.g. “Bush and Smith [7] pioneered...”. If the reference carries the names of three or more authors it should be quoted as “Bush *et al.* [7]”, if Bush is the first author, or as “Bush and co-workers [7]”, if Bush is the senior author.

**Footnotes** should be reduced to a minimum. Each footnote should be typed double-spaced at the bottom of the page, on which its subject is first mentioned.

**Tables** are numbered with Arabic numerals on the left-hand top. Each table should be referred to in the text. Column headings should be as short as possible but they must define units unambiguously. The units are to be separated from the preceding symbols by a comma or brackets.

Note: The following format should be used when figures, equations, *etc.* are referred to the text (followed by the respective numbers): Fig., Eqns., Table, Scheme.

**Schemes and figures.** Each manuscript (hard copy) should contain or be accompanied by the respective illustrative material as well as by the respective figure captions in a separate file (sheet). As far as presentation of units is concerned, SI units are to be used. However, some non-SI units are also acceptable, such as °C, ml, l, etc.

The author(s) name(s), the title of the manuscript, the number of drawings, photographs, diagrams, etc., should be written in black pencil on the back of the illustrative material (hard copies) in accordance with the list enclosed. Avoid using more than 6 (12 for reviews, respectively) figures in the manuscript. Since most of the illustrative materials are to be presented as 8-cm wide pictures, attention should be paid that all axis titles, numerals, legend(s) and texts are legible.

The authors are asked to submit **the final text** (after the manuscript has been accepted for publication) in electronic form either by e-mail or mail on a 3.5” diskette (CD) using a PC Word-processor. The main text, list of references, tables and figure captions should be saved in separate files (as \*.rtf or \*.doc) with clearly identifiable file names. It is essential that the name and version of

the word-processing program and the format of the text files is clearly indicated. It is recommended that the pictures are presented in \*.tif, \*.jpg, \*.cdr or \*.bmp format, the equations are written using "Equation Editor" and chemical reaction schemes are written using ISIS Draw or ChemDraw programme.

The authors are required to submit the final text with a list of three individuals and their e-mail addresses that can be considered by the Editors as potential reviewers. Please, note that the reviewers should be outside the authors' own institution or organization. The Editorial Board of the journal is not obliged to accept these proposals.

## EXAMPLES FOR PRESENTATION OF REFERENCES

### REFERENCES

1. D. S. Newsome, *Catal. Rev.–Sci. Eng.*, **21**, 275 (1980).
2. C.-H. Lin, C.-Y. Hsu, *J. Chem. Soc. Chem. Commun.*, 1479 (1992).
3. R. G. Parr, W. Yang, *Density Functional Theory of Atoms and Molecules*, Oxford Univ. Press, New York, 1989.
4. V. Ponec, G. C. Bond, *Catalysis by Metals and Alloys* (Stud. Surf. Sci. Catal., vol. 95), Elsevier, Amsterdam, 1995.
5. G. Kadinov, S. Todorova, A. Palazov, in: *New Frontiers in Catalysis* (Proc. 10th Int. Congr. Catal., Budapest, 1992), L. Guzzi, F. Solymosi, P. Tetenyi (eds.), Akademiai Kiado, Budapest, 1993, Part C, p. 2817.
6. G. L. C. Maire, F. Garin, in: *Catalysis. Science and Technology*, J. R. Anderson, M. Boudart (eds), vol. 6, Springer-Verlag, Berlin, 1984, p. 161.
7. D. Pocknell, *GB Patent 2 207 355* (1949).
8. G. Angelov, PhD Thesis, UCTM, Sofia, 2001.
9. JCPDS International Center for Diffraction Data, Power Diffraction File, Swarthmore, PA, 1991.
10. *CA* **127**, 184 762q (1998).
11. P. Hou, H. Wise, *J. Catal.*, in press.
12. M. Sinev, private communication.
13. <http://www.chemweb.com/alchem/articles/1051611477211.html>.

CONTENTS

<i>D. M. Djordjevic, R. P. Krstic, M. G. Kodric, S. P. Djordjevic</i> , Modeling of polyester fabric dyeing after proteolytic enzyme pre-treatment.....	115
<i>S. Abarova, B. Antonova, K. Stoichkova, N. Nakova, P. Abarov, A. Zasheva, R. Koynova, B. Tenchov</i> , Spectroscopic and thermodynamic characterization of the chemotherapy drug Epirubicin interaction with human serum albumin.....	121
<i>N. Umairambika, N. Arunodhaya, S. Renganathan</i> , Extraction of underexploited <i>Vernonia cinerea</i> oil with comparative pretreatment techniques for conversion into biodiesel.....	126
<i>P. B. Kumar, S. Srinivas</i> , MHD Eyring-Powell nanofluid flow in a channel with oscillatory pressure gradient: A note.....	134
<i>M. J. Dencheva-Zarkova, D. Yankov, J. L. Genova, I. Tsibranska</i> , Flux and separation efficiency in nanofiltration with mixed solvents.....	141
<i>I. V. Vasileva, I. N. Kolev</i> , A sulfur-based qualitative test for determining the presence of the secondary alcohol functional group of (-)-quinine and (+)-quinidine.....	147
<i>P.G. Velichkova, M. R. Popova, A. T. Angelov</i> , Optimization of the operating parameters of microbial electrolysis cell assisted anaerobic digester for generating bioenergy from an ethanol.....	152
<i>G. Sangavi, J. Jayapriya, G. Nandhini Devi</i> , A kinetic study on the effect of short-term frying cycles on the properties of cold pressed peanut oil.....	158
<i>A. M. Aliyev, A. R. Safarov, G. A. Ali-zadeh, F. V. Aliyev</i> , Study of the kinetics and mechanism of the oxidative conversion of ethyl alcohol to acetic acid over the modified natural zeolite catalyst clinoptilolite.....	164
<i>M. B. Ibrahim, S. A. Rufa'i, H. U. Yaqub, U. B. Suleiman</i> , Efficient palladium <i>n</i> -heterocyclic carbene catalytic system for the synthesis of cinnamic acid and derivatives in water stillage .....	172
<i>INSTRUCTIONS TO AUTHORS</i> .....	182